

**MODELING OF MICRO-DIAPHRAGM FOR OPTICAL
PRESSURE SENSOR FOR HUMAN ARTERY PULSE
WAVE DETECTION**

KHAIRUNNISA HASIKIN

**THESIS SUBMITTED IN FULFILMENT
OF REQUIREMENTS
FOR THE DEGREE OF MASTER OF ENGINEERING
SCIENCE**

Perpustakaan Universiti Malaya




A513413525

**FACULTY OF ENGINEERING
UNIVERSITY OF MALAYA
KUALA LUMPUR**

SEPTEMBER 2010

UNIVERSITY OF MALAYA

ORIGINAL LITERARY WORK DECLARATION

Name of Candidate : KHAIRUNNISA BINTI HASIKIN 

Registration/Matric No: KGA070062

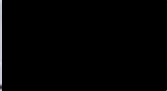
Name of Degree: MASTER OF ENGINEERING SCIENCE

Title of Thesis("this Work"): MODELING OF MICRO-DIAPHRAGM FOR OPTICAL PRESSURE SENSOR FOR HUMAN ARTERY PULSE WAVE DETECTION

Field of Study: BIOMEMS

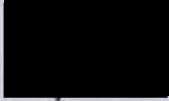
I do solemnly and sincerely declare that:

- (1) I am the sole author/writer of this Work;
- (2) This Work is original;
- (3) Any use of any work in which copyright exists was done by way of fair dealing and for permitted purposes and any excerpt or extract from, or reference to or reproduction of any copyright work has been disclosed expressly and sufficiently and the title of the Work and its authorship have been acknowledged in this Work;
- (4) I do not have any actual knowledge nor do I ought reasonably to know that the making of this work constitutes an infringement of any copyright work;
- (5) I hereby assign all and every rights in the copyright to this Work to the University of Malaya ("UM"), who henceforth shall be owner of the copyright in this Work and that any reproduction or use in any form or by any means' whatsoever is prohibited without the written consent of UM having been first had and obtained;
- (6) I am fully aware that if in the course of making this Work I have infringed any copyright whether intentionally or otherwise, I may be subject to legal action or any other action as may be determined by UM.

Candidate's Signature: 

Date: 3/9/2010

Subscribed and solemnly declared before,

Witness's Signature 

Date: 3/9/2010

Name:

Designation:

Dr. Ting Hua Mong
Senior Lecturer
Department of Biomedical Engineering
Faculty of Engineering, University of Malaya
50603 Kuala Lumpur
Malaysia

ABSTRACT

This thesis presents the development of a micro-diaphragm for an optical pulse pressure sensor using Micro-electro-mechanical Systems (MEMS) technology. Modelling of the micro-diaphragm was conducted and the comparison of its performance was simulated for silicon nitride and polyimide materials. In addition, diaphragm's radius and thickness were varied to further analyze the performance of the micro-diaphragm. There are three design parameters that affecting the micro-diaphragm performance namely diaphragm's radius, thickness and material. Thus, an optimization analysis using Taguchi method was done to attain significant design parameters that give the best micro-diaphragm performance. Findings indicated that the best performance of the micro-diaphragm was obtained when the micro-diaphragm achieved high deflection and sensitivity as well as low resonance frequency. Simulation results have concluded that these performances are achieved when the diaphragm's radius and thickness are large and small respectively. Furthermore, the Taguchi method verified that the optimized design parameters radius of $90\mu\text{m}$, thickness of $4\mu\text{m}$ and polyimide material have successfully achieved the best micro-diaphragm performance. In addition, the selected design parameters have been proven to provide an adequate sensitivity to detect the pulse pressure on human's radial artery.

ACKNOWLEDGEMENTS

First and foremost, I would like to say Alhamdulillah because by His blessing, I finally completed this thesis. I would like to express my sincere gratitude and special wish to acknowledge the following:

- To both distinguished supervisors, Assoc. Prof. Dr. Fatimah Ibrahim and Assoc. Prof. Dr. Norhayati Soin for their supervision, advice and full support.
- To my Head of Department, Assoc. Prof. Dr. Noor Azuan Abu Osman for the trust he gave me in making this research possible.
- To all my friends in Clinical Engineering and BioMEMS Laboratories, Nurul Aini Yusoff, Naemah Suhaimi, Noor Aimie Salleh, Salmah Karman, Siti Hajar Othman, Mohd. Naim Mohd Ibrahim, Helmy Rizal Salahudin, Tan Yin Qing, and Leow Ruen Shan for their encouragements and supports.
- To the Department of Biomedical Engineering's staffs, Ng. Siew Cheok, Rohana Ismail, Maznah Mohammad Zin, Azuan Othman, Mohd Asni Mohamed and Zulkafli Muhamad for their help during my studies.
- To all the important people in my life, my mother Fabilah Ismail, my father Hasikin Jasman, my brother Fazrul Ikram, and my sister Arina for their never ending support and understanding.
- And lastly to many of my friends inside and outside the University of Malaya, namely Junaidah Md Jan, Syamsul Kamarudin, and Aliaa Diyana Aziz for their moral support and help they provided me.

TABLE OF CONTENTS

ABSTRACT	I
ACKNOWLEDGEMENTS	II
TABLE OF CONTENTS	i
LIST OF FIGURES	iv
LIST OF TABLES	viii
LIST OF ABBREVIATIONS	x
1.0 INTRODUCTION	
1.1 Overview	1
1.2 Objective of Thesis	3
1.3 Scope of Work	3
1.4 Organization of Thesis	4
2.0 LITERATURE REVIEW	
2.1 Introduction	5
2.2 Arterial Stiffness	5
2.2.1 Mechanisms of Arterial Stiffness	5
2.2.2 Diagnosis Techniques for Arterial Stiffness	8
2.3 BioMEMS Pressure Sensing Principles	16
2.3.1 Piezoresistive	17
2.3.2 Capacitive	18
	i

2.3.3	Optical	21
2.4	The Performance of Micro-Diaphragm	23
2.5	Micro-Diaphragm Material	25
2.6	Design Optimization Techniques	32
2.7	Summary	36
3.0	DESIGN METHODOLOGY	
3.1	Introduction	38
3.2	Micro-Diaphragm Design Processes	39
3.2.1	Operation of the micro-diaphragm	39
3.2.2	Micro-diaphragm Design Specifications	41
3.2.3	Modelling of the micro-diaphragm	42
3.3	Micro-Diaphragm Performance Analysis	46
3.3.1	Simulation Conditions	47
3.3.2	Static Response of the Micro-Diaphragm	50
3.3.3	Frequency Response of the Micro-Diaphragm	55
3.3.4	Transient Response of the Micro-Diaphragm	59
3.4	Optimization Technique in Designing the Micro-Diaphragm	61
3.4.1	S/N Ratio	63
3.4.2	Pareto Analysis of Variance (ANOVA)	67

4.0 RESULTS AND ANALYSIS

4.1	Introduction	70
4.2	Micro-Diaphragm Performance Response	70
4.2.1	Static Response Analysis	71
4.2.2	Frequency Response Analysis	86
4.2.3	Transient Response Analysis	94
4.3	Optimization Analysis by using Taguchi Method	97
4.3.1	Analysis of Signal-to-noise (S/N) ratio	97
4.3.2	Analysis of Pareto ANOVA	101
4.4	Summary	104

5.0 CONCLUSIONS AND FUTURE WORKS

5.1	Conclusions	108
5.2	Future Works	109
5.2.1	Improvement for micro-diaphragm structural design	109
5.2.2	Fabrication Process	110

REFERENCES	111
-------------------	------------

APPENDICES

Appendix A	List of Publications	121
Appendix B	Simulation Results	123
Appendix C	Calculation formula in Taguchi Method	128

LIST OF FIGURES

FIGURES	PAGE NUMBER
Figure 2.1 : Stiffening process of the artery	6
Figure 2.2 : Magnetic resonance imaging scanner	10
Figure 2.3 : Duplex ultrasound probe	11
Figure 2.4 : Radial pulse contour derived from the radial artery	13
Figure 2.5 : Principle of tonometer	14
Figure 2.6 : Unbonded strain gauge pressure sensor	15
Figure 2.7 : Silicon-based pressure sensor	16
Figure 2.8 : Applying a dc voltage to conductive objects	19
Figure 2.9 : Applying an alternating current to conductive objects	20
Figure 2.10 : Categories of micromechanical materials	25
Figure 2.11 : Material properties of MEMS	26
Figure 2.12 : The difference between structural robustness and reliability	34
Figure 3.1 : Flowchart of the design methodology	39
Figure 3.2 : Proposed design of the optical pulse pressure sensor	40
Figure 3.3 : 3D micro-diaphragm model	43
Figure 3.4 : Fabrication process for the diaphragm	44
Figure 3.5 : Example of mask for patterning process	46
Figure 3.6 : Micro-diaphragm with fixed boundary	48

Figure 3.7 :	3D micro-diaphragm model before and after meshed	49
Figure 3.8 :	Structure model for the circular diaphragm	50
Figure 3.9 :	Vibration modes	57
Figure 3.10 :	Nodal circles and nodal diameters	57
Figure 3.11 :	Three stages in Taguchi Method	62
Figure 3.12 :	Two major tools in robust design	62
Figure 3.13 :	Flowchart of Taguchi Method used in designing the micro-diaphragm	64
Figure 4.1 :	Diaphragm deflection from (a) top view (b) side view and(c) bottom view Deflection of rigidly clamped diaphragm	71
Figure 4.2 :	Relationship between diaphragm deflection and ratio of radial distance to radius	72
Figure 4.3 :	3D graph of diaphragm deflection of circular diaphragm	73
Figure 4.4 :	Diaphragm deflection and flexural rigidity versus diaphragm thickness for (a) polyimide diaphragm (b) silicon nitride diaphragm	74
Figure 4.5 :	Simulation result shows relationship between diaphragm deflection and applied pressure for (a) polyimide and (b) silicon nitride diaphragms	77
Figure 4.6 :	Relationship among sensitivity, diaphragm radius	78

and diaphragm thickness

- Figure 4.7 : Simulation result show the diaphragm pressure sensitivity in relation with diaphragm radius for (a) polyimide and (b) silicon nitride diaphragms 80
- Figure 4.8 : Sensitivity and flexural rigidity in relation with diaphragm thickness for (a) polyimide and (b) silicon nitride diaphragms 82
- Figure 4.9 : Tangential stress distribution of the diaphragm 83
- Figure 4.10 : Radial stress distribution of the diaphragm 84
- Figure 4.11 : Simulation results on diaphragm deflection and stress in relation with diaphragm radius 85
- Figure 4.12 : Relationship among diaphragm radius, diaphragm thickness and resonance frequency 87
- Figure 4.13 : Resonance Frequency in relation with diaphragm thickness 88
- Figure 4.14 : Diaphragm deflection and resonance frequency in relation with diaphragm thickness 89
- Figure 4.15 : Resonance Frequency and flexural rigidity in relation with diaphragm radius for (a) polyimide and (b) silicon nitride diaphragms 91
- Figure 4.16 : Diaphragm deflection versus frequency for polyimide diaphragm 93
- Figure 4.17 : Diaphragm deflection versus frequency for silicon 93

	PAGE NUMBER
nitride diaphragm	
Figure 4.18 : Deflection versus time for polyimide diaphragm	95
Figure 4.19 : Deflection vs time for silicon nitride diaphragm	95
Figure 4.20 : The mean signal-to-noise ratio graph for diaphragm deflection and diaphragm pressure sensitivity	99
Figure 4.21 : The mean signal-to-noise ratio graph for resonance frequency	99
Figure 4.22 : Pareto diagram for (a) diaphragm deflection (b) diaphragm pressure sensitivity and(c) resonance frequency	103

LIST OF TABLES

TABLES	PAGE NUMBER
Table 2.1 : Comparison of material properties for silicon based, polymer based and metal based diaphragm materials	27
Table 2.2: Comparison between reliability-based method and robust design-based method	35
Table 3.1: Diaphragm design specifications	42
Table 3.2: Fabrication process involved in the modeling of the micro-diaphragm	45
Table 3.3: Values of constant α_{mn}	57
Table 3.4: Values of $\lambda\alpha_{mn}$	58
Table 3.5: Design Parameters and Material Properties of Polyimide and Silicon Nitride Diaphragms	61
Table 3.6: Commonly used orthogonal array	63
Table 3.7: Control factors and levels in the diaphragm design	66
Table 3.8: Basic Taguchi L8 (2^3) orthogonal array	66
Table 3.9: Pareto ANOVA for two level factors	68
Table 4.1: Simulated parameters and calculated S/N ratios for diaphragm deflection, diaphragm pressure sensitivity and resonance frequency	97
Table 4.2: Response Table of Mean S/N ratio for the larger the	98

	better characteristic of diaphragm deflection, and diaphragm pressure sensitivity	
Table 4.3:	Response Table of Mean S/N ratio for smaller the better characteristic of resonance frequency	98
Table 4.4:	The calculated BC two-way table for diaphragm deflection	100
Table 4.5:	The calculated BC two-way table for diaphragm pressure sensitivity	100
Table 4.6:	The calculated BC two-way table for resonance frequency	101
Table 4.7:	Pareto ANOVA analyses for diaphragm deflection	102
Table 4.8:	Pareto ANOVA analyses for diaphragm pressure sensitivity	102
Table 4.9:	Pareto ANOVA analyses for resonance frequency	102
Table 4.10:	Comparison of designed diaphragm model for the optical pulse pressure sensor with the other available pulse pressure sensor	107

LIST OF ABBREVIATIONS

ABBREVIATIONS

MEMS	Micro-electro-mechanical systems
BioMEMS	Biological micro-electro-mechanical systems
IVUS	Intravascular ultrasound
MRI	Magnetic resonance imaging
CAD	Coronary artery disease
PWA	Pulse wave analysis
PVD	Peripheral vascular disease
DOE	Design of experiment
LED	Light emitting diode
PECVD	Plasma-enhanced chemical vapor deposition
TEOS	Tetraethoxysilane
FEA	Finite element analysis
3D	Three-dimensional
ANOVA	Analysis of variance
S/N	Signal-to-Noise
dB	Decibel

CHAPTER 1

INTRODUCTION

1.1 Overview

Arterial stiffness is a disease which affects arterial blood vessels. It results from a deposition of tough, rigid collagen inside the vessel wall and around atheroma (Pouladian *et al.*, 2003). It is also caused by the build-up of fatty deposits (plaques) inside the arteries wall. These plaques will reduce the blood flow through the artery (Latifoglu *et al.*, 2007).

The arterial stiffness can be considered the most important underlying cause of strokes, heart attack and various heart diseases. Many researchers have demonstrated that pulse pressure is the strongest predictor of coronary heart failures and arterial stiffness (Darne *et al.*, 1989, Franklin *et al.*, 1999, Benetos *et al.*, 1997 and Fang *et al.*, 1995).

A high pulse pressure is correlated with a decrease in aortic elasticity probably due to arterial stiffness. Cardiovascular mortality and its various clinical manifestations such as angina, myocardial infarction and stroke are increased in the presence of raised pulse pressure (Darne *et al.*, 1989).

Commercial miniature sensors available, regardless of their invasiveness can present only a percentage of arterial occlusions. There is no information on the degrees of sclerosis and stiffness of the arteries which can be directly gained from them (Pouladian *et al.*, 2003, Hill *et al.*, 2007).

In order to obtain parameters such as distension and stiffness of the arteries, the movement of the arteries walls during pulsation must be accurately detected. For this purpose, several techniques are used in the recent years. This includes Magnetic Resonance Imaging, Angiography, Intravascular Ultrasound and biomedical pressure sensor.

A study conducted on arterial pulse pressure waveform has shown its potential to indicate physiological changes due to arterial stiffness. Moreover, a recent advance in Micro-electro-mechanical Systems (MEMS) field has enabled the development of a miniature pulse pressure sensor. This miniature pulse pressure sensor is able to detect the pulse pressure on the human's radial artery. The detection of pulse pressure will determine the degree of sclerosis in the arteries wall.

Sensing principles such as capacitive (Chatzandroulis *et al.*, 1997), piezoresistive (Druzhinin *et al.*, 1999) and optical (Tohyama *et al.*, 1998, Katsumata *et al.*, 2000) MEMS have a good potential in biomedical application. The ability to guide signals to and from a measurement site has made the optical MEMS technology attractive in designing a pulse pressure sensor.

Thus, the optical pulse pressure sensor has been proposed to detect the pulse pressure on the human's radial artery. The detection of the pulse pressure will give valuable information on the degree of stiffness of the artery. The proposed optical pulse pressure sensor is therefore convenient to be used as it will be placed on the human's wrist.

This proposed optical pulse pressure sensor was designed using MEMS technology. In addition, the proposed sensor also consists of an optical fibre and micro-

diaphragm which acts as a pressure sensor. However, this study only focused on designing a micro-diaphragm for the optical pulse pressure sensor.

In this study, a micro-diaphragm based optical pulse pressure sensor was designed and its performance was analyzed to obtain the optimum performance for pulse pressure measurement in a range of 0 to 300 mmHg.

It is important to note that the micro-diaphragm performance is affected by three design parameters namely diaphragm radius, diaphragm thickness and diaphragm material. The three design parameters inevitably affected the performance of the micro-diaphragm. Thus optimization analysis of Taguchi Method is employed to attain the optimum design parameters which could give the best micro-diaphragm performance.

1.2 Objective of Thesis

The objective of this study was to design a micro-diaphragm for an optical pulse pressure sensor using the MEMS technology.

1.3 Scope of Work

The scope of work covered in the present study is as follows:

- i. Modeling of a micro-diaphragm for an optical pulse pressure sensor.
- ii. Simulation study of micro-diaphragm performance for polyimide and silicon nitride using the MEMS technology.
- iii. Optimization of the design parameters using the statistical method of Taguchi

1.4 Organization of Thesis

This thesis is divided into five chapters and these include introduction, literature review, design methodology, result and analysis as well as conclusions and future works.

Chapter 1 outlines a general introduction, objective and scope of work for this study.

Chapter 2 discusses the literature review and background studies on the pulse pressure sensor. It covers the review on arterial stiffness and BioMEMS sensing principles. This chapter also describes some previous studies studying on the performance of the micro-diaphragm and diaphragm materials. In addition, it also presents a review on the design optimization techniques.

Chapter 3 specifically explains the design methodology of the research methodology used for the present study. It includes designing a micro-diaphragm for the optical pulse pressure sensor and analysis of the micro-diaphragm performance. This chapter also covers the optimization using the Taguchi method. In this chapter, a statistical approach was used in order to attain an optimum micro-diaphragm performance.

Chapter 4 describes the results and analysis of the micro-diaphragm performance with the variation of the design parameters. Furthermore, this chapter also presents the results derived from the statistical analysis of the Taguchi method.

Finally, Chapter 5 discusses the overall conclusion and offers some recommendations for future work.

CHAPTER 2

LITERATURE REVIEW

2.1 Introduction

In this chapter, the literature review on arterial stiffness, BioMEMS pressure sensor, diaphragm performance and materials are discussed. Meanwhile, Section 2.2 reviews mechanisms of arterial stiffness and its diagnosis techniques. There are five diagnosis techniques discussed in this chapter and these includes intravascular ultrasound (IVUS), magnetic resonance imaging (MRI), angiography, pulse wave analysis and biomedical pressure sensor.

BioMEMS pressure sensors are discussed in Section 2.3. The performance of micro-diaphragm and micro-diaphragm materials are elaborated in Sections 2.4 and 2.5 respectively. Section 2.6 reviews the design optimization techniques. Finally, Section 2.7 concludes the literature review.

2.2 Arterial Stiffness

The literature review on arterial stiffness is further divided into two parts, namely the mechanism of arterial stiffness and the diagnosis techniques of arterial stiffness.

2.2.1 Mechanism of Arterial Stiffness

Arterial stiffness is a growing epidemic associated with increased risk of cardiovascular diseases, dementia, morbidity and mortality (Zieman *et al.*, 2005). It is a hardening and stiffening process of the arteries. During the stiffening process, the artery will be narrowed due to the deposition of fats and cholesterols known as plaques.

These plaques consist of three main components referred to as atheroma, cholesterol layers and calcification at the outer base of the artery. The atheroma is a nodular accumulation of soft material at the centre of the plaques. The plaques can grow large enough to decrease elasticity of the arteries and reduce the blood flow through the arteries (Latifoglu *et al.*, 2007). In addition, it will increase the thickness and rigidity of the arterial walls. Figure 2.1 shows the stiffening process of the artery.

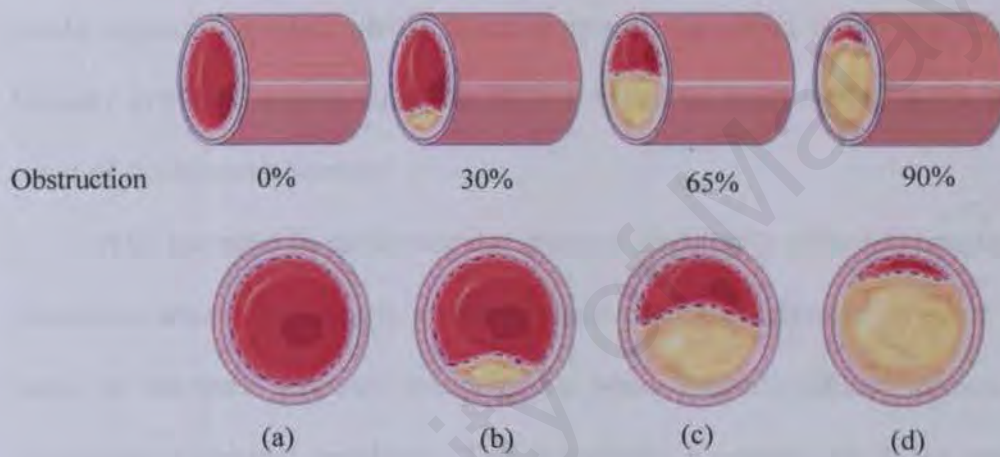


Figure 2.1: Stiffening process of the artery (a) normal artery (b) 30% obstruction in the artery (c) plaques in the blood vessel (d) Plaques reduce the blood flow in the artery (adapted from Servier Medical Art 2008)

The arterial stiffness may eventually lead to plaque ruptures and stenosis (narrowing of the artery). Thus, the body will receive insufficient blood supply. The soft plaques in the arteries will rupture and cause the formation of the thrombus. The thrombus will rapidly stop the blood flow and lead to death of the tissues fed by the arteries. This phenomenon is called infarction (Alty *et al.*, 2007). Infarction is known as a major cause of coronary artery disease such as stroke, hypertension and heart attack.

Arterial stiffness typically begins in early adolescence, and it is usually found in most major arteries (Alty *et al.*, 2007). Recent studies have shown that arterial stiffness increases with age (Kopeć *et al.*, 2009). It is also associated with cardiovascular risks including hypertension (Nichols *et al.*, 1990), diabetes mellitus (Lehmann *et al.*, 1992), atherosclerosis (Wada *et al.*, 1994) and end-stage renal failure (London *et al.*, 1990).

The World Health Organization (WHO, 2008) predicts that by 2010 cardiovascular diseases would also be the leading killer in the developing world and it would represent a major global health problem. According to the statistic from the Ministry of Health (MOH, 2008) for 2008 in Malaysia, heart disease is the number one cause of death in this country.

The increases in cardiovascular diseases are closely related to arterial stiffness. Moreover, arterial stiffness is asymptotic and cannot be detected by most diagnostic tools. It becomes seriously symptomatic when arterial stiffness affects coronary circulation or cerebral circulation. This is typically happened due to the rupture of an atheroma and blood clot.

It is important to note that arterial stiffness has been implicated in the development of isolated systolic hypertension. This disease mainly affects the elderly population and is always associated with considerable excess morbidity and mortality. In addition, arterial stiffness may act as a marker for development of future atherosclerosis or it may also be more directly involved in the process of atherosclerosis.

Currently, pulse pressure is used as a predictor for most cardiovascular diseases such as myocardial infarction, arterial stiffness and congestive cardiac failure. As briefly discussed in Chapter 1, high pulse pressure (> 40 mmHg) is a predictor of the

cardiovascular diseases which include arterial stiffness and atherosclerosis (Alty *et al.*, 2007).

Although, most of the measurement techniques are focusing on experimental and physiological studies at present, arterial stiffness can be measured using a variety of techniques. Nevertheless, it is likely that over the next few years measurement of arterial stiffness will become an increasingly important part of the process of risk assessment, and may possibly also improve the monitoring of therapy in patients with conditions such as isolated systolic hypertension. Therefore it has become necessary for physicians to understand the importance of arterial stiffness and all the techniques available for clinical assessment.

2.2.2 Diagnosis Techniques for Arterial Stiffness

In order to obtain parameters such as distension and arterial stiffness, the movement of the arterial walls during pulsation must be accurately detected. Several techniques have been used in the recent years. These include MRI, angiography, IVUS, pulse wave analysis and biomedical pressure sensors.

(i) Magnetic Resonance Imaging

Magnetic Resonance Imaging (MRI) is an imaging technique used primarily in medical settings to produce high quality images inside the human body (Hossain and Abedin, 2008). It provides detailed images of the body in any plane. MRI is potentially useful and can be used as an effective diagnostic tool in basic research, clinical investigation and disease diagnosis (Yu and Zhao, 2008).

In addition, the MRI also provides both chemical and physiological information about the tissue under investigation (Yu and Zhao, 2008, Hautvast *et al.*, 2006). It is based on the principles of nuclear magnetic resonance (NMR). The NMR is a

spectroscopic technique used by scientists to obtain microscopic chemical and physical information about molecules (Hossain and Abedin, 2008).

The MRI was initially used as a tomographic imaging technique which produced an image of NMR signal in a thin slice through the human body (Hossain and Abedin, 2008, Frahm *et al.*, 1987). The human body is mainly composed of water molecules in which each molecule contains two hydrogen nuclei or protons. Besides water molecules, it also contains fat. Fat and water have many hydrogen atoms, which make the human body to have approximately 63 % hydrogen atoms. Hydrogen nuclei have an NMR signal (Hossain and Abedin, 2008, Frahm *et al.*, 1987).

For these reasons, the MRI is primarily images of NMR signals from the hydrogen nuclei. Each of the human body images contains one or more tissues. Meanwhile proton possessed a property called spin which can be thought of as a small magnetic field, and it will cause a nucleus to produce an NMR signals (Hossain and Abedin, 2008, Sebastiani *et al.*, 1996, Matter *et al.*, 2006).

The MRI provides a much greater contrast between the different soft tissues of the body than a computed tomography does, making it especially useful in neurological (brain), musculoskeletal, cardiovascular, and oncological (cancer) imaging. In cardiovascular diagnosis, a non-invasive assessment of atherosclerosis is important. Figure 2.2 shows the MRI scanner of the human body. Advancements in the MRI have made it possible to obtain high resolution and in-vivo visualization of atherosclerosis plaque of complex composition (Imai *et al.*, 2006).



Figure 2.2: Magnetic Resonance Imaging Scanner (adapted from draimaging 2009)

However, many magnetic resonance signals encounter problem in low signal-to-noise ratio. Magnetic resonance magnitude image noise is usually modelled by Richian Distribution (Yu and Zhao, 2008, Gravel *et al.*, 2004). Richian noise is not zero-mean, and the mean depends on the local intensity in the image. Thus, the estimation of the magnetic resonance image from the noisy data is especially challenging because of this complication.

(ii) Angiography

Coronary X-ray angiography is currently the standard imaging technique used in diagnosing coronary artery disease (Hansis *et al.*, 2008). The coronary artery disease (CAD) is a condition when plaque builds up inside the coronary arteries. Angiography is conducted by injecting a radio-opaque contrast agent into the blood vessel and the X-ray based technique is used for imaging.

Angiography is mostly done through femoral artery. Using guide wires and catheters, a contrast agent is added to the blood to make it visible in x-ray images

(Bartsch *et al.*, 1996). Two dimensional projection images of selectively contrast agent enhanced arteries are usually analyzed directly.

However, a 3-D reconstruction of the coronary arteries would offer great advantages. The 3-D reconstruction of the coronary arteries is performed from rotational projection data of selective contrast agent. It is enhanced coronary arteries, acquired on an X-ray C arm system with simultaneous electrocardiogram (ECG) recording (Hansis *et al.*, 2008).

Angiography has been the standard for evaluating the extent of coronary artery disease. However, pathologic studies have indicated that the angiography images of coronary arterial stiffness are underestimated by 'normal' coronary artery segments (Mintz *et al.*, 1995). Furthermore, angiography is invasive and has relatively high cost.

(iii) Intravascular Ultrasound

Intravascular Ultrasound (IVUS) is a medical imaging technique which uses a catheter with a miniaturized ultrasound probe that can determine both plaque volume within the arteries wall and stenosis of the arteries lumen. The IVUS enables assessment of morphology and distribution of *in vivo* atherosclerosis plaque (Yamagishi *et al.*, 1999). Figure 2.3 shows the assessment of arterial stiffness using IVUS.



Figure 2.3: Duplex ultrasound probe (adapted from Stocktoncardiology, 2009)

The IVUS can visualize the lumen of the arteries. Therefore, the IVUS is normally used to determine both plaques volume within the arteries wall and the degree of stenosis of the artery lumen. It can be useful in situation in which an angiographic image is considered unreliable. In addition, the IVUS has been reported (Yamagishi *et al.*, 1999) to be used in assessing the effects of medical treatment of stenosis.

However, IVUS is time consuming and can only be performed by a technician who is trained in interventional cardiology techniques. The IVUS uses significant additional examination time and increased risk to the patient beyond performing a standard diagnostic angiographic examination. Moreover, there may be additional risk imposed by the use of the IVUS catheter.

(iv) Pulse Wave Analysis

Noninvasive radial artery pulse wave has been widely used for assessment of arterial stiffness. Shape of the arterial pulse waveform provides a measure of systemic arterial stiffness. The arterial pulse waveform can be assessed noninvasively using the pulse wave analysis (PWA) technique (Wilkinson *et al.*, 2002).

PWA is a non-invasive method which measures small vessel and large vessel compliances derived from the radial artery. The PWA detects changes in the blood flow through the vessels and calcified arteries (Thompson *et al.*, 2008). Calcification changes the blood vessel and flow characteristics. The study involving an arterial pulse wave analysis has shown its potential in indicating physiological changes due to the arterial stiffness or peripheral vascular disease.

The arterial pressure waveform was first recorded and analyzed at the end of the 19th century. The waveform was recorded using sphygmograph (Mackenzie *et al.*, 1995). Since then, numerous methods have been used to detect the arterial pulse pressure. They

include the vasculograph (Lax *et al.*, 1958), invasive devices and more recently, the non-invasive tonometer.

The arterial pressure waveform is composed of a forward pressure wave and a reflected wave. Waves are reflected from the periphery mainly at branch points. The velocity at which the pressure wave travels is influenced by the stiffness of the arteries. The stiffer arteries will result in higher velocity of pulse wave. In elastic vessels, the reflected wave tends to arrive back at the aortic root during diastole (Lax *et al.*, 1958, Mackenzie *et al.*, 1995).

However, in the case of stiff arteries, the reflected wave arrives back at the central arteries earlier. Thus, it will cause augmentation of the systolic pressure and a consequent decrease in diastole pressure. Figure 2.4 shows radial pulse contour derived from the radial artery. The radial artery waveforms can be derived non-invasively using a simple non-invasive method of measuring arterial stiffness, tonometer.

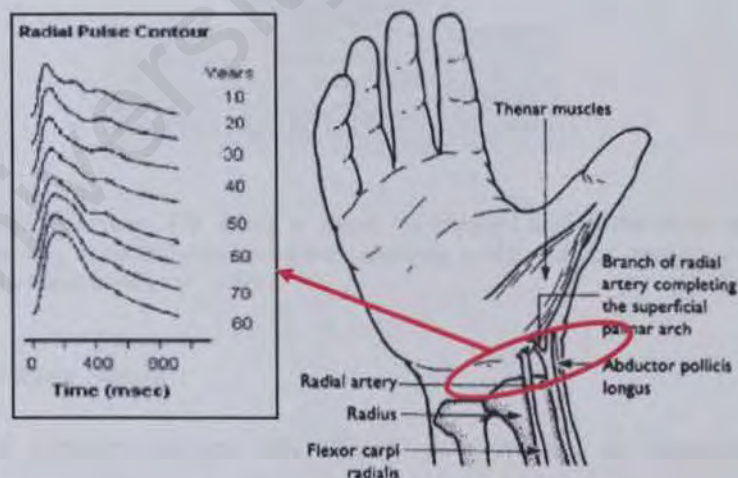


Figure 2.4: Radial pulse contour derived from the radial artery (adapted medstudents, 2009)

As illustrated in Figure 2.5, the tonometer is used to record pulse pressure at radial or carotid arteries. It consists of an array of pressure transducer which used a

modified Windkessel model of the circulation and an assessment of diastole pressure decay (Mackenzie et al., 1995). The arterial pressure waveform is measured at the site where the strongest pulse is detected (Tyan *et al.*, 2008).

However, certain patients with vascular diseases or unusual physiques have smaller and weaker radial artery's pulses. Thus it is difficult to find the position of the strongest pulsation, thereby making it impossible to measure the optimal pulse. In addition, the tonometer is operator depended and it is also very sensitive to movements. Therefore, it is challenging to record a stable radial pulse waveform using the tonometer.

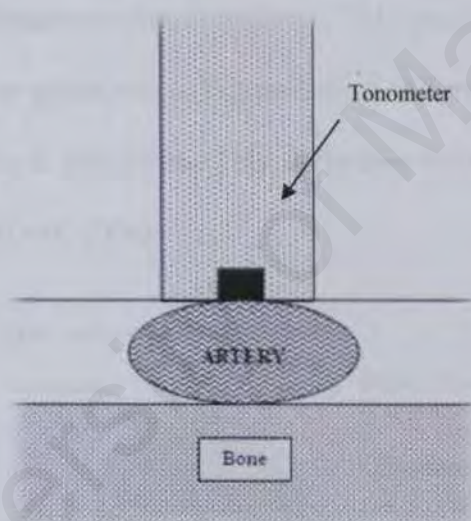


Figure 2.5: Principle of tonometer. The artery is gently compressed against the underlying bone, thus flattening it and equalizing circumferential pressures, allowing a high-fidelity pressure waveform to be recorded (adapted from Mackenzie et al., 1995).

(v) Biomedical Pressure Sensor

Biomedical pressure sensor has shown its potential in diagnosing arterial stiffness. Diagnosis of arterial stiffness can be conducted by detecting the pulse pressure on the human's radial artery.

There are two approaches used in biomedical pressure measurements namely direct pressure and indirect pressure measurements. The direct pressure measurement refers to the assessment of the pressure using a sensor which is in contact with blood or fluid in human body (Dorf, 2006). Through invasive techniques the sensor experiences physical connection with circulating blood or measured fluid.

However, the indirect pressure measurement involves a sensor which does not have any invasive measurements. The most familiar indirect pressure measurement is arterial pressure measurement. The primary sensor used for indirect arterial pressure measurement is a strain gauge pressure transducer. This sensor consists of a diaphragm which is attached to a four gauge wires (Figure 2.6). A differential pressure seen across the diaphragm will cause a deflection. This deflection will then be measured by a displacement transducer (Dorf, 2006).

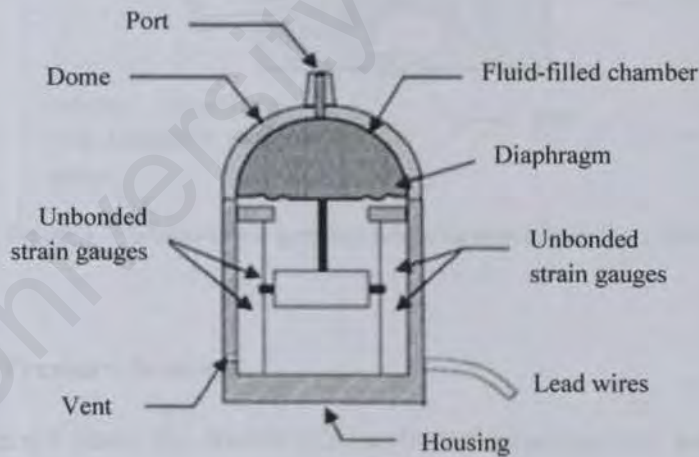


Figure 2.6: Unbonded strain gauge pressure sensor (adapted from Dorf, 2006)

Advances in the semiconductor technology have been applied in designing the biomedical pressure sensor. Therefore, smaller and less expensive sensor can be

designed. Silicon strain gauge was developed using this technology. It is more sensitive than the previous design. In addition, a chip which consists of a diaphragm with strain gauge integrated into its surface was also designed using this technology. The sensor structure is shown in Figure 2.7:

Nevertheless, there is a critical need for a miniature ultra-low pressure transducer (Noh *et al.*, 2003). Many sensing principles such as piezoresistive, capacitive and optical have been reported for biomedical pressure sensors. The rapid expansion in Biological Micro-electro-mechanical Systems (BioMEMS) has enabled sensor miniaturization for arterial pressure measurements. Extended reviews on the BioMEMS technology will be explained in the following section.

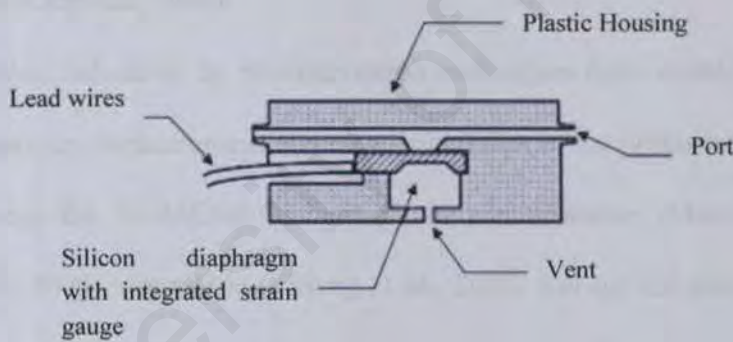


Figure 2.7: Silicon-based pressure sensor (adapted from Dorf, 2006)

2.3 BioMEMS Pressure Sensors

In the recent years, the BioMEMS has become increasingly prevalent and it has also been used in a wide variety of applications such as diagnostics, therapeutics and tissue engineering. The inception of the MEMS technology in 1970s, led to the realization of the significance of the biomedical applications of these miniature systems. As a result, the BioMEMS has emerged as a subset of the MEMS devices for

applications in biomedical research and medical micro-devices (Saliterman, 2006). It can typically be considered as having a dimension in micron range (~ 100nm to 200µm). Derived from the microfabrication technology, BioMEMS is expected to revolutionize the way medicine is practiced and delivered.

In general, BioMEMS integrate micro-scale sensors, actuators, microfluidics, micro-optics, and controls for application in medicine (Polla,2001, Cheung, 2005). These devices and systems encompass all interfaces of the life sciences and biomedical disciplines with micro-scale and nano-scale systems (Bashir, 2004). The ability to apply batch fabrication methods in the BioMEMS manufacturing enables a greater accessibility to the medical procedures through a lower overall cost of health care delivery system (Grayson, 2004).

In addition, advances in miniaturization techniques have enabled non-invasive arterial pulse pressure measurement. The miniaturization of the pressure sensor has been done by utilizing the BioMEMS technology in piezoresistive (Marco *et al.*, 1996, Pramanik *et al.*, 2006), capacitive (Chiang *et al.*, 2007) and optical sensor (Toshima *et al.*, 2003, Dagang *et al.*, 2006).

2.3.1 Piezoresistive

Ever since the piezoresistive effect in the semiconductor materials was developed (Kerr and Milnes, 1963Smith 1954), it has widely been applied to manufacture piezoresistive sensor (Marco *et al.*, 1996). The piezoresistive sensor consists of four resistors which are arranged in a Wheatstone bridge circuit (McCready *et al.*, 2002).

It is usually made by placing the sensing resistors on the top of the silicon diaphragm. When the diaphragm is loaded with an applied pressure, the resultant strain

from the deflected diaphragm will change the resistance value of the sensing resistors (McCready *et al.*, 2002). The variation of resistivity with strain is then exploited to obtain an output signal proportional to the input force.

In the late 1950's, the piezoresistive pressure sensor became available for biomedical applications. The sensor was designed for intravascular pressure measurements. Millar Instruments miniaturized this sensor and placed it in a catheter. Nevertheless, the resulting product was fragile and very expensive. Thus, it was only applicable in restricted applications.

Using thin membrane, Marco *et al.* 1996 developed a piezoresistive pressure sensor for invasive pressure measurements. This particular sensor is capable of direct pressure measurement and it is also more linear than the available pressure sensors. Pramanik *et al.* 2006 maximized the performance of the piezoresistive sensor by optimizing the doping concentration and geometry of the sensor.

Nevertheless, biocompatibility issues should be taken into consideration when designing a biomedical sensor. Even though piezoresistive transducers are more linear than capacitive detection, a non-negligible nonlinearity appears when high sensitivity and accuracy are simultaneously required (Marco *et al.*, 1996, He and Yang, 2006).

A major problem associated with the piezoresistive pressure sensor is its inherent cross sensitivity to temperature. Other disadvantages of the piezoresistive pressure sensor include large power consumption and strict requirement for sensing resistors placement to obtain maximum sensitivity (Xu, 2005).

2.3.2 Capacitive

On the contrary, to the piezoresistive pressure sensor, capacitive sensor generates an electrical signal because of an elastic deformation of a diaphragm. Capacitive sensor

is a noncontact device used for precision measurement of a conductive or a nonconductive material (Wilson, 2005).

Non-contact capacitive sensor operates by measuring changes in an electrical property called capacitance (Wilson, 2005, Lion Precision, 2009). In more specific, capacitance describes how two conductive objects with a space between them respond to a voltage difference applied to them. Figure 2.8 and 2.9 show an electric field is created between them and causing positive and negative charges to collect on each conductive object (Lion Precision, 2009).

However, capacitance is affected by three things: the sizes of the probe and target surfaces, the distance between them, and the material used in the gap. Theoretically, the intrinsic sensitivity of the capacitive pressure transducer can be much greater than piezoresistive transducer (Ko *et al.*, 1982). The capacitive structure is also expected to be free from some of the effects which cause baseline drift in piezoresistive pressure transducer (Ko *et al.*, 1982).

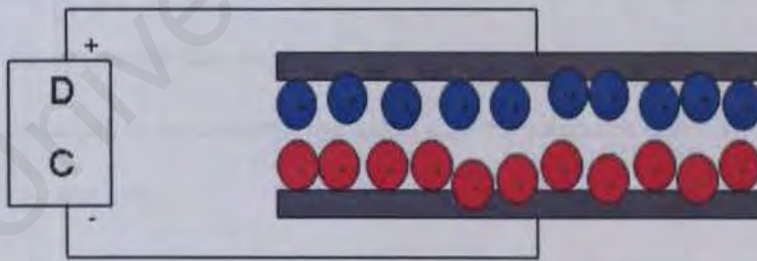


Figure 2.8: Applying a dc voltage to conductive objects (adapted from Lion Precision, 2009).

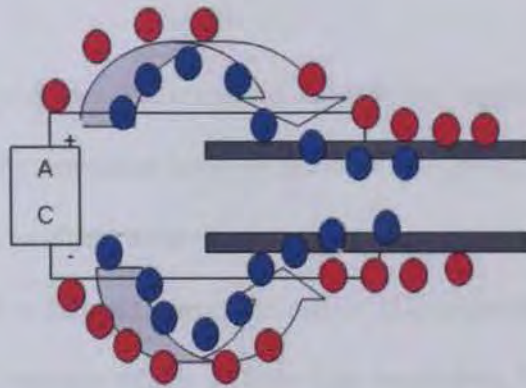


Figure 2.9: Applying an alternating current to conductive objects (adapted from Lion Precision, 2009).

A number of MEMS capacitive pressure sensors have been developed for biomedical applications. In 1980, capacitive pressure sensor was first fabricated using the MEMS technology (Sander *et al.*, 1980). The main structure of this particular sensor is a chamber. When a pressure is loaded onto the chamber, the capacitance will change. The measuring range was from 0 to 300 mmHg and the sensor was specifically designed for biomedical application. Extensive reviews on the MEMS capacitive sensor were conducted by Puers, 1993.

Habibi *et al.*, 1995 used the glass as the substrate to design capacitive pressure sensors. The sensors were designed using the surface micromachining technology. The sensors were arranged in an array on the glass substrate and the measuring range of these sensors was 0 to 800 kPa.

The capacitive pressure sensor has shown good performance in terms of sensitivity and power consumption. However, electrical connections to the sensor are very sensitive to noise. This is because of the small electrical capacitance. Therefore, it is desired to make the connections as short and well defined as possible, and this makes creating a sensor packaging a big challenge (Xu, 2005).

2.3.3 Optical

Miniature sensors are preferred in biomedical applications because of the minimized effect on the measured systems (Zhu *et al.*, 2005). Significant efforts have been exerted to fabricate these miniature sensors, electrically or optically interrogated. Compared to capacitive and piezoresistive sensor (Goustouridis *et al.*, 1998), optical sensor has several advantages which include high resolution, high sensitivity, intrinsic electrical passivity and immunity to electromagnetic interference (Zhu *et al.*, 2005, Totsu *et al.*, 2003, Tohyama *et al.*, 1998).

Optical pressure sensor typically utilizes a sensor head which consists of a micro-diaphragm and optical fibre. The optical pressure sensor converts the light rays to an electric signal. Therefore the micro-diaphragm is one of the most important parts in the optical pressure sensor. It is because the sensitivity of the sensor is highly dependent on its performance (Noh *et al.*, 2003).

High resolution and wide dynamic range afforded by optical detection provides a good combination with the demands of the MEMS pressure measurements. Therefore, several optical systems have been developed for measuring the displacement or deflection in the MEMS devices. The optical pressure measurements techniques can be categorized as interferometric and non-interferometric (Tayag *et al.*, 2003).

The non-interferometric technique typically modulates the power which is coupled into an optical fiber to ensure that it is proportional to the deflection of the MEMS sensor. This technique includes the optical-beam deflection method (Shin *et al.*, 1998), the shutter method and the lever method (He and Cuomo, 1991).

Meanwhile, the interferometric technique can be divided into two namely, single-point measurement technique and full-field optical measurement technique

(Tayag *et al.*, 2003). The single-point measurement technique measures the transverse deflection at a single point on the MEMS structure. Therefore, it is proven that linear and two-dimensional deflection data can be obtained using this approach.

The full-field optical measurement is a non-contact measurement method in which various physical quantities such as position, deflection, and stresses are measured as two-dimensional distribution. It is based on the images taken by a camera to give real time distribution data. The full-field optical measurement technique includes holographic interferometry (Wernicke *et al.*, 1998), moiré interferometry (Hart *et al.*, 1999) and stroboscopic interferometry.

A new optical pressure sensor design emerged in the late 1970's and early 1980's (Matsumoto *et al.*, 1978). The sensor design is based on Fabry-Perot Interferometer (Belsley *et al.*, 1986). The Fabry-Perot Interferometer is typically made of a transparent plate with two reflecting surfaces. In this design, one of the two parallel optical reflecting surfaces acts as a pressure sensitive micro-diaphragm. Fabry-Perot reflectance peak change accordingly when the micro-diaphragm responds to the pressure. However, this design required complex signal analysis instrumentation.

A dual-channel non-invasive optical sensor system was developed by Singh *et al.*, 1990. The sensor is used for simultaneous recording of carotid and radial artery pulses. Pressure pulsations detected on the artery cause the micro-diaphragm to be deflected. Thus, the deflected micro-diaphragm changes the reflected light spectrum. Nevertheless, the sensor systems require further improvement so as to obtain a continuous monitoring of arterial pressure waveform.

Interferometric pressure sensor for intravascular blood pressure measurement was developed by Hill *et al.* 2007. The Fabry-Perot Interferometry is formed between a

reflective micro-diaphragm and the optical fibre's end. Using SU-8 as the diaphragm material, Hill *et al.* 2007 showed that the sensor achieved linear response to pressure with satisfactory resolution for the intravascular blood pressure measurements.

The optical MEMS pressure sensors for biomedical applications were designed and reviewed in (Dagang *et al.*, 2006, Cibula *et al.*, 2002, Toshima *et al.*, 2003, Wang *et al.*, 2005 and Tohyama *et al.*, 1998). The optical MEMS have shown the potential in designing a biosensor. Reviews have shown that the optical MEMS are suitable for non-invasive measurements of pulse pressure waveform on human radial artery.

2.4 The Performance of Micro-Diaphragm

Designing a micro-diaphragm for an optical sensor can be successfully done by analyzing the performance of micro-diaphragm. Among all the elastic plates, the micro-diaphragm is not only simple to construct, but it is also suitable in high vibration environment (Giovanni, 1982). Moreover, the micro-diaphragm is a flexible plate which undergoes elastic deflection when a lateral pressure is applied onto it.

Deformation of the loaded micro-diaphragm will determine the performance and sensitivity of the complete sensor system. Thus, it is crucial to design a micro-diaphragm which can operate with optimum performance. Diaphragm deflection, diaphragm pressure sensitivity and frequency response of the diaphragm are the most important parameters to be considered in designing the micro-diaphragm.

Numerous researchers have investigated the performance of micro-diaphragm for the optical sensor. Among other extensive reviews on the performance characteristics of micro-diaphragm have been conducted by Xu, 2005 and Deng, 2004. Both the researchers analyzed the performance of micro-diaphragm for optical MEMS pressure

measurement of gas turbine engine and real-time detection of acoustic emissions in power transformer respectively. The studies have shown that the performance of micro-diaphragm become less sensitive when the diaphragm is thick (Xu, 2005, Deng, 2004)

In addition, the relationship between diaphragm deflection and applied pressure has been analyzed by Le *et al.*, 2005, and Dagang *et al.*, 2006. The researchers found that the diaphragm deflection increases linearly when the applied pressure increases. Therefore a micro-diaphragm which has a linear relationship between diaphragm deflection and applied pressure is highly desirable since it is easy to calculate and measure. This linear relationship between deflection and applied pressure is achieved when the maximum deflection is not more than 30 % of the diaphragm thickness (Giovanni, 1982, Xu, 2005, Deng, 2004).

Besides diaphragm deflection, sensitivity is another important parameter to be considered in designing the diaphragm. The determination of diaphragm pressure sensitivity partially defines the sensitivity of a complete sensor system. The diaphragm pressure sensitivity is defined as the ratio of the deflection to the applied pressure. Analysis presented by Sheplak and Dugundji, 1998, showed that a diaphragm with high sensitivity is desirable since it measures how sensitive the diaphragm deforms with the applied pressure.

Resonance frequency of the diaphragm is another important parameter to be considered in any diaphragm performance analysis. High sensitivity diaphragm reduces the diaphragm resonance frequency (Sheplak and Dugundji, 1998, Xu, 2005, Deng, 2004). Thus, it is crucial to select design parameters which give the highest sensitivity without affecting diaphragm resonance frequency. Therefore, there is a need to find the optimum design parameters to achieve the diaphragm with the best performance.

2.5 Micro-Diaphragm Material

Material for the micro-diaphragm is chosen based on its applications. The selection of the most suitable material for the micro-diaphragm is also a crucial part in designing an optical pulse pressure sensor. Since the micro-diaphragm acts as a pressure sensitive element, it must have a high sensitivity to ensure the performance of the optical pulse pressure sensor. The optical pulse pressure sensor must have an adequate detection system to measure small micro-diaphragm deformation. Therefore, suitable material needs to be chosen to ensure the micro-diaphragm is sensitive for small pulse pressure measurements.

There are five main categories of MEMS materials as shown in Figure 2.10. The structural material or substrate material must be able to withstand the various process steps. Spacer materials are usually completely or partially etched away to release the microstructure. In addition, it may also be used to make moulds for structures and protect the substrate or structural material from certain etching steps. Surface materials are also important for achieving electrical isolation. Besides that, active materials are incorporated on structures to exploit their special physical transduction characteristics.

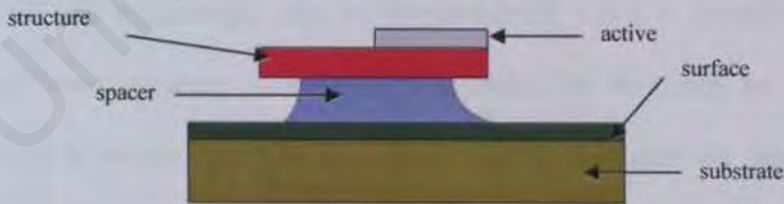


Figure 2.10: Categories of micromechanical materials (adopted from Bustillo et al., 1998)

Figure 2.11 shows the material properties in the MEMS. These material properties can be divided into a few categories which include mechanical and electrical properties of material. Mechanical properties include Young's modulus, shear stress,

residual stress and poisson's ratio (Park, 2003). Another material properties in the MEMS are processing, cost, thermal conductivity, biocompatibility, electro-chemical and optical.

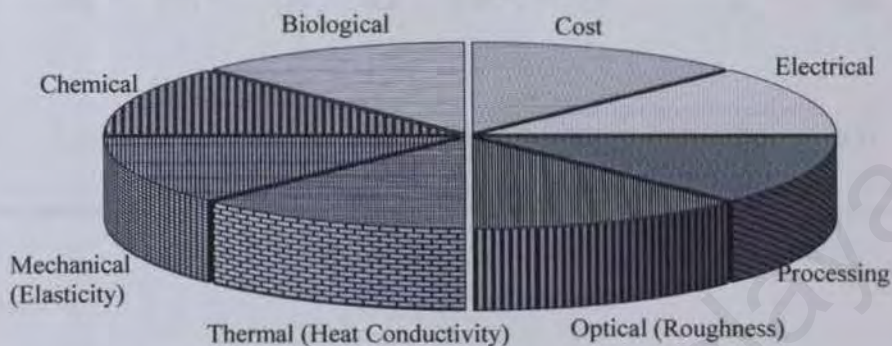


Figure 2.11: Material properties of the MEMS

In addition, a comparison of material properties for several MEMS materials is presented in Table 2.1. The material properties for silicon-, polymer- and metal- based materials are presented in terms of Young's Modulus and Poisson's ratio. Young's Modulus is a measure of the stiffness of an isotropic elastic material while Poisson's ratio is a ratio of the transverse strain to the extension of axial strain (Beards, 1996).

The MEMS technology can be implemented using a number of different materials and manufacturing techniques. The materials that can be used for the diaphragm include silicon, polymer and metal. Previous studies on micro-diaphragm material for biosensor are presented and these include silicon-based, polymer-based and metal-based materials.

Table 2.1: Comparison of material properties for silicon based, polymer based and metal based diaphragm materials

Material	Silicon based			Polymer based			Metal based		
Properties	Silicon	Silicon Nitride	Silicon Carbide	SU8	PDMS	Polyimide	Aluminum	Nickel	Magnesium metal
Young's Modulus (GPa)	150	270	410	4.4	0.87	7.5	70	200	45
Poisson's ratio	0.17	0.27	0.14	0.22	0.5	0.35	0.35	0.31	0.29

(i) Silicon

Silicon is a material used to create most integrated circuits in consumer electronics. Silicon has significant advantages engendered through its material properties. When it is flexed there is virtually no hysteresis and hence almost no energy dissipation (Madou, 2002).

Silicon is very reliable as it suffers very little fatigue and can have a service lifetime in the range of billions to trillions of cycles without breaking. The basic techniques for producing all silicon-based MEMS devices are deposition of material layers, patterning of these layers by lithography and etching. These techniques could be applied to produce the required shapes.

Totsu *et al.*, 2005 successfully developed an optical pressure sensor system using silicon diaphragm. The system directly detects the modulated spectrum of the reflected light from the sensor interferometer. By detecting the shift of the peak wavelengths from the spectrum, the cavity length is calculated and the measured pressure is continuously displayed.

The silicon diaphragm has been used to design a fiber-optic pressure micro-sensor for balloon catheters (Tohyama *et al.*, 1998). It is shown that the silicon is biocompatible and suitable in designing a biosensor. The developed sensor can be used for a wide range of medical applications such as minimally invasive surgery and microsurgery (Tohyama *et al.*, 1998).

In addition, silicon has been used in designing a piezoresistive pressure sensor for biomedical applications (Pramanik *et al.*, 2006, Marco *et al.*, 1996). Many researchers (Totsu *et al.*, 2005, Tohyama *et al.*, 1998, Pramanik *et al.*, 2006, Marco *et al.*, 1996) have shown that the silicon has a potential in invasive and non-invasive measurements. In more specific, the MEMS technology has enabled the usage of silicon-based materials. The silicon based materials such as silicon nitride, polysilicon and silicon dioxide are biocompatible and they are also commonly used for biomedical applications.

Polysilicon has been used to design a pressure sensor for cardiovascular pressure measurements (Kalvesten *et al.*, 1998). Kalvesten *et al.*, 1998 further showed that polysilicon could be used as a pressure sensor inside catheters. Meanwhile silicon nitride possesses few advantages for clinical and biomedical applications (Silva *et al.*, 2008). This is due to its high wear resistance and low friction coefficient. In addition, silicon nitride is a non-cytotoxic material and possesses satisfactory fracture roughness.

(ii) Polymer

Even though the electronic industry has widely used silicon, nevertheless crystalline silicon is still a complex and relatively expensive material to produce. However, polymer can be produced in huge volumes, with a great variety of material

characteristics. The MEMS devices can be made from polymers by processes such as injection moulding, embossing and stereolithography (Park and Bronzino, 2003).

Synthetic polymeric materials have widely been used in medical disposable supplies, prosthetic materials, dental materials, implants, dressings and polymeric drug delivery systems (Park and Bronzino, 2003). The main advantages of the polymeric biomaterials compared to metal and ceramic materials are the ease of manufacturability to produce various shapes, ease of secondary processibility, reasonable cost, and availability with desired mechanical and physical properties (Park and Bronzino, 2003).

Many researchers have been using polymer to design a micro-diaphragm for a biosensor (Cibula *et al.*, 2002, Hill *et al.*, 2007, Shin *et al.*, 2004, Chiang *et al.*, 2007, Melamud *et al.*, 2004, Nesson 2007, Pelletier *et al.*, 2005, Yu and Zhao, 2008). Among other Cibula *et al.*, 2002, designed a miniature optical pressure sensor for blood pressure measurement. The invasive design of the pressure sensor utilizes a thin polymer diaphragm which is inserted inside a hollow end of the optical fibre. The performance of the sensor is optimized for human blood pressure range (0 to 300 mmHg) with 1mmHg resolution (Cibula *et al.*, 2002).

Hill *et al.*, 2007 used biocompatible polymer, SU-8 to fabricate an interferometric pressure sensor. The sensor consists of a polymer cap with a reflective, pressure sensing diaphragm mounted onto the end of a fibre optic cable. The sensor is designed for invasive biomedical applications. It showed a linear pressure response from 0 to 125 mmHg with 1-2 mmHg resolution. Furthermore, the sensor shows promising results when tested in air and liquid environments.

However, there is a limitation involved when SU-8 is used as a critical material in micro-devices. The possible disadvantages of SU-8 include instability and

manufacturing process variability. The invasive biomedical commercial product with SU-8 as a critical material should be carefully tested in a representative environment and perhaps ship in fluid-filled packaging (Melamud *et al.*, 2005, Hill *et al.*, 2007).

A flexible wireless blood pressure sensor was developed using a chip embedded flexible packaging technology by Shin *et al.*, 2004. Polyimide is spin coated to act as flexible diaphragm. Polyimide diaphragm is mechanically flexible and it is wrapped onto the outside of the blood vessel. The pressure sensor consists of a flexible capacitance type sensor system. As blood pressure changes, the blood vessel either expands or shrinks. This sensor system detects blood pressure variation due to the changes in the distance between the electrodes (Shin *et al.*, 2004).

Meanwhile Chiang *et al.*, 2007 developed a micro capacitive pressure sensor for in situ monitoring of the interface pressure between implanted cuff and nerve tissue. In this study, the structure of the capacitive pressure sensor consists of two parallel electrical sensing plates. Polyimide is chosen as a material for insulating layers because it is biocompatible and can act as an insulator.

In vitro intradiscal pressure measurements of rodents have been successfully demonstrated by Nesson 2007. Nesson 2007 developed two different optical systems with novel miniature optical pressure sensors. The two different optical systems consist of intensity based sensor system and low coherence interferometry based sensor system. The pressure sensor was designed using polyimide diaphragm to measure pressure in rat discs without disrupting the structure and altering the intradiscal pressure.

Yu and Zhao, 2008 further improved the design by Nesson 2007. One of the unique features of this study is the design and fabrication of a sensor element with a multilayer polymer-metal diaphragm. The fabricated sensor showed better performance

than Nesson's design without disrupting the structure or altering the intradiscal pressures (Yu and Zhao, 2008).

It is proven in this review that the polymer-based materials have to be used in designing the micro-diaphragm for biosensor (Cibula *et al.*, 2002, Hill *et al.*, 2007, Shin *et al.*, 2004, Chiang *et al.*, 2007, Melamud *et al.*, 2004, Nesson 2007, Pelletier *et al.*, 2005, Yu and Zhao, 2008). Thus, these extensive reviews are beneficial and helpful in the selection of the most suitable diaphragm material.

(iii) Metal

Metals can also be used to create MEMS devices. Metals exhibit a very high degree of reliability. Besides that, metals are used as biomaterials due to their excellent electrical, thermal conductivity and mechanical properties. Since some electrons are independent in metals, they can quickly transfer an electric charge and thermal energy.

The mobile free electrons act as a binding force to hold the positive metal ions together (Park and Bronzino, 2003). Moreover, the attractions between electrons are strong. This is due to the closely packed atomic arrangement. As a result, most metals have high specific gravity and high melting points (Park *et al.*, 2003).

However, metal is rarely used as a sensing element for small range of pressure measurements. This is because metal possesses high stiffness and high Young's Modulus as presented in Table 2.1. Since the sensor is designed for pulse pressure measurement and operating in small deflection measurements, metal is not suitable for this particular study. On the contrary, materials with low Young's Modulus are more suitable for small pulse pressure measurements.

A513413525

2.6 Design Optimization Techniques

In this study, the performance of micro-diaphragm will determine the performance of a complete sensor system. Deviation in the performance of micro-diaphragm due to the design parameter variations should be taken into consideration in the early MEMS design stage. However, these design parameters have not been considered during device-level and system-level design stages in MEMS software. Thus, overall performance of micro-diaphragm is affected.

Since size of MEMS micro-diaphragm approach the micron and submicron range, its performance is more sensitive to design process variations. In addition, there is possibility that the material used in the micro-diaphragm is poorly characterized (Hsiung, 2006). Further complicating the design process is the difficulty of making measurements at the micrometer scale. As a result, most performances of the micro-diaphragm have large uncertainties associated with their variations in design parameters.

Thus, a robust design method is needed to ensure the micro-diaphragm achieve its best performance. If the micro-diaphragm is not robust to design variations, exhaustive post-fabrication screening or calibration is often required. In other words, the micro-diaphragm must be optimized and perform its intended functions with minimized noise factors (Basem, 2005).

Therefore, to successfully design the best performance of micro-diaphragm, the optimization methods such as six-sigma quality strategy (Basem, 2005, Coleman *et al.*, 2000), reliability-based design (Zhang *et al.*, 2005, Kuo *et al.*, 2001, Haldar & Mahadevan, 2000, Maute & Frangopol, 2003), robust optimization (Basem, 2005) and genetic algorithm (Darnoby *et al.*, 2008) have been applied in optimizing the performance of MEMS devices.

Darnoby et al., 2008 used genetic algorithm in designing MEMS element (Darnoby et al., 2008). The inductive nature of genetic algorithm does not require knowledge in any rules of the problems. However, it requires more computational time for the genetic algorithm search process (Darnoby et al., 2008).

Besides that, a six-sigma quality strategy was used as the earliest approach to reduce the design variations (Zhang et al., 2005). It is an organized and systematic problem solving method for strategic system improvement and development. The six-sigma strategy is classified into two approaches namely reliability-based method and robust design-based method.

The difference between structural robustness and reliability is shown in Figure 2.12. The reliability-based method estimates the probability distribution of the system's response based on the known probability distributions of the random parameters. Maute and Frangopol, 2003 combined topology and reliability-based method in order to provide a stochastic method for compliant the MEMS design. However, in this method, the variation is not minimized since it only concentrates on rare events at the tails of the probability distribution (Basem et al., 2005).

Meanwhile, the robust design improves product quality by minimizing the effects of variation causes without eliminating them. In 1951, Fisher has developed a statistical design of experiment (DOE) approach to improve the yield of agricultural crops (Fisher, 1951). DOE refers to the processes of planning, designing and analyzing process variables or factors to achieve valid result in an effective way.

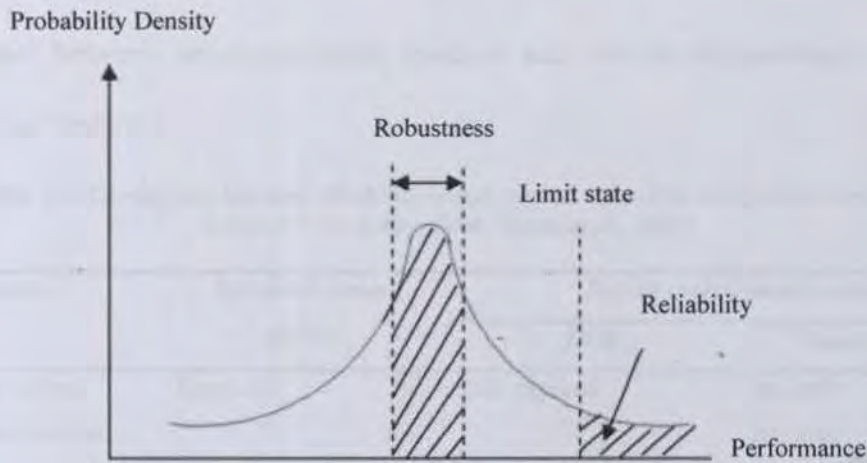


Figure 2.12: The difference between structural robustness and reliability

Unfortunately, in most situations, time is limited and the DOE methods tend to be lengthy and cumbersome. The DOE is a structured, organized method which is used to determine the relationship between the different factors affected a process and the output of that particular process. In order to optimize the design with such restrictions, a more efficient experimental method is needed.

In 1950s and early 1960s, Taguchi developed a methodology as a foundation of robust design to produce high quality products. This methodology has simplified the procedure by advocating the use of fewer simulation runs. It also provides a clearer understanding of the variation nature and economic consequences of quality engineering (Tasirin *et al.*, 2007).

Although the concept in Taguchi method is similar to concept of DOE, this method only conducts balanced or orthogonal simulation combinations. Thus it makes the Taguchi method even more efficient than the fractional functional design. In addition, this method allows looking into variability caused by the noise factors, which are usually ignored in the traditional DOE approach (Taguchi, 1989). Summarized

comparison between reliability-based method and robust design-based method is presented in Table 2.2.

Table 2.2: Comparison between reliability-based method and robust design-based method (adapted from Kirby, 2006, Basemet *et al.*, 2005)

Aspect	Reliability-based method	Robust design-based method	
		DOE	Taguchi Method
Knowledge of the process being studied	Required	Not required	In-depth knowledge required
Number of test runs	Large	Relatively large – all combination of inputs	Much smaller number of combinations
Noise factors	Included	Usually not included	Included in the basic design
Variability of system being studied	Not minimized	Only used to look for most effective combination of inputs	Looks at both level and variability of output to select input combinations
Confirmation runs	Not required, as all combination of inputs are tested	Not required, as all combination of inputs are tested	Advisable; selected combination of inputs may not have been tested

Since enormous amount of time is required in order to reduce simulation trials, a number of researchers (Zhang *et al.*, 2005, Tasirin *et al.*, 2007, Sycros, 2003, Vijian and Arunachalam, 2007, Lai *et al.*, 2007) have used the Taguchi Method in various applications such as milling process, casting and for designing of MEMS devices (Zhang *et al.*, 2005, Tasirin *et al.*, 2007, Sycros, 2003, Vijian and Arunachalam, 2007, Kwak *et al.*, 2000, Lai *et al.*, 2007).

Zhang *et al.*, 2007 and Sycros 2003 used Taguchi method to optimize surface quality in the CNC machine and to obtain setting of a die casting parameters respectively. In addition, Tasirin *et al.*, 2007 demonstrated the application of Taguchi's

method in food engineering. The method was used in optimizing the drying parameters of bird's eye chilies in fluidized bed dryer (Tasirin *et al.*, 2007).

The Taguchi method was also applied in the robust optimal design of the MEMS structure in Kwak *et al.*, 2000. In addition, Kwak *et al.*, 2000 proved that the Taguchi method relieved much of the difficulties often encountered in most conventional design works. The method has also been found to be practical for the structural design of the MEMS. The optimal design of microwave MEMS switches by the Taguchi method is also presented in Lai *et al.*, 2007. The structures of the switches are analyzed and optimized so as to improve the reliability and performance of the MEMS switches.

Research findings have shown that the Taguchi Method is a powerful tool for high quality systems design (Zhang *et al.*, 2007, Sycros, 2003, Tasirin *et al.*, 2007, Vijian and Arunachalam, 2007). The findings also demonstrated that this method provides simple, efficient and systematic approaches to optimize the performance, quality and cost of the robust design. Thus, the Taguchi method was chosen in determining the optimum design parameters to be used in constructing the best performance of the micro-diaphragm.

2.7 Summary

In this chapter, the arterial stiffness and its diagnosis techniques were extensively reviewed. Reviews on micro-diaphragm performance and material as well as design optimization techniques have been presented. Therefore, it can be concluded that the arterial stiffness can be diagnosed by detecting the pulse pressure on the human's radial artery.

The review has revealed that the optical sensing principle has a good potential to be used in designing the pulse pressure sensor. Miniaturization technology in the MEMS enabled the design of the miniature optical pulse pressure sensor.

Previous studies by Xu, 2005, Deng, 2004, Giovanni, 1989, Le *et al.*, 2005, Dagang *et al.*, 2006 have concluded that the diaphragm deflection and diaphragm pressure sensitivity are important parameters which affect the performance of micro-diaphragm. The findings also indicated that the diaphragm deflection and diaphragm pressure sensitivity are increased when the micro-diaphragm is thin. However, thinner micro-diaphragm has been found to reduce its resonance frequency.

In addition, the silicon-based and polymer-based materials have been found as suitable to be used for the micro-diaphragm. Thus, both types of materials would be used as micro-diaphragm material and their performance would also be analyzed.

The design optimization technique needs to be applied in order to choose appropriate design parameters for the micro-diaphragm. Based on the literature studies, the robust design-based method is more suitable for high quality design as compared to the reliability design-based method. More efficient approach and fewer simulation runs have made the Taguchi Method suitable to be used in optimizing the performance of micro-diaphragm.

CHAPTER 3

METHODOLOGY

3.1 Introduction

This chapter describes the methodology used in the present study. The methodology consists of five stages as shown in Figure 3.1. The study began with the literature review of the design processes of micro-diaphragm. The second stage is continued with the design processes of the micro-diaphragm. In these design processes, the operation and design specification for the micro-diaphragm are specified. In addition, the modelling of the micro-diaphragm is conducted using MEMS Software, known as, *Intellisuite*.

In the third stage, simulations are conducted to analyze the performance of micro-diaphragm. These simulations used finite element analysis to study the micro-diaphragm characteristics which include static, frequency and transient responses of the micro-diaphragm.

Nevertheless there are three design parameters namely diaphragm radius, diaphragm thickness and diaphragm material which have been found to affect the performance of micro-diaphragm. Thus, optimization by Taguchi method was conducted in stage four to ensure the variation in design parameters is minimized and optimum micro-diaphragm performance can be achieved. Finally, the optimum combination of the design parameters for the micro-diaphragm was chosen at stage five as shown in Figure 3.1.

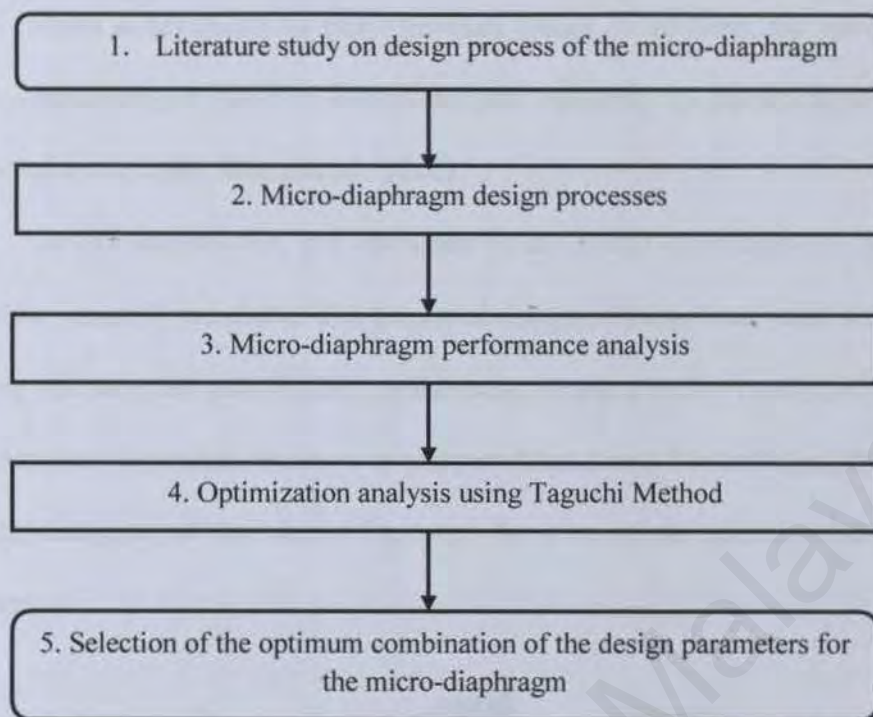


Figure 3.1: Flowchart of the design methodology

Micro-diaphragm design processes and its performance analysis are presented in Sections 3.2 and 3.3 respectively. Finally Section 3.4 explained the optimization analysis using the Taguchi Method.

3.2 Micro-Diaphragm Design Processes

In this section, the operation of the micro-diaphragm and its design specifications are discussed. The modelling process of the micro-diaphragm using the MEMS design software is also presented.

3.2.1 Operation of the micro-diaphragm

The MEMS technology enables the development of miniature sensors. Since the optical MEMS are capable of guiding signals to and from a measurement site, it has

been chosen in designing the pulse pressure sensor. In addition, the optical MEMS offer high adaptability in harsh environment and immunity to electromagnetic interference (Xiao-qi *et al.*, 2006, Wang *et al.*, 2006).

In this sub-section, the operation of the micro-diaphragm for the optical pulse pressure sensor is presented. The proposed design of the optical pulse sensor is shown in Figure 3.2. In more specific, the optical pulse pressure sensor consists of an optical fibre and a micro-diaphragm structure as pressure transducer. Nevertheless, this study focuses on the designing of the micro-diaphragm for a complete optical pulse pressure sensor system.

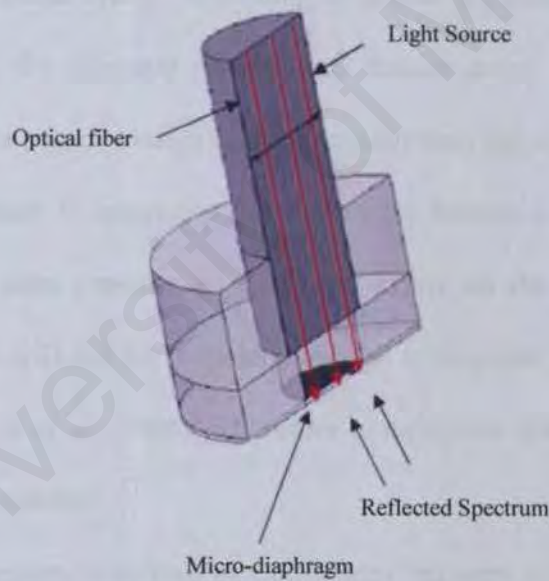


Figure 3.2: Proposed design of the optical pulse pressure sensor

The optical pulse pressure sensor is demodulated by detecting the shift of the reflected or transmitted spectrum from the light source. A light emitting diode (LED) is used as a light source and it will be transmitted through the optical fibre. Pulse pressure

sensed from the surface of radial artery will cause deformation of the micro-diaphragm which will change the reflected or transmitted spectrum.

The diffused components of the reflected light will strike the micro-diaphragm which is in contact with the skin on human's radial artery. Meanwhile the cavity length and diaphragm deflection can be measured from the reflected spectrum. Information about arterial stiffness and elasticity of the artery could also derived from them (Wilkinson *et al.*, 2002).

3.2.2 Micro-diaphragm Design Specifications

The optical pulse pressure sensor is designed to sense the pulse pressure on the surface of human's radial artery. According to (Le *et al.*, 2006, Madssen *et al.*, 2006, Osika *et al.*, 2007), the diameter of a normal human artery is between 2 to 3 mm. Therefore, a complete sensor system must be smaller than the size of radial artery.

Since the sensor is externally attached to the human's wrist, the pulse pressure will not create the same pressure as the blood exerts on the arteries wall (Le *et al.*, 2006). The pressure will not be sufficient enough to displace the micro-diaphragm by more than 1 μm (Le *et al.*, 2006). Therefore a miniature diaphragm with maximum deflection of 1 μm is needed.

The pulse pressure is defined as a difference between systolic and diastolic blood pressure during heart contractions (Benetos *et al.*, 1997). Thus, the micro-diaphragm should be able to operate in the blood pressure measurement in the range from 0 to 300 mmHg.

In order to ensure that the micro-diaphragm operates in a linear range, the resonance frequency of the diaphragm should be at least 2.5 times larger than the applied frequency (Wang *et al.*, 2006). For pulse pressure detection, the micro-

diaphragm should be able to operate in a frequency range of 0 to 50 kHz. The summarized micro-diaphragm design specifications are presented in Table 3.1.

To successfully perform pulse pressure measurement on a human's wrist, the sensor must be miniature in size. In addition, it also needs to have an adequate detection system to measure the small changes in micro-diaphragm deformation. The optical pulse pressure sensor must have an appropriate dynamic range and sensitivity for small pulse pressure measurement. Furthermore, the sensor must be biocompatible to be used in the pulse pressure measurements

Table 3.1: Diaphragm design specifications

Parameter	Value
Pressure range	0-300 mmHg
Frequency range	0-50 kHz
Maximum Deflection	$\leq 1 \mu\text{m}$

3.2.3 Modelling of the micro-diaphragm

Modelling of the micro-diaphragm was conducted using the MEMS Software, *Intellisuite*TM. The micro-diaphragm was designed using the microfabrication process of the MEMS technology in the *Intellifab*TM module.

A three-dimension (3D) micro-diaphragm model was initially designed using the *Intellifab*TM, a fabrication computer aided drawing (CAD) tool from *Intellisuite*TM (Figure 3.3). Steps involved in the fabrication process are listed in Table 3.2. In the UV lithography step, a mask to create a pattern is defined. There are four masks required to create the micro-diaphragm. The first mask is used to pattern the diaphragm material to create an outer surface of the micro-diaphragm. Meanwhile the second and third masks

are used to pattern the diaphragm material to form a cavity wall and diameter hole respectively. The final mask is used to back-etched the substrate layer.

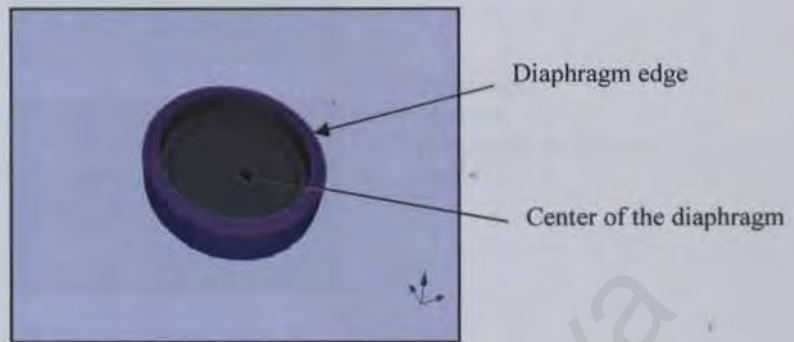


Figure 3.3: 3D micro-diaphragm model

The fabrication process consists of 18 steps and it begins with the deposition of silicon wafer as a substrate material and this is followed by the deposition of silicon dioxide as an electrical isolation. After the silicon wafer is cleaned, a $2\ \mu\text{m}$ release layer of silicon dioxide film is deposited on the silicon wafer by plasma-enhanced chemical vapour deposition (PECVD) using tetraethoxysilane (TEOS).

Then, the second layer of diaphragm material is deposited on the top of the release layer. The second layer of $30\ \mu\text{m}$ thick formed the cylindrical wall around the cavity of the sensor system. Diameter hole and cavity wall are patterned using deep reactive ion etching (DRIE). The diameter hole is smaller than the cavity wall to act as an insertion stop for the optical fibre.

In order to enhance the reflection from the diaphragm, metal was evaporated onto the entire wafer. $200\ \text{\AA}$ of chromium and $1000\ \text{\AA}$ of titanium were coated on the wafer. After developing the micro-diaphragm, micromanipulator will be used to insert cleaved end of a single mode optical fiber. The fabrication process in the *Intellifab* module is listed in Table 3.2 and shown in Figure 3.4.

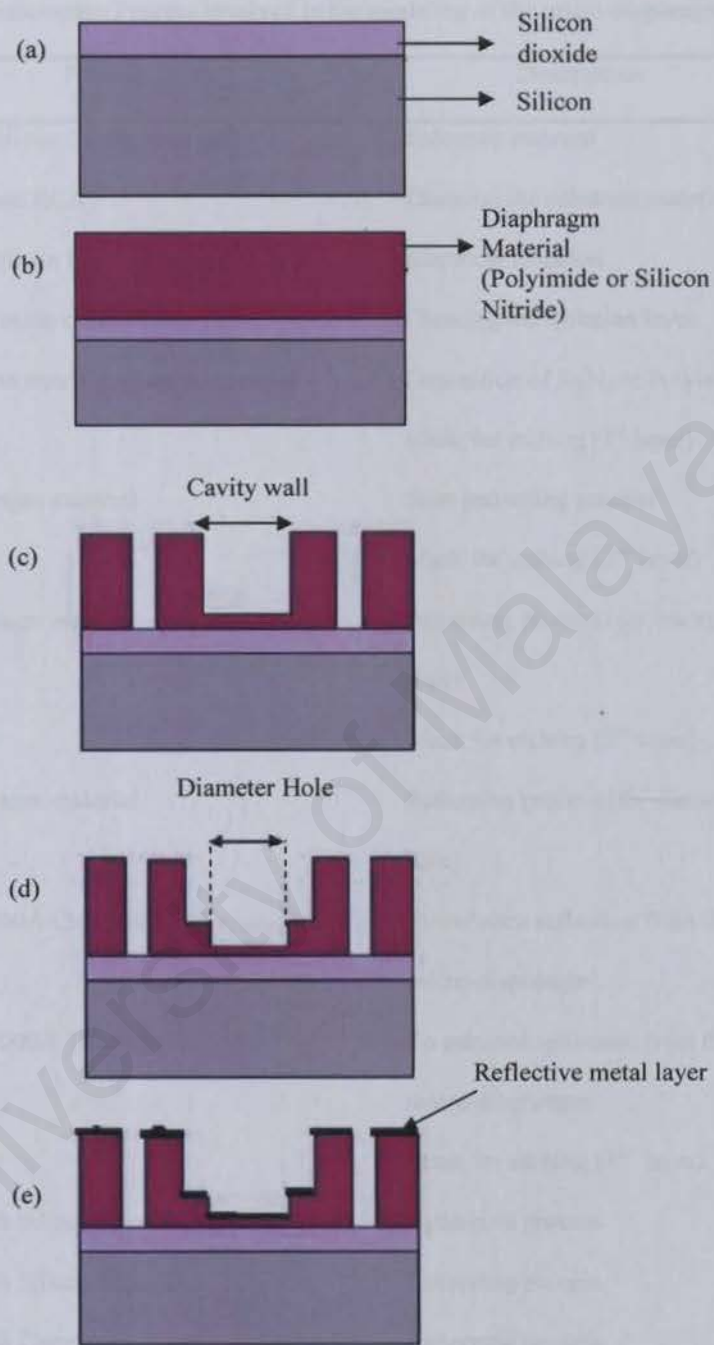


Figure 3.4: Fabrication process for the diaphragm. (a) Release layer ($2\mu\text{m}$ silicon dioxide) is deposited onto the silicon wafer. (b) Diaphragm material is deposited onto the wafer as diaphragm layer. (c) Diameter hole is patterned by using deep reactive ion etching (DRIE). (d) Etching process using DRIE to form cavity walls. (e) 200\AA chromium and 1000\AA Titanium will be evaporated onto the whole wafer as a reflective metal layer.

Table 3.2: Fabrication Process involved in the modeling of the micro-diaphragm

Step	Process	Description	Mask used
1.	Deposition of Silicon Czochralski 100	Substrate material	-
2.	Etch Silicon clean RCA	Cleaning the substrate material	-
3.	Deposition of Silicon Dioxide using PECVD	Electrical isolation	-
4.	Etch Silicon Dioxide clean RCA	Cleaning the isolation layer	-
5.	Deposition of the micro-diaphragm material	Deposition of Si_3N_4 or Polyimide	-
6.	UV lithography	Mask for etching (1 st layer)	Mask 1
7.	DRIE of diaphragm material	Start patterning process	Mask 1
8.	UV lithography	Mask for etching (2 nd layer)	Mask 2
9.	DRIE of diaphragm material	Patterning process (for cavity wall)	Mask 2
10.	UV lithography	Mask for etching (3 rd layer)	Mask 3
11.	DRIE of diaphragm material	Patterning process (for diameter hole)	Mask 3
12.	Deposition of 200Å Chromium	To enhance reflection from the micro-diaphragm	-
13.	Deposition of 1000Å Titanium	To enhance reflection from the micro-diaphragm	-
14.	UV lithography	Mask for etching (4 th layer)	Mask 4
15.	Bottom wet etch Silicon Czochralski 100	Patterning process	Mask 4
16.	Bottom wet etch Silicon Dioxide	Patterning process	Mask 4
17.	Bottom wet etch Chromium	Patterning process	Mask 4
18.	Bottom wet etch Titanium	Patterning process	Mask 4

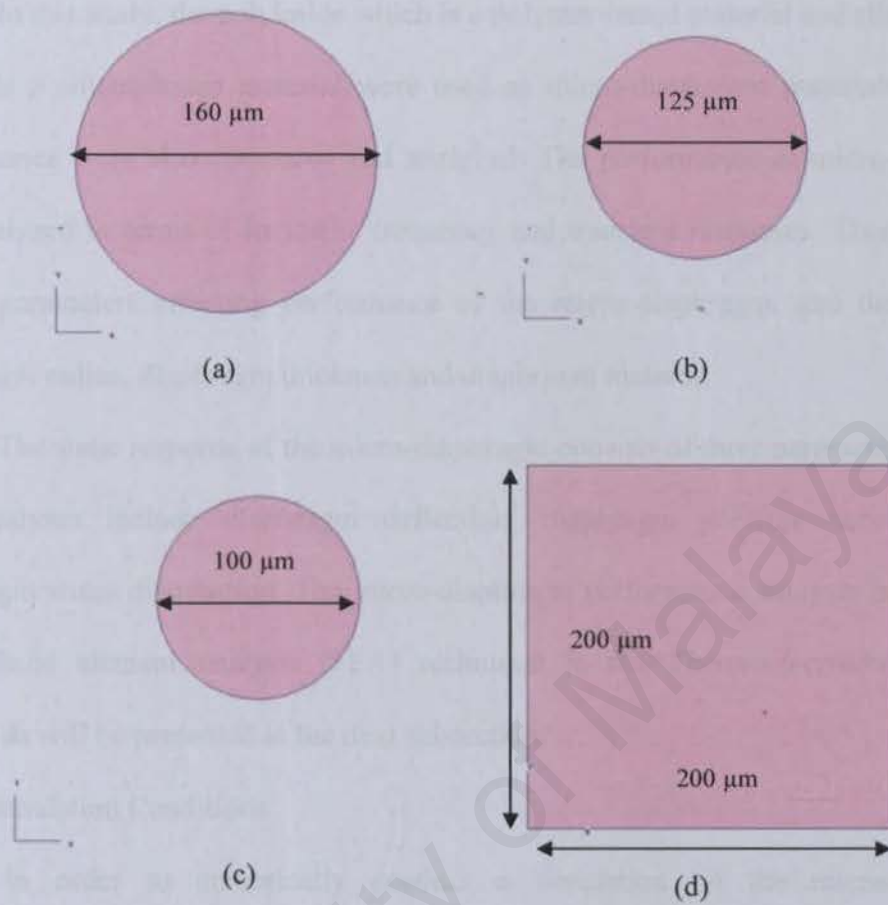


Figure 3.5: Example of the masks for patterning process (a) Mask 1 (b) Mask 2 (c) Mask 3 (d) Mask 4

3.3 Micro-Diaphragm Performance Analysis

When the solid model of the micro-diaphragm was designed in the *Intellifab*TM module, the performance of micro-diaphragm was further analyzed using the *Thermoelectromechanical*TM module. Generally, there are three types of micro-diaphragm namely circular, square and rectangular diaphragms. Due to the negligence of residual stress at the edge of diaphragm surface, the circular shape has been chosen as the micro-diaphragm for the optical pulse pressure sensor (Correia *et al.*, 1998).

In this study, the polyimide which is a polymer-based material and silicon nitride which is a silicon-based material were used as micro-diaphragm materials and their performance were also compared and analyzed. The performance of micro-diaphragm was analyzed in terms of its static, frequency and transient responses. There are three design parameters affecting performance of the micro-diaphragm, and these include diaphragm radius, diaphragm thickness and diaphragm material.

The static response of the micro-diaphragm consists of three parametric analyses. The analyses include diaphragm deflection, diaphragm pressure sensitivity and diaphragm stress distribution. The micro-diaphragm performance analysis is conducted using finite element analysis (FEA) technique in the *Thermoelectromechanical*TM module as will be presented in the next subsection.

3.3.1 Simulation Conditions

In order to numerically conduct a simulation on the micro-diaphragm performance, the 3D model of micro-diaphragm structure must be meshed and discretized into elements. The *Inttelisuite*TM requires 20-node brick element for the finite element analysis. The simulation is conducted using finite element analysis (FEA) in *Thermoelectromechanical*TM module.

The FEA which is also known as the finite element method is a computational technique used to obtain approximate solutions of the boundary condition problems in engineering (Shirazee *et al.*, 1997). Prior to fabricating the micro-diaphragm, it is essential to perform a simulation analysis using the FEA. This analysis is helpful because the FEA gives close approximation to the actual prototype before it is fabricated.

Enormous amount of time and money can be saved with the use of the FEA. This is because difficulties encountered during designing stage of the micro-diaphragm can be detected and rectified at an early stage. Hence, trial and error approaches which are still conducted today can be avoided (Shirazee *et al.*, 1997). In addition, the FEA is a simulation technique which is well suited for analysis of the performance of the MEMS devices (Goldberg *et al.*, 1997).

The type of design elements, mesh profile, material properties, boundary conditions and loads are defined prior to the starting of the FEA simulations. The movable micro-diaphragm in the FEA simulation needs to be able to operate in a small deflection region and must have a perfect boundary condition.

Boundaries of the micro-diaphragm are fixed and clamped at its edge as shown in Figure 3.6 . The 3-dimensional (3D) model of the micro-diaphragm in Figure 3.6 is meshed and discretized into elements for the FEA simulation in the *Thermoelectromechanical*TM module. Figure 3.7 shows the 3D model of the micro-diaphragm before and after meshed.

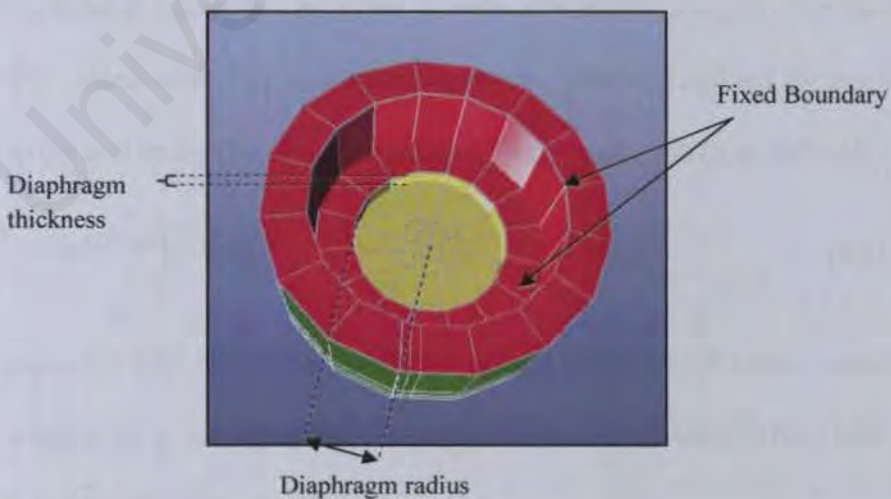


Figure 3.6: Micro-diaphragm with fixed boundary

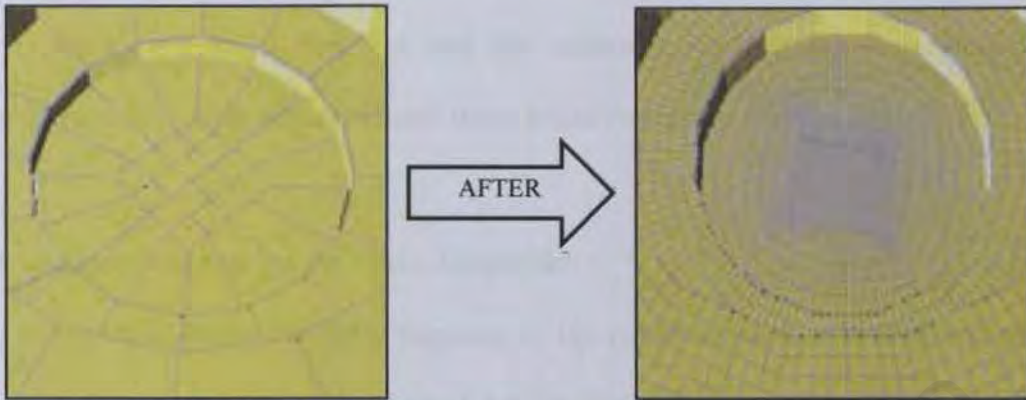


Figure 3.7: 3D micro-diaphragm model before and after meshed

The micro-diaphragm model is discretized into several or many elements (meshed), which each of the elements possesses behaviour which varies to external and internal load. These elements are then recombined at the nodes into a global model. The process results in a set of simultaneous algebraic equations. The basic equations for the standard displacement-based finite element analysis are presented in equation:

$$\int_V \sigma : \delta D dV = \int_S t^i \cdot \delta v dS + \int_V f^T \cdot \delta v dV \quad (3.1)$$

The left-hand side of this equation is replaced with the integral over the reference volume of the virtual work rate per reference volume which is defined by any conjugate pairing of stress and strain (Intellisuite Technical Reference, 2007), as follows:

$$\int_{V^0} \tau^C : \delta \alpha dV^0 = \int_S t^T \cdot \delta v dS + \int_V f^T \cdot \delta v dV \quad (3.2)$$

where τ^c and ϵ are any conjugate pairing of material stress and strain measures. The particular choice of ϵ is dependent on the individual element. The finite element interpolator can be written generally as:

$$u = N_N u^N \quad (3.3)$$

where N_N are interpolation functions which are dependent on some material coordinate system, u^N are nodal variables and the summation convention is adopted for the uppercase subscripts which indicate these nodal variables.

3.3.2 Static Response of the Micro-Diaphragm

In this study, the static response of the micro-diaphragm is analyzed using the load-deflection method. This is a well known method for the measurement of thin films with elastic properties (Wang *et al.*, 2006, Eaton *et al.*, 1999). A side view of a circular diaphragm loaded with applied pressure is shown in Figure 3.8. This diaphragm is loaded with lateral uniform pressure, P and thus, the diaphragm deforms as a function of the applied pressure.

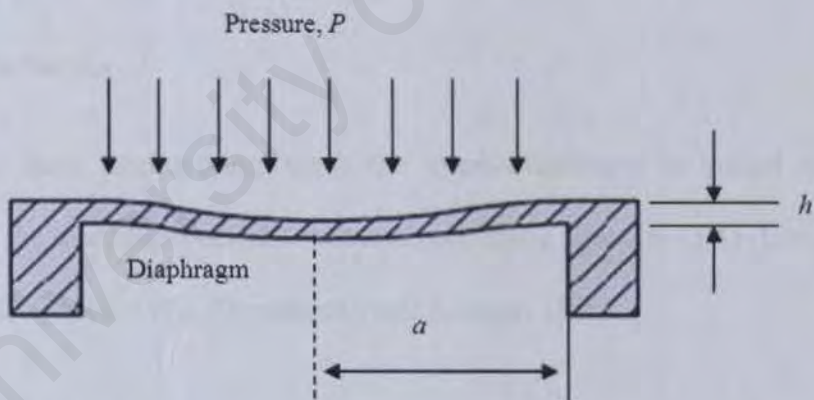


Figure 3.8: Structure model for the circular diaphragm

When the circular diaphragm which is rigidly clamped at its edge is applied with the lateral pressure, it tends to bend into a “quasispherical” shape. In this study, the following assumptions were made to study the diaphragm deflection and diaphragm pressure sensitivity:

- a) The circular micro-diaphragm is flat and has uniform thickness
- b) Diaphragm material is isotropic and homogeneous
- c) Maximum deflection of the micro-diaphragm is less than 30% of diaphragm thickness
- d) All forces, loads and reactions are applied normally to the micro-diaphragm (lateral)
- e) The micro-diaphragm is not stressed beyond its elastic limit
- f) The diaphragm thickness should not be too thick (less than 20% of the diaphragm diameter)
- g) The micro-diaphragm will deflect mostly due to the bending tensile forces on the micro-diaphragm.

(i) Diaphragm Deflection

Based on these assumptions, when the micro-diaphragm is loaded with the applied pressure, the diaphragm deflection is analyzed using equation (3.4) (Eaton *et al.*, 1999, Xu, 2005, Giovanni, 1982, Timoshenko and Kreiger, 1959):

$$y = \frac{3(1-\mu^2)P}{16Eh^3} (a^2 - r^2)^2 \quad (3.4)$$

where P is the applied pressure, y is deflection, μ is Poisson's ratio, E is Young's Modulus, h is diaphragm thickness, a and r are diaphragm radius and radial distance respectively. This equation shows that the diaphragm deflection is a function of the pressure difference and the radial distance of the diaphragm.

Since the micro-diaphragm is designed in circular shape, the diaphragm deflection varies from its edges ($r=a$) to the maximum value at its centre ($r=0$). The maximum diaphragm deflection, y_c at the centre of the diaphragm was analyzed using the following equation (Giovanni, 1982):

$$y_c = \frac{3(1-\mu^2)Pa^4}{16Eh^3} \quad (3.5)$$

By rearranging equation (3.4), the diaphragm deflection curve under the applied pressure could be represented as in equation (3.6) (Xu, 2005):

$$y = \frac{3(1-\mu^2)P}{16Eh^3} a^4 \left[1 - \left(\frac{r}{a} \right)^2 \right]^2 = y_c \left[1 - \left(\frac{r}{a} \right)^2 \right]^2 \quad (3.6)$$

The equations presented above are applied in the micro-diaphragm analysis if the diaphragm deflection is less than 30% of the diaphragm thickness (Giovanni, 1982). Some previous studies (Xu, 2005, Deng, 2004) have shown that the diaphragm radius is generally determined by the measurement requirements such as measuring space and sensor packaging.

Consequently, when the diaphragm radius is selected, and the pressure measurement range is known, and the minimum diaphragm thickness required for the micro-diaphragm could be estimated using the following equation (Xu, 2005, Deng, 2004):

$$h_{\min} = a \left[\frac{5(1-\mu^2)P_{\max}}{8E} \right]^{1/4} \quad (3.7)$$

Therefore this equation plays a major role in determining suitable thickness for diaphragm. The selection of an appropriate diaphragm thickness will ease the design process of high sensitivity diaphragm.

(ii) Diaphragm Pressure Sensitivity

Despite diaphragm deflection, the sensitivity of the micro-diaphragm is another important parameter which needs to be considered. The diaphragm pressure sensitivity is a ratio of the changes in the diaphragm deflection to pressure difference. The diaphragm pressure sensitivity is studied using equation (3.8) (Xu, 2005, Deng, 2004, Giovanni, 1982):

$$S = \frac{\Delta y}{\Delta P} \quad (3.8)$$

Based on this equation, it is shown that diaphragm deflection is closely related to diaphragm pressure sensitivity. In more specific, the higher the diaphragm deflection increases the diaphragm pressure sensitivity.

In designing the micro-diaphragm, it should be one which sensitive to the small changes of pulse pressure. Thus, micro diaphragm with high deflection and sensitivity needs to be constructed as a pressure transducer for the optical pulse pressure sensor.

(iii) Diaphragm Stress Distribution

Analysis of diaphragm stress distribution is conducted to predict any failure of the diaphragm. For small diaphragm deflection, there is no stress in the middle plane of the micro-diaphragm. However, the bending stresses increase linearly to the outer surfaces of the micro-diaphragm.

As discussed in the previous section, the stress analysis must include the radial and tangential stresses since the micro-diaphragm is bent into “quasispherical” shape. Both stresses vary along the diaphragm radius. The radial stress σ_r at any distance r from the centre is calculated using the equation (3.9) (Giovanni, 1982):

$$\sigma_r = \pm \frac{3Pa^2}{8h^2} \left[(3+\mu) \frac{r^2}{a^2} - (1+\mu) \right] \quad (3.9)$$

The tangential stress σ_t at any radial distance r is given by equation (3.10) (Giovanni, 1982):

$$\sigma_t = \pm \frac{3Pa^2}{8h^2} \left[(3\mu+1) \frac{r^2}{a^2} - (1+\mu) \right] \quad (3.10)$$

where P is the applied pressure, μ is Poisson’s ratio, h is diaphragm thickness, a and r are diaphragm radius and radial distance respectively.

The micro-diaphragm experienced the maximum radial and tangential stresses at the edge and centre of the micro-diaphragm respectively. Therefore the maximum radial stress in equation (3.11) and the maximum tangential stress in equation (3.12) are employed (Xu, 2005, Deng, 2004, Giovanni, 1982):

$$\sigma_{r,\max} = \pm \frac{3}{4} P \frac{r^2}{h^2} \quad (3.11)$$

$$\sigma_{t,\max} = \pm \frac{3}{8} (1 + \mu) P \frac{r^2}{h^2} \quad (3.12)$$

In addition, the diaphragm stress distribution is correlated with the diaphragm deflection. This relationship was investigated using equation (3.14) to (3.17). By rearranging equation (3.5) and solving (Xu, 2005, Deng, 2004, Giovanni, 1982), the following is retrieved:

$$P = \frac{16}{3(1-\mu^2)} \frac{Eh^3 y_c}{a^4} \quad (3.13)$$

Equation (3.13) is then introduced in the equation (3.9) for the radial stress leading to (Xu, 2005, Deng, 2004, Giovanni, 1982):

$$\sigma_r = \pm \frac{2Ehy_c}{(1-\mu^2)a^2} \left[(3+\mu)\frac{r^2}{a^2} - (1+\mu) \right] \quad (3.14)$$

Therefore, at the edge of the diaphragm, the maximum radial stress, $\sigma_{r,max}$ can be referred to as follows (Xu, 2005, Deng, 2004, Giovanni, 1982):

$$\sigma_{r,max} = \frac{4}{1-\mu^2} \frac{Ey_c h}{a^2} \quad (3.15)$$

Using the same concept, a similar expression for the tangential stress σ_t is obtained (Xu, 2005, Deng, 2004, Giovanni, 1982):

$$\sigma_t = \pm \frac{2Ehy_c}{(1-\mu^2)a^2} \left[(3\mu+1)\frac{r^2}{a^2} - (1+\mu) \right] \quad (3.16)$$

Thus, the relationship between the maximum tangential stress and deflection is given by the following equation (Giovanni, 1982):

$$\sigma_t = \pm \frac{2Ehy_c}{(1-\mu)a^2} \quad (3.17)$$

where E is Young's Modulus, μ is Poisson's ratio, h is diaphragm thickness, whereas y_c and a are the maximum deflection and diaphragm radius respectively.

3.3.3 Frequency Response of the Micro-Diaphragm

Resonance frequency needs to be taken into consideration when designing the micro-diaphragm for a dynamic pulse pressure measurement (Wang *et al.*, 2006).

Therefore it is important to characterize the relationships between the diaphragm dimension, sensitivity and resonance frequency to design the micro-diaphragm.

In the frequency response of the micro-diaphragm analysis, the diaphragm vibration theory is employed. The micro-diaphragm is assumed to be perfectly elastic and is made of homogeneous isotropic material. The transverse deflection of a circular diaphragm clamped at its edge is expressed in Hemholtz equation (Meirovitch *et al.*, 1997, Timoshenko, 1974).

The solutions of the Hemholtz equation consist of symmetric modes and asymmetric modes as shown in Figure 3.9. These symmetric modes only have nodal circles, but the asymmetric modes have both nodal circles and diameters. In this study, the resonance frequency of the diaphragm was analyzed using the following equation (3.18) (Giovanni, 1982, Xu, 2005):

$$f_{mn} = \frac{\alpha_{mn}}{4\pi} \sqrt{\frac{E}{3\rho(1-\mu^2)}} \left(\frac{h}{r^2}\right) \quad (3.18)$$

where α_{mn} is a constant related to the vibrating modes of the diaphragm, h is the thickness of the diaphragm, r is the effective diaphragm radius, ρ is the mass density of the diaphragm material, whereas μ , and E are Poisson's ratio and Young's modulus of the diaphragm material respectively.

In this case, α indicates the radius of the boundary which may be obtained by taking into account the number of the nodal circles m and the number of the nodal diameters n . Table 3.3 shows the value of the constant α_{mn} . The number of the nodal circles, m and the number of the nodal diameters, n are presented in Figure 3.10.

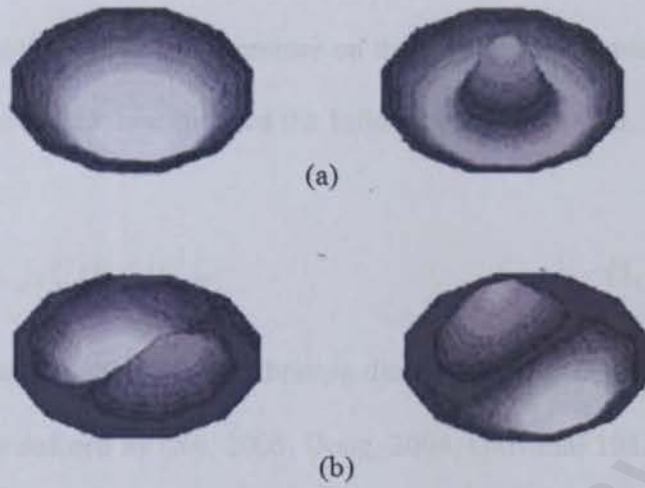


Figure 3.9: Vibration modes: (a) Symmetrical vibration modes (b) Asymmetrical vibration modes (reproduce from Hong *et al.*, 2006)

Table 3.3: Values of constant α_{mn} (reproduced from (Giovanni, 1982, Xu, 2005):

α_{mn}	$n=0$	$n=1$	$n=2$
$m=0$	10.21	21.22	34.48
$m=1$	39.78	60.82	84.58
$m=2$	88.90	120.12	153.76

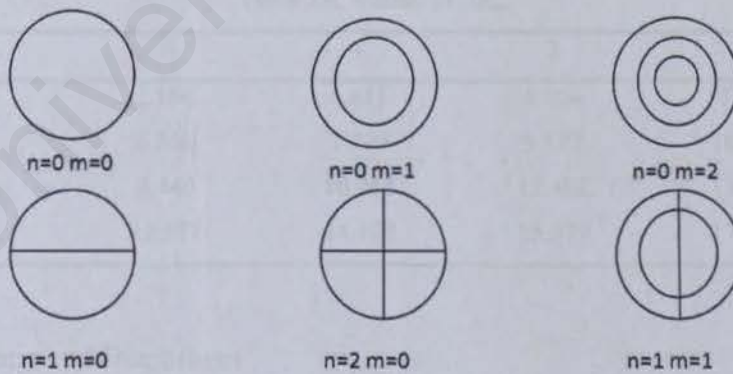


Figure 3.10: Nodal circles and nodal diameters

The micro-diaphragm vibration was analyzed in terms of free diaphragm vibration and force diaphragm vibration analyses.

(i) Free diaphragm vibration

By assuming that there is no pressure on the surface of the micro-diaphragm, the equation of motion of free vibration used the following equation (Xu, 2005, Deng, 2004, Timoshenko, 1974):

$$D\nabla^2 u(r, \theta, t) + \rho h \frac{\partial^2 u(r, \theta, t)}{\partial t^2} = 0 \quad (3.19)$$

where $u(r, \theta, t)$ is the deflection of the vibrating diaphragm, and D is the flexural rigidity of the diaphragm as defined by (Xu, 2005, Deng, 2004, Giovanni 1982):

$$D = \frac{Eh^3}{12(1-\mu^2)} \quad (3.20)$$

Resonance frequency was retrieved from equation (3.19) as in the following (Giovanni, 1982, Xu, 2005):

$$\omega_{mn} = \frac{(\lambda a_{mn})}{r^2} \sqrt{\frac{D}{\rho h}} \quad (3.21)$$

The roots of the equation, λa_{mn} is shown in Table 3.4 :

Table 3.4: Values of λa_{mn}

$m \setminus n$	0	1	2	3
0	3.196	4.611	5.906	7.143
1	6.306	7.799	9.197	10.537
2	9.440	10.958	12.402	13.795
3	12.577	14.108	15.579	17.005

(ii) Force Vibration of Diaphragm

By considering the fact that the micro-diaphragm is applied with a load varying harmonically with time, the equation of motion is given by (Xu, 2005, Deng, 2004):

$$D\nabla^2 u + \rho h \frac{\partial^2 u}{\partial t^2} + v \frac{\partial u}{\partial t} = p e^{iqt} \quad (3.22)$$

in which ν is the coefficient corresponding to the damping of liquid, q is the frequency of varying pressure and p is the amplitude of varying pressure.

While the maximum deflection of the micro-diaphragm occurs when frequency is 0 (static case), the vibration response at the centre of the micro-diaphragm is derived using the following (Xu, 2005, Deng, 2004):

$$u_{mn}(q) = u_{\max} \cdot \beta_{mn}(q) = \frac{3p(1-\mu^2)}{16Eh^3} a^4 \frac{\omega_{mn}^2}{\sqrt{(\omega_{mn}^2 - q^2)^2 + 4q^2 n^2}} \quad (3.23)$$

where

$$\beta = \frac{\Sigma \text{ force}}{\Sigma \text{ no-force}} = \frac{\omega_{mn}^2}{\sqrt{(\omega_{mn}^2 - q^2)^2 + 4q^2 n^2}} \quad (3.24)$$

3.3.4 Transient response of the micro-diaphragm

When the micro-diaphragm dimension is specified, the transient response analysis is conducted for the polyimide and silicon nitride micro-diaphragms. The transient analysis is conducted when the micro-diaphragm is loaded with time-varying load. The relationship between diaphragm deflection and time was investigated. The vibration of the micro-diaphragm is dependent on its material and micro-diaphragm stiffness.

Consequently, the performance of the micro-diaphragm was analyzed in terms of its static, frequency and transient responses. The three design parameters namely diaphragm radius, diaphragm thickness and diaphragm material were found to affect the performance of the micro-diaphragm. In this study, a comparison between the two diaphragm materials (polyimide and silicon nitride) is conducted.

Silicon nitride was chosen because it is transparent in optical range (Correia *et al.*, 1998) and possesses high wear resistance and low friction coefficient (Silva *et al.*, 2008). However polyimide is a high performance polymer material which has a good thermal stability. In addition, it has low linear coefficient of thermal expansion (Cui *et al.*, 2006). Both the materials have excellent properties in designing the micro-diaphragm.

The size of the diaphragm or diaphragm radius are generally determined by the measurement requirements such as installation spaces provided to accurately detect the signals. Since the proposed optical sensor will be placed on the human radial artery to detect the pulse pressure, the complete sensor system must be smaller than the size of the artery. Therefore, with these arrangements, the proposed sensor will provide an adequate detection scheme to measure the changes in diaphragm deformation of the sensor.

As discussed in the earlier section, the radius of the normal human radial artery is in the range of 2.5 mm to 3 mm. Therefore, the diaphragm radius also varies in range of 0 to 500 μm (0.5 mm) so as to achieve allowable maximum deflection of 1 μm .

When the range of diaphragm radius is identified, the minimum required diaphragm thickness is calculated from equation (3.7). Therefore, by replacing the radius, a with maximum diaphragm radius of 500 μm , maximum applied pressure of 0.04 MPa (300 mmHg), the minimum required diaphragm thicknesses for polyimide and silicon diaphragms are given by:

$$h_{\min, \text{polyimide}} = 500 \mu \left[\frac{5(1 - 0.35^2)(0.04 \text{ MPa})}{8 \times 7.5 \text{ GPa}} \right]^{-1/4} \quad (3.25)$$

$$h_{\min, \text{polyimide}} = 20 \mu\text{m}$$

$$h_{\min, \text{siliconnitride}} = 500 \mu \left[\frac{5(1 - 0.27^2)(0.04 \text{ MPa})}{8 \times 270 \text{ GPa}} \right]^{1/4} \quad (3.26)$$

$$h_{\min, \text{siliconnitride}} = 9 \mu \text{m}$$

Therefore, the minimum required diaphragm thickness for both the diaphragms could be identified using these equations. The minimum required diaphragm thickness for Polyimide and Silicon Nitride diaphragms is 20 μm and 9 μm respectively. Therefore in order to investigate the micro-diaphragm performance, diaphragm thickness was varied in a range from 0 to 20 μm . Design parameters and material properties of polyimide and silicon nitride are presented in Table 3.5.

Table 3.5: Design Parameters and Material Properties of Polyimide and Silicon Nitride Diaphragms

Design Parameters	Variation Range
Diaphragm radius range (μm)	0-500
Diaphragm thickness range (μm)	0-20
Diaphragm material	Polyimide and Silicon Nitride

Thus, the analysis of the micro-diaphragm performance was conducted using these ranges of the design parameter.

3.4 Optimization Technique in Designing the Micro-Diaphragm

The Taguchi method involves three stages (Syracos, 2003, Taguchi, 1989, Bendell, 1988), which are system design, parameter design, and tolerance design. In the system design stage, the design specifications for the micro-diaphragm are determined.

The second stage of Taguchi method is the parameter design stage. In this stage, the specific values of the design parameters also known as control factors are

determined. Therefore, it will minimize variability transmitted from uncontrollable (or noise) variables. Selection of proper orthogonal array and appropriate performance characteristics for the micro-diaphragm are also conducted in this stage. Meanwhile, the simulation trials were conducted when the control factors and levels were specified.

The best tolerances for the parameters are specified in the tolerance design stage. The three stages in the Taguchi Method are presented in Figure 3.11. Moreover, two major tools in the robust design are presented in Figure 3.12 (Taguchi, 1989, Bendell, 1988, Ghani *et al.*, 2004).

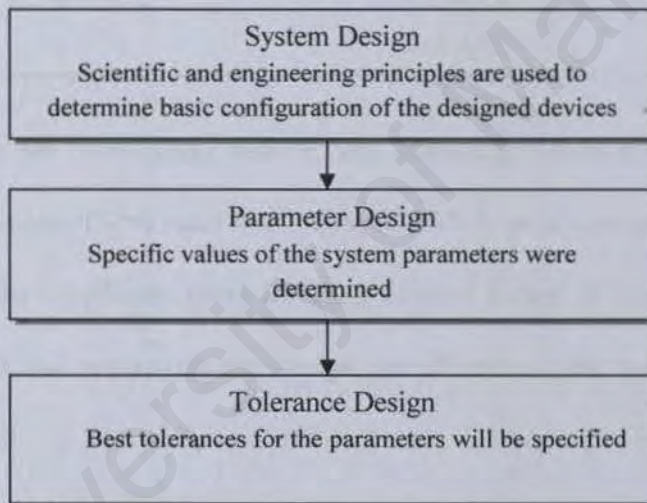


Figure 3.11: Three stages in Taguchi Method

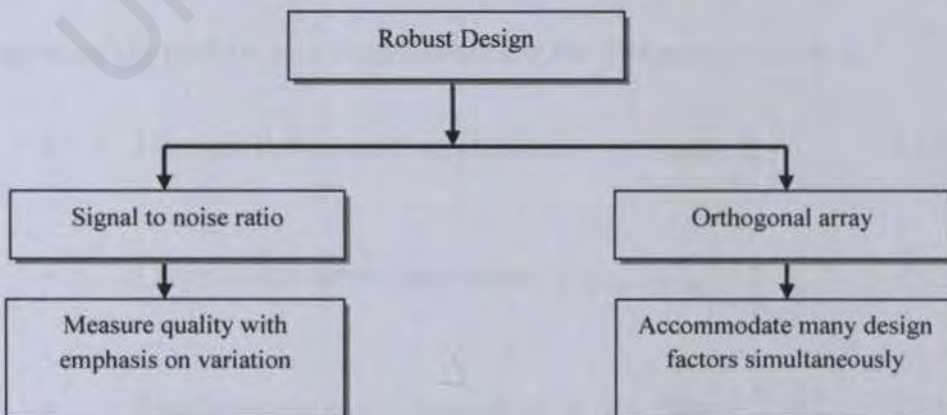


Figure 3.12: Two major tools in robust design

The Taguchi Method is performed using an iterative procedure to obtain the optimum design parameters for the diaphragm as shown in Figure 3.13. The optimization procedure starts with problem initialization. It includes selection of a proper orthogonal array and appropriate performance characteristics in the analysis of the S/N ratio. The following standard orthogonal arrays are commonly used in design experiments (Table 3.6):

Table 3.6: Commonly used orthogonal array (Basem *et al.*, 2005)

Level	Orthogonal Array
2	L4, L8, L12, L16, L32, L64
3	L9, L18, L27
4	L16, L32

Based on the simulation results, the statistical optimization analyses which include signal-to-noise (S/N) ratio and Pareto ANOVA were conducted. These analyses will determine the significant level for each control factor. If the determined control factors and levels did not satisfy the design specifications, the optimization procedure would be repeated.

3.4.1 S/N Ratio

The performance of the micro-diaphragm can be optimized using three the categories of the performance characteristics in the S/N ratio as follows:

- Nominal is the best characteristic: $S/N = 10 \log \left(\frac{\bar{y}}{s\bar{y}} \right)$ (3.27)

- Larger-is-the better (maximize): $S/N = -10 \log \left(\frac{1}{n} \sum_{i=1}^n \frac{1}{y_i^2} \right)$ (3.28)

- Smaller-is-the better (minimize): $S/N = -10 \log \left(\frac{1}{n} \sum_{i=1}^n y_i^2 \right)$ (3.29)

where \bar{y} , is the average of the observe data, s_y^2 is the variance of y , n is the number of observations, and y is the observed data.

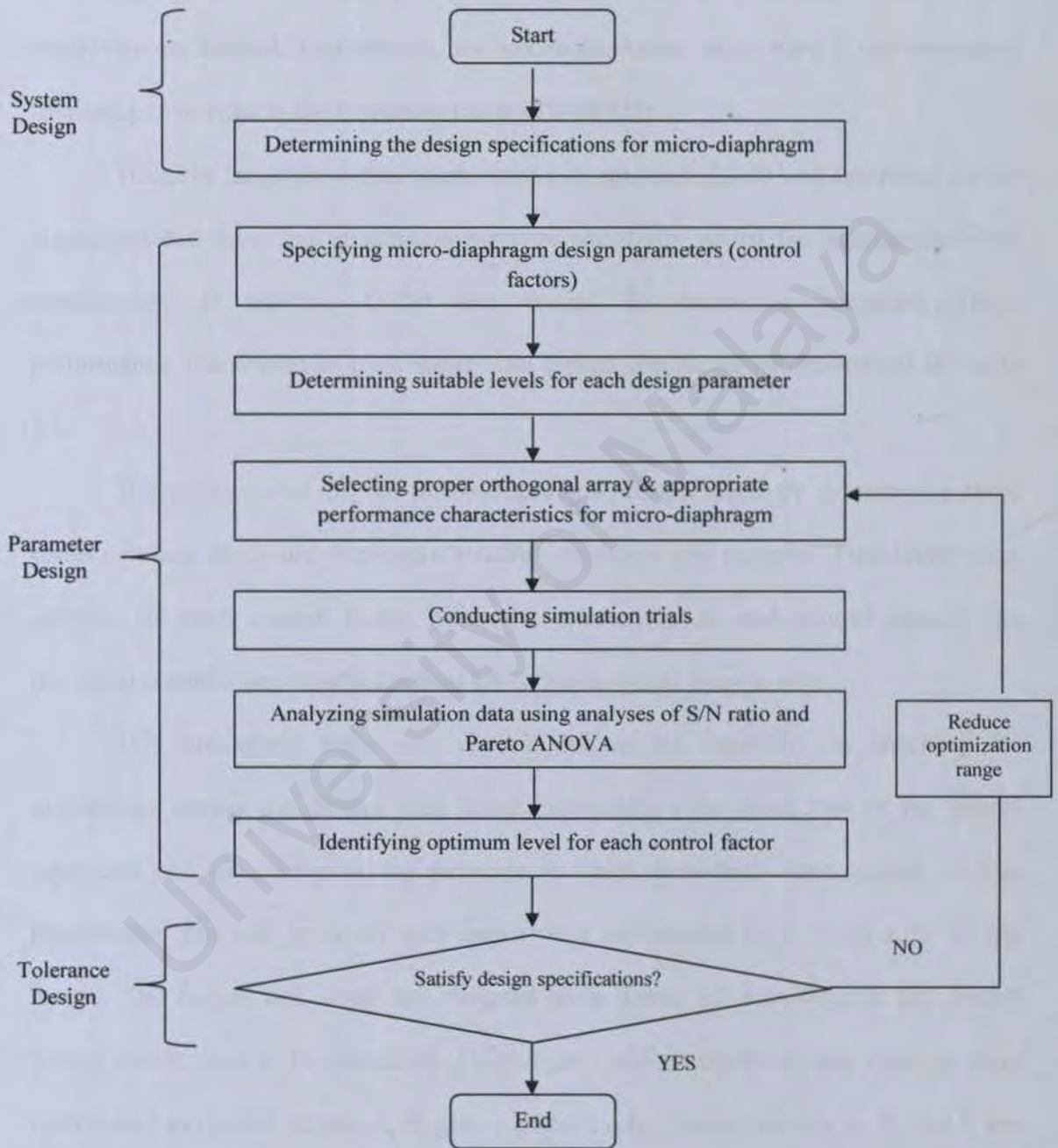


Figure 3.13: Flowchart of Taguchi Method used in designing the micro-diaphragm

In this study, there are three performance characteristics need to be optimized which are diaphragm's deflection, sensitivity and resonance frequency. Hence, in designing the micro-diaphragm, high diaphragm deflection and high diaphragm pressure sensitivity are needed. Furthermore, the micro-diaphragm must have a low resonance frequency to operate in the frequency range of 0-50 kHz.

Thus, the larger-the-better characteristic in equation (3.2.8) was employed for the diaphragm deflection and diaphragm pressure sensitivity whilst the smaller-the-better characteristic in equation (3.29) was applied for resonance frequency. These performance characteristics must satisfy the design specifications determined in Table 3.1.

The performance of the micro-diaphragm is optimized by considering three control factors which are diaphragm's radius, thickness and material. Two levels were selected for each control factor. With the selected levels and control factors, the fractional factorial design of a standard L8 (2^3) orthogonal array is used.

This orthogonal array was chosen due to its capability in checking for interactions among the factors with fewer experiment runs. Each row of the matrix represents one trial. However, the sequence in which these trials were carried out was randomized. The two levels of each factor were represented by a '1' or a '2' in the matrix. The factors and levels are assigned as in Table 3.7 according to the control factors which need to be optimized. Diaphragm's radius, thickness and material were represented as control factors A, B, and C respectively. Control factors A, B, and C are arranged in columns 4, 2 and 1 respectively in the standard L8 (2^3) orthogonal array as shown in Table 3.8.

Table 3.7: Control factors and levels in the diaphragm design

Control Factor	Level	
	1	2
Diaphragm Radius (μm)	50	90
Diaphragm Thickness (μm)	4	8
Diaphragm Material	Polyimide	Silicon Nitride

Table 3.8: Basic Taguchi L8 (2^3) orthogonal array

Run	Columns						
	1	2	3	4	5	6	7
1	1	1	1	1	1	1	1
2	1	1	1	2	2	2	2
3	1	2	2	1	1	2	2
4	1	2	2	2	2	1	1
5	2	1	2	1	2	1	2
6	2	1	2	2	1	2	1
7	2	2	1	1	2	2	1
8	2	2	1	2	1	1	2
	C	B	-BC	A	-AC	-AB	ABC

Eight simulation trials were conducted based on the combination of control factors presented in L8 (2^3) orthogonal array. From these simulation trials, the S/N ratios for three performance characteristics were calculated. These calculated results were used to build a response table by averaging the S/N ratios of the same level for each control factor. Since the simulation trial was arranged in orthogonal array, it was possible to separate the effect of each control factors at different levels. For example, the mean S/N ratio for the diaphragm radius at level 1 was calculated by averaging the S/N ratios for the simulation trials 1, 3, 5 and 7.

Once the response table was obtained, the optimum level for each control factor is identified by finding the largest S/N ratio in the corresponding column of the response table. If the results of the optimum combination did not satisfy the design specification, the optimization process in parameter design stage would be repeated.

Meanwhile, the significant interaction between control factors was further analyzed using a two-way table (Ghani *et al.*, 2004). This analysis is conducted by taking a summation for each interaction at each level (Ghani *et al.*, 2004). The calculation formula to construct a two-way table is tabulated in Appendix C. The optimum level for the interaction is indicated by the highest value in that particular two-way table.

3.4.2 Pareto Analysis of Variance (ANOVA)

The optimization is continued with the analysis of variance (ANOVA). The Pareto ANOVA analysis is conducted by separating the total variability of the S/N ratios.

The Pareto ANOVA is measured by sum of square deviations from the total mean of the S/N ratio. The total sum of the squared deviations can be calculated using equation (3.30) (Nalbant *et al.*, 2007) as follows:

$$SS_T = \sum_{i=1}^m \eta_i^2 - \frac{1}{m} \left[\sum_{i=1}^m \eta_i \right]^2 \quad (3.30)$$

Due to each process parameter, the sum of the squared deviations is presented in equation (3.31) (Nalbant *et al.*, 2007):

$$SS_p = \sum_{j=1}^t \frac{(s\eta_j)^2}{t} - \frac{1}{m} \left[\sum_{i=1}^m \eta_i \right]^2 \quad (3.31)$$

where m is the number of experiments in the orthogonal array, η_i is the mean S/N ratio for the i th experiment. p represent one of the experiment parameters, j is the level number of the parameter p , t is the repetition of each level of the parameter p , and $\sum \eta_{jt}$ is the sum of S/N ratio involving this parameter p and level j . Thus, the percentage contribution ρ can be calculated as (Nalbant *et al.*, 2007):

$$\rho = \frac{SS_p}{SS_T} (\%) \quad (3.32)$$

The Pareto ANOVA analyses for all performance characteristics were calculated from the formula shown in Table 3.9. The highest value of sum of the squared deviations indicates the optimum level for each control factor. Meanwhile, control factor with the highest contribution ratio represents which particular control factor greatly affect the micro-diaphragm performance. The Pareto diagram for the three micro-diaphragm performance will be plotted based on this calculated contribution ratio.

Table 3.9: Pareto ANOVA for two level factors

Factor	A	B	C	Total
Sum at factor level				
1	$\sum A1$	$\sum B1$	$\sum C1$	T
2	$\sum A2$	$\sum B2$	$\sum C2$	
Sum of squares of differences	S_A	S_B	S_C	S_T
Contribution ratio (%)	S_A / S_T	S_B / S_T	S_C / S_T	100

Total sum at factor level, $T = \sum A1 + \sum A2$

Sum of squares of difference for control factor A, $S_A = (\sum A1 - \sum A2)^2$

Sum of squares of difference for control factor B, $S_B = (\sum B1 - \sum B2)^2$

Sum of squares of difference for control factor C, $S_C = (\sum C1 - \sum C2)^2$

Total of Sum of squares of difference, $S_T = S_A + S_B + S_C$

Hence, based on analyses of S/N ratio and Pareto ANOVA, the optimum levels for each control factor could be attained. In order to achieve adequate deflection and sensitivity, the larger-the-better characteristic was employed for the diaphragm deflection and diaphragm pressure sensitivity. Meanwhile, the smaller-the-better characteristic was applied to obtain low vibration frequency of the diaphragm.

This chapter presents the simulation results and analysis to investigate the micro-diaphragms for the typical micro-diaphragm system. The simulation analysis and analysis are divided into two parts namely micro-diaphragm performance and micro-diaphragm analysis using the Taguchi method.

Section 4.2 illustrates an experimental simulation of the micro-diaphragm performance for polyimide, polyimide-copper, and polyimide-copper-gold based materials. The analysis of micro-diaphragm performance includes the deflection and pressure sensitivity.

In this study, the micro-diaphragm was designed in terms of deflection, pressure sensitivity and vibration frequency. Meanwhile, the statistical analysis of Taguchi method is discussed in section 4.3. This section consists of two parts, the Analytic Hierarchy Process (AHP) and Pareto ANOVA analysis of the Pareto ANOVA. Finally, the simulation results and analysis are included in section 4.4.

4.1 Micro-Diaphragm Performance Response

In this section, the simulation of micro-diaphragm performance analysis will be discussed. The simulation results and analysis are presented in sub-sections 4.2.1 and 4.2.2 respectively.

CHAPTER 4

RESULTS AND ANALYSIS

4.1 Introduction

This chapter presents the simulation results and analysis in designing the micro-diaphragm for the optical pulse pressure sensor. The simulation results and analysis are divided into two parts namely micro-diaphragm performance and optimization analyses using the Taguchi method.

Section 4.2 elaborates on the simulation results on the micro-diaphragm performance for polyimide (polymer-based material) and silicon nitride (silicon-based material). The analysis of micro-diaphragm performance includes static, frequency and transient responses.

In the static response, the performance of the micro-diaphragm was discussed in terms of diaphragm's deflection, pressure sensitivity and stress distribution. Meanwhile, the statistical analysis of Taguchi Method is discussed in Section 4.3. This section consists of two parts which are Analysis Signal-to-Noise (S/N) Ratio and Pareto Analysis of Variance (Pareto ANOVA). Finally, the simulation results and analysis are concluded in Section 4.4.

4.2 Micro-Diaphragm Performance Response

In this section, analysis of micro-diaphragm performance which includes static, frequency and transient responses are presented in sub-sections 4.21, 4.22 and 4.23 respectively.

4.2.1 Static Response Analysis

The analysis of static response is divided into three which are diaphragm's deflection, sensitivity and stress distribution.

(i) Diaphragm Deflection

Figures 4.1 (a) to (c) show an example of deflection distribution from top, bottom and side views respectively. The highest and lowest diaphragm deflections are indicated by dark blue and red respectively. It can be seen from the figure that the micro-diaphragm deflected from the outer surface and achieved its maximum deflection of $0.9 \mu\text{m}$ at the centre of the micro-diaphragm.

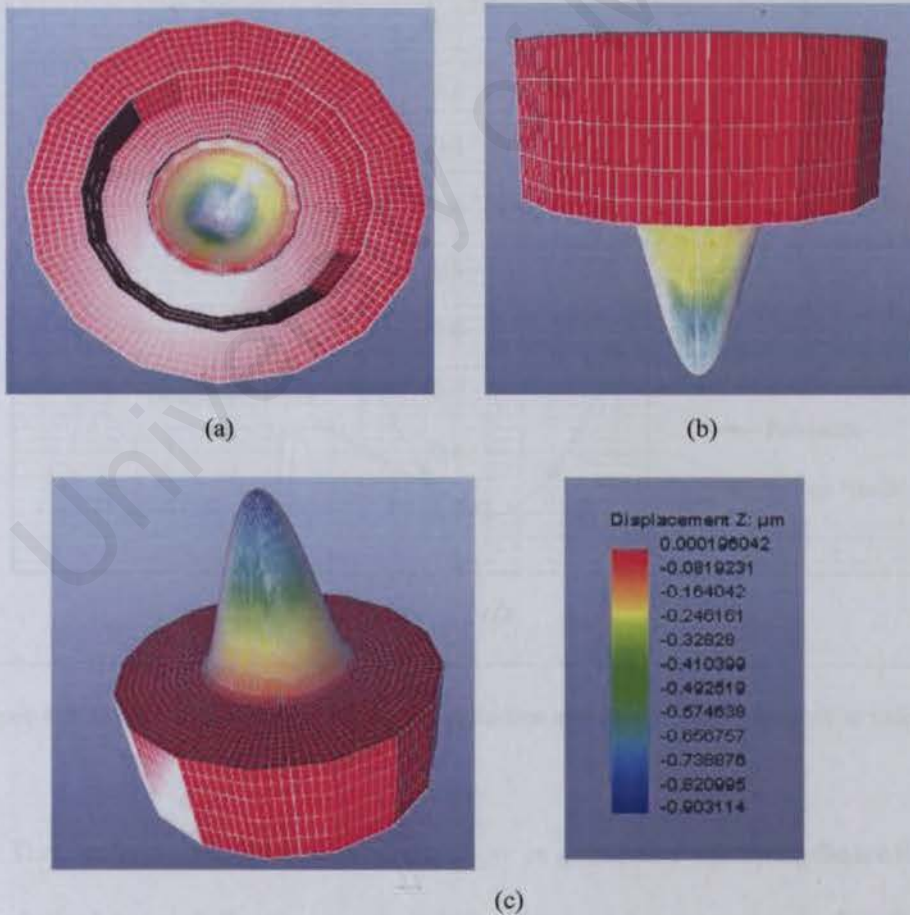


Figure 4.1: Diaphragm deflection from (a) top view (b) side view and (c) bottom view

This distribution of diaphragm deflection is further discussed using two-dimensional graph of deflection as shown in Figure 4.2. This figure illustrated the relationship between diaphragm deflection and ratio of radial distance to radius (r/a). It is concluded from this figure, that the polyimide diaphragm has higher deflection of $0.9 \mu\text{m}$ as compared to silicon nitride which only achieved a deflection of $0.02 \mu\text{m}$. The silicon nitride attained lower deflection than polyimide diaphragm due to its stiffness that will lead to the increment in its bending stress. This finding is in agreement with equation (3.4) and findings by (Xu, 2005 and Deng, 2004).

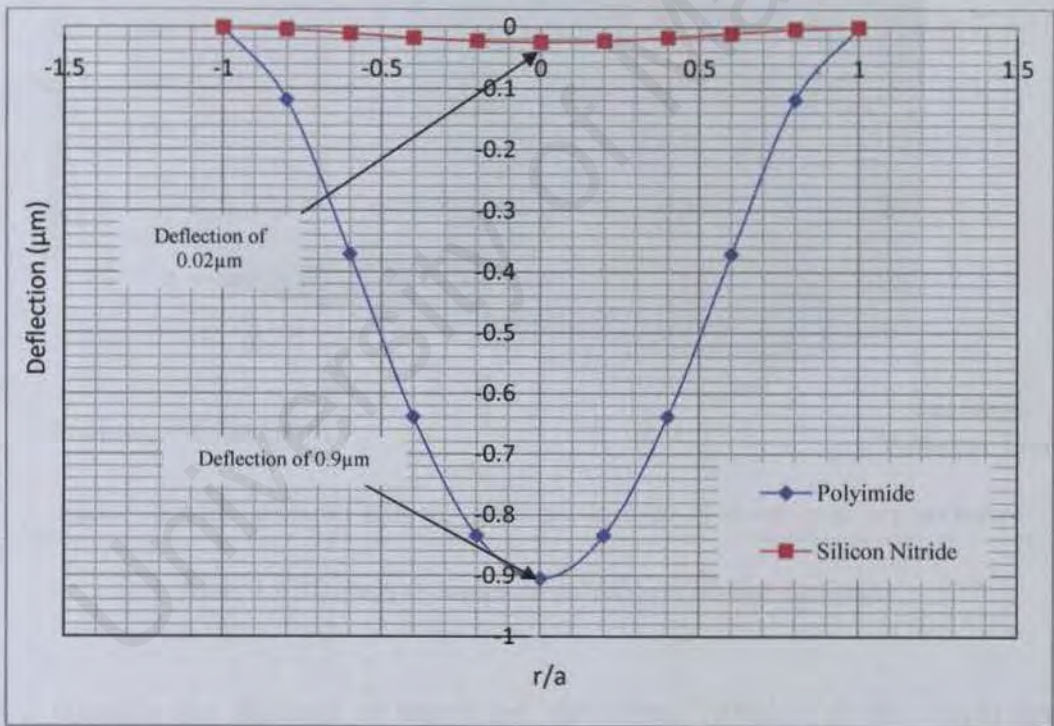


Figure 4.2: Relationship between diaphragm deflection and ratio of radial distance to radius (r/a)

The analysis of diaphragm deflection is presented in three-dimensional (3D) graph of diaphragm deflection as shown in Figure 4.3. At a particular diaphragm's

thickness, the deflection increases as the diaphragm radius is large. These results also indicate that the thin micro-diaphragm increases the diaphragm deflection. These behaviours are also supported by researchers' findings in (Xu, 2005, Deng, 2004, Madssen *et al.*, 2006, Osika *et al.*, 2007). In addition, the relationship between the diaphragm's deflection, radius and thickness is supported using equations 3.4 and 3.5.

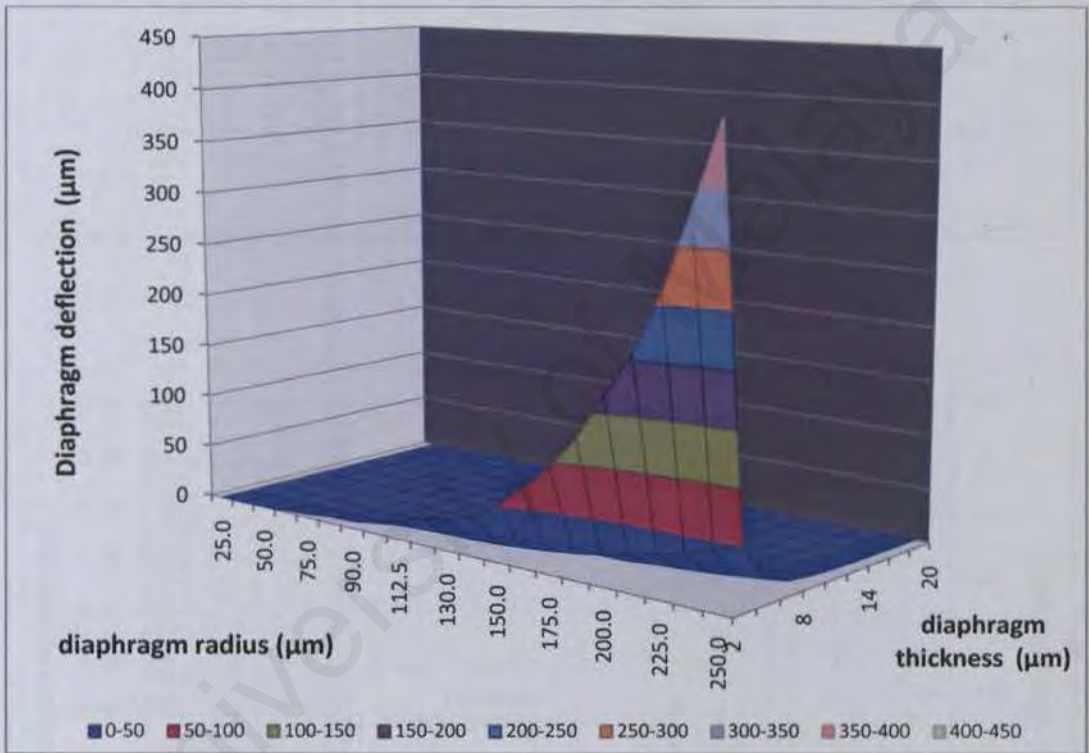
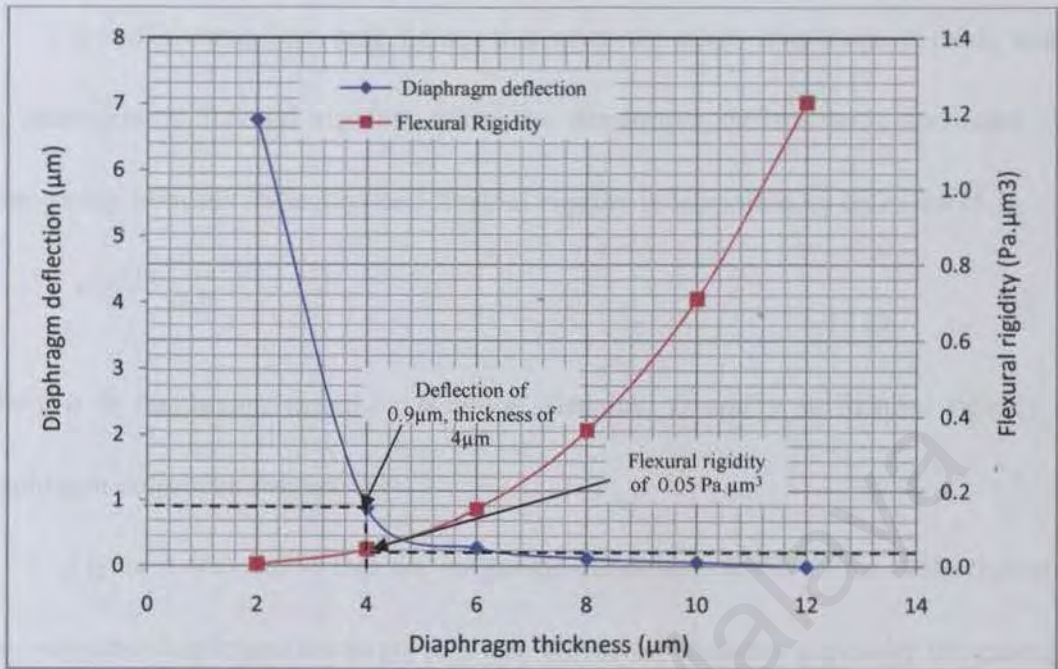
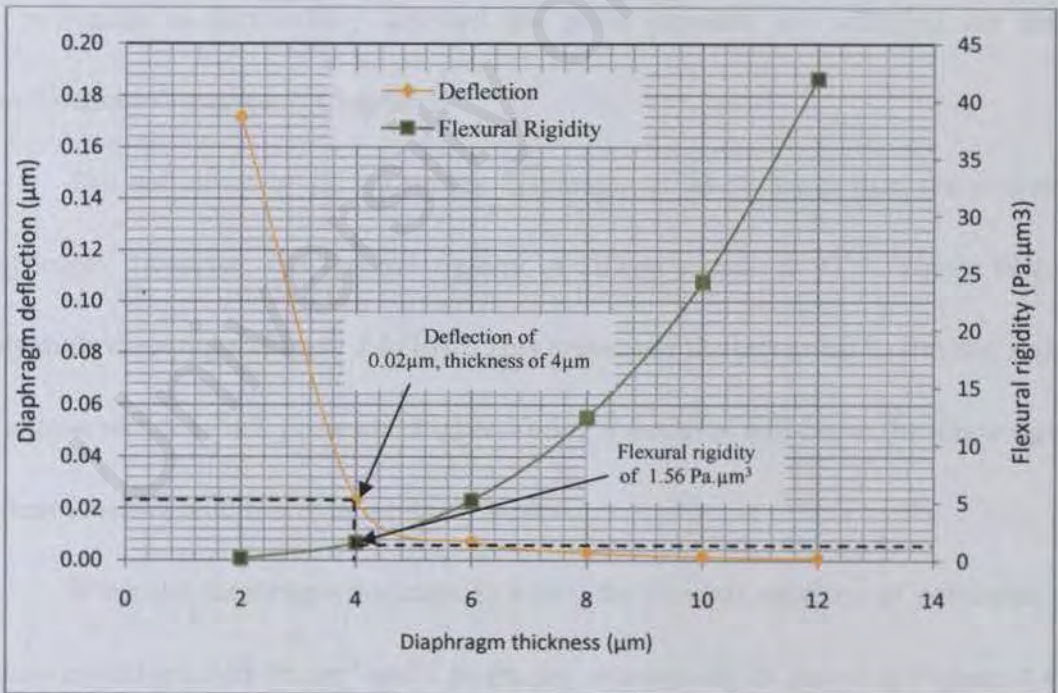


Figure 4.3: 3D graph of diaphragm deflection of circular diaphragm

Despite the analysis of diaphragm deflection, stiffness of the diaphragm is another important parameter which needs to be considered in designing a micro-diaphragm. The stiffness of the micro-diaphragm is presented in terms of its flexural rigidity. The relationship between diaphragm deflection and flexural rigidity for polyimide and silicon nitride are depicted in Figures 4.4 (a) and (b) respectively.



(a)



(b)

Figure 4.4: Diaphragm deflection and flexural rigidity versus diaphragm thickness for (a) polyimide diaphragm (b) silicon nitride diaphragm

It is illustrated from both figures that when the micro-diaphragm is thick, there is an increment in flexural rigidity, while the diaphragm deflection is decreased. This relationship between deflection and flexural rigidity is supported by equation (4.1):

$$y = \frac{P(a^2 - r^2)^2}{64 D} \quad (4.1)$$

where a is diaphragm radius, r is radial distance, D and y is flexural rigidity and diaphragm deflection respectively.

Figure 4.4(a) shows that the polyimide diaphragm achieved the deflection of 0.9 μm when the diaphragm thickness is 4 μm . However, with this particular thickness, the silicon nitride only attained 0.02 μm (Figure 4.4 (b)). The deflection of 0.9 μm achieved by polyimide is successfully detected the pulse pressure and satisfied the design specifications discussed in Chapter 3.

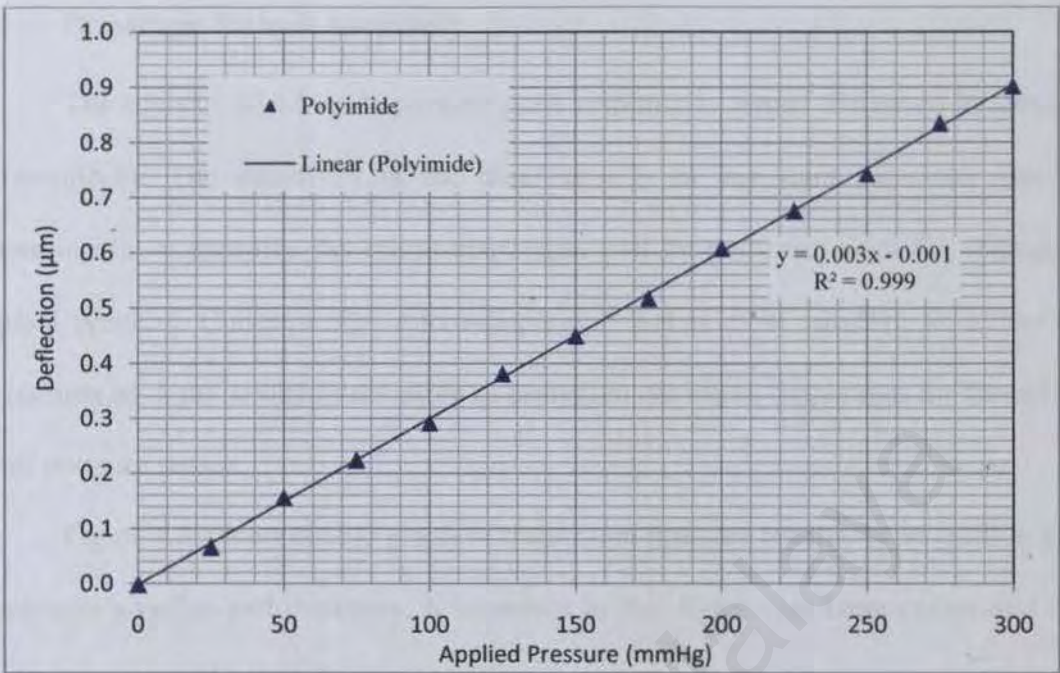
The deflection of silicon nitride diaphragm is 98 % lower than the polyimide diaphragm. However, the flexural rigidity of silicon nitride is 97 % higher than the polyimide diaphragm (Figure 4.4 (b)). This is because the increment in flexural rigidity of silicon nitride which possessed higher Young's modulus will cause the diaphragm to be less sensitive and thus reduced its deflection.

When the diaphragm thickness is 4 μm , the flexural rigidities of polyimide and silicon nitride are 0.05 $\text{Pa}\cdot\mu\text{m}^3$ and 1.56 $\text{Pa}\cdot\mu\text{m}^3$ respectively as shown in Figures 4.4 (a) and (b). It is concluded from Figures 4.4 (a) and (b) that the diaphragm thickness of 4 μm was chosen because it satisfied its design specifications as tabulated in Table 3.1.

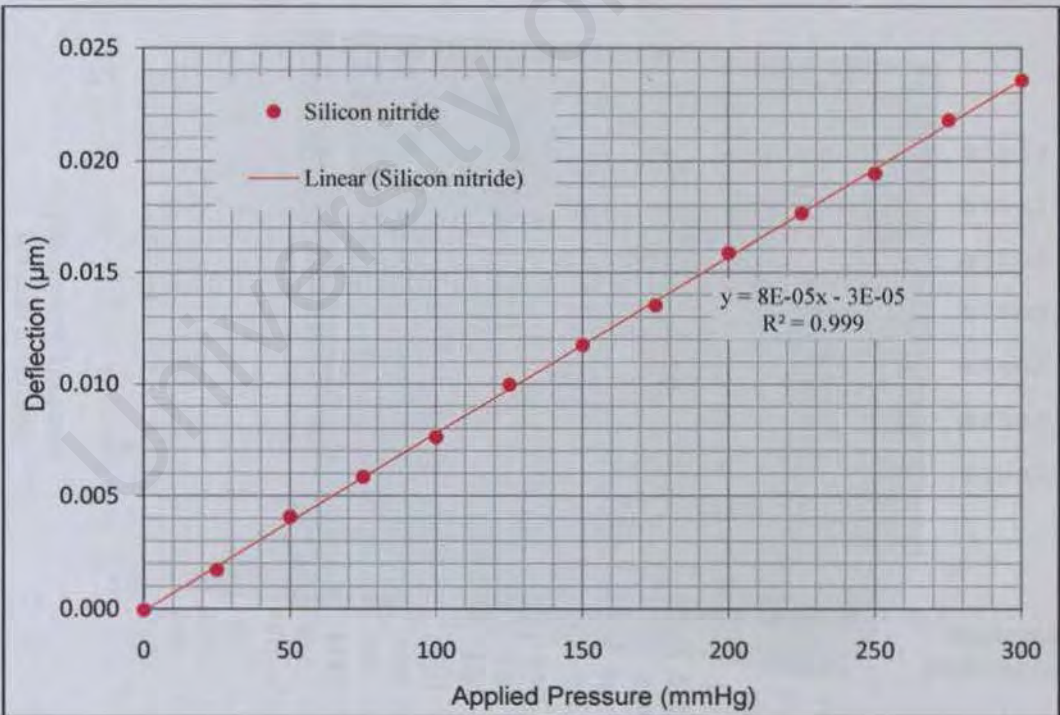
Based on this relationship between flexural rigidity and deflection, it is proven that the flexural rigidity is highly dependent on the diaphragm material. The material that possessed high Young's modulus increased the flexural rigidity and thus causing the diaphragm to obtain low deflection.

The analysis of diaphragm deflection is also discussed in terms of its linearity. The linearity of polyimide and silicon nitride diaphragms are presented in Figures 4.5 (a) and (b) respectively. Both figures depict that the deflection increased linearly with the applied pressure. The correlation coefficients, R^2 for linearity graph of polyimide and silicon nitride are 0.996 respectively. It is observed that the slopes for polyimide diaphragm (Figure 4.5(a)) and silicon nitride diaphragm (Figure 4.5(b)) are 3×10^{-3} and 8×10^{-5} respectively. In addition, it is proven that there is a difference of 97% in slope of linear equations between polyimide and silicon nitride. Based on the Figures 4.5 (a) and (b), it is also concluded that the higher slope of the graph provides higher deflection.

This linear relationship between deflection and applied pressure is highly desirable since it is easier to handle in calculation and measured (Giovanni, 1982, Soin and Majlis, 2002). However, the polyimide diaphragm obtained higher deflection than the silicon nitride. This phenomenon happened due to the low flexural rigidity in polyimide which successfully reducing bending stiffness. It is concluded that the polyimide diaphragm has achieved $0.9 \mu\text{m}$ when the maximum applied pressure of 300 mmHg was applied on to it (Figures 4.5(a)).



(a)



(b)

Figure 4.5: Simulation result shows relationship between diaphragm deflection and applied pressure for (a) polyimide (b) silicon nitride diaphragms

(ii) Diaphragm Pressure Sensitivity

The analysis of micro-diaphragm static response is further discussed in terms of its sensitivity. The sensitivity of the diaphragm is an important parameter since it determines how sensitive the micro-diaphragm will be deformed with the change of applied pressure. Consequently, micro-diaphragm that is most sensitive to deflect the diaphragm by 1 μm is highly desirable in designing the micro-diaphragm for the optical pulse pressure sensor.

Figure 4.6 shows the 3D graph of diaphragm pressure sensitivity in relation with diaphragm's radius and thickness. It is shown in this figure that large radius and thin micro-diaphragm has the highest sensitivity.

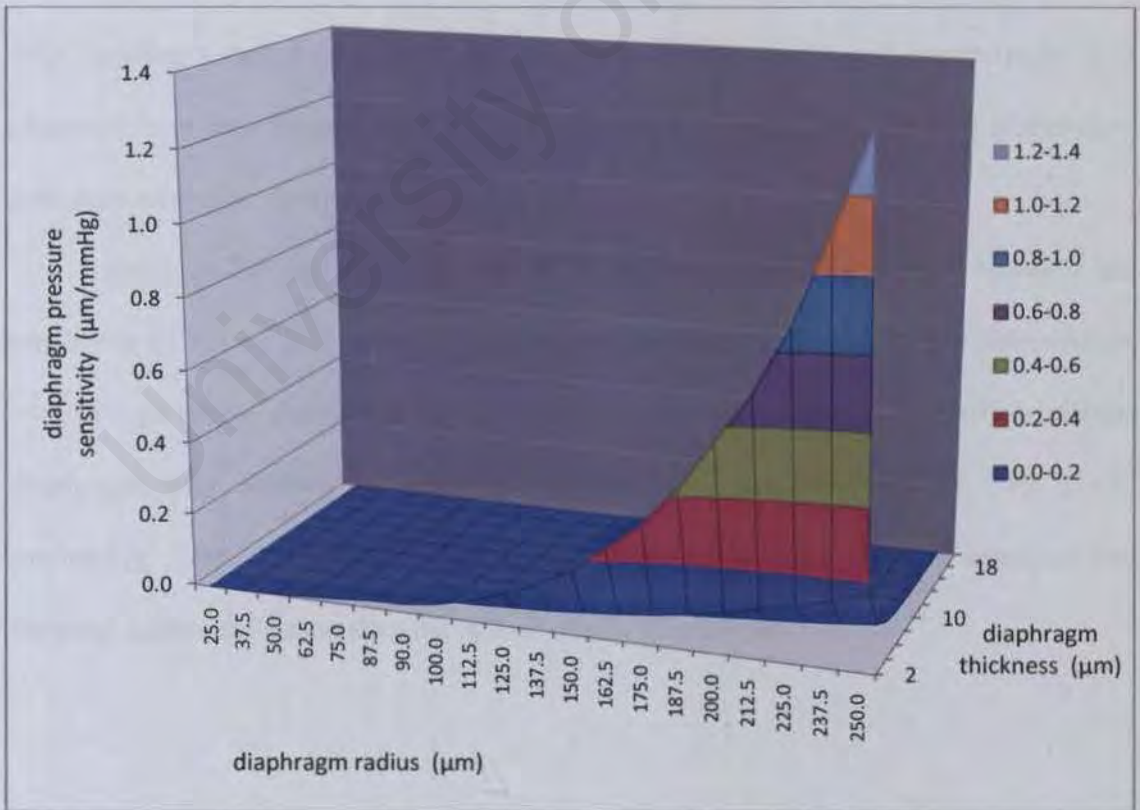


Figure 4.6: Relationship among sensitivity, diaphragm radius and diaphragm thickness

This is due to a decrement in the stiffness of the micro-diaphragm (Xu, 2005, Timoshenko, 1974) and is supported by equations (4.2) and (4.3) for polyimide and silicon nitride respectively:

$$Y_c(\text{polyimide}) = 2.194 \times 10^{-11} \frac{a^4}{h^3} (\mu\text{m} / \text{mmHg}) \quad (4.2)$$

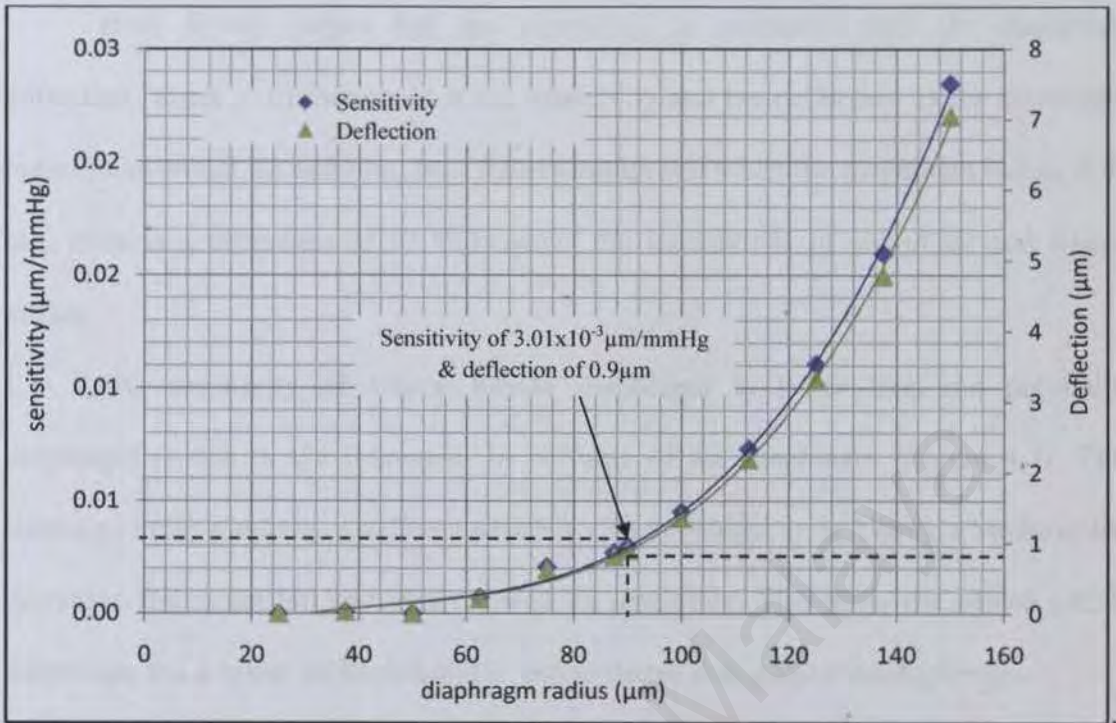
$$Y_c(\text{silicon nitride}) = 8.585 \times 10^{-11} \frac{a^4}{h^3} (\mu\text{m} / \text{mmHg}) \quad (4.3)$$

where a and h are in microns.

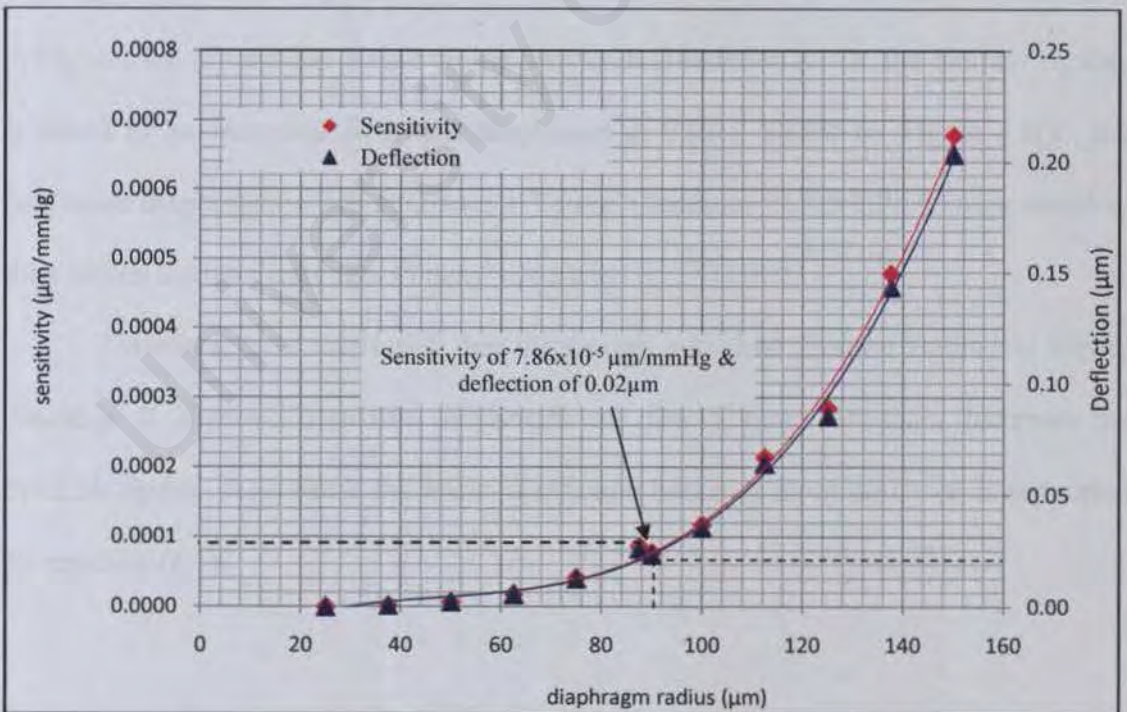
The analysis of sensitivity is discussed by referring to relationship between diaphragm's sensitivity and radius. The relationship of the diaphragm pressure sensitivity with variation of the diaphragm radius is shown in Figures 4.7 (a) and (b).

Figures 4.7 (a) and (b) illustrate the simulation results on sensitivity in relation with diaphragm radius for polyimide and silicon nitride diaphragms respectively. It is observed from both figures that the diaphragm pressure sensitivity for both diaphragms increased when the diaphragm radius is large.

Findings indicate that the polyimide diaphragm (Figure 4.7(a)) achieves the sensitivity of $3.01 \times 10^{-3} \mu\text{m}/\text{mmHg}$ when the diaphragm radius is $90 \mu\text{m}$. Meanwhile, with this particular diaphragm radius (diaphragm radius = $90 \mu\text{m}$), the silicon nitride diaphragm only attained its deflection of $0.02 \mu\text{m}$ and sensitivity of $7.86 \times 10^{-5} \mu\text{m}/\text{mmHg}$. Thus, it is attested that the polyimide diaphragm is more sensitive and obtained higher deflection than the silicon nitride diaphragm.



(a)



(b)

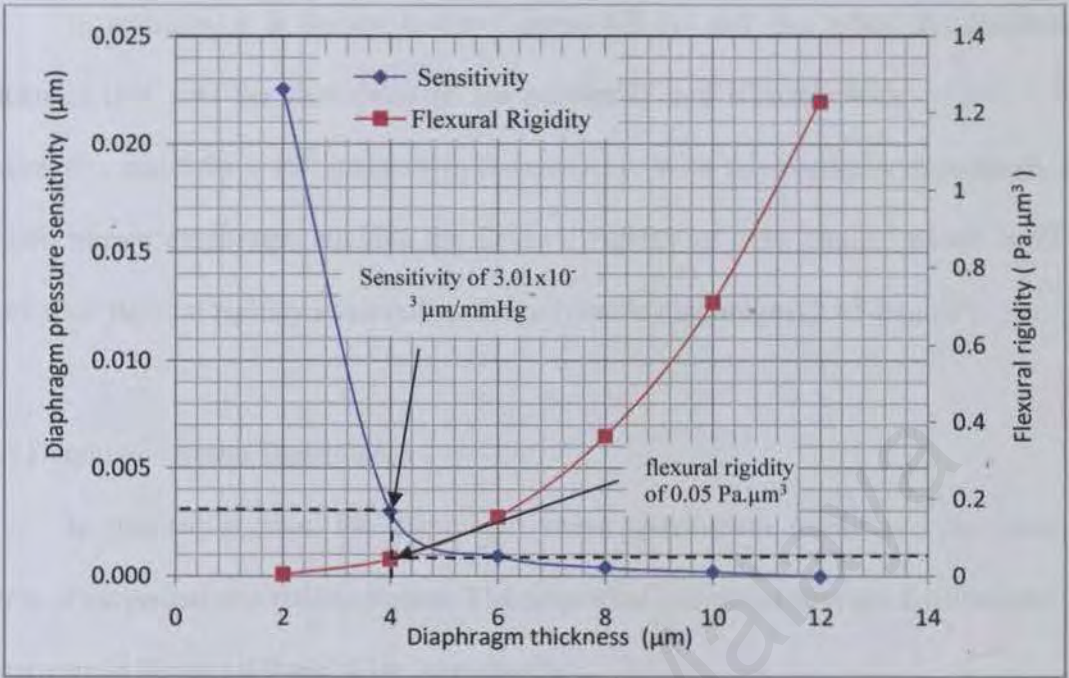
Figure 4.7: Simulation results show the sensitivity in relation with diaphragm radius for (a) polyimide and (b) silicon nitride diaphragms when the diaphragm thickness is 4 μm.

Both figures depict that the sensitivity is correlated with the diaphragm deflection. There is an increment in the sensitivity and the deflection as the diaphragm radius is increased. In addition, both figures depict that when the diaphragm radius is 90 μm , there is a difference of 97 % between the sensitivities of polyimide and silicon nitride.

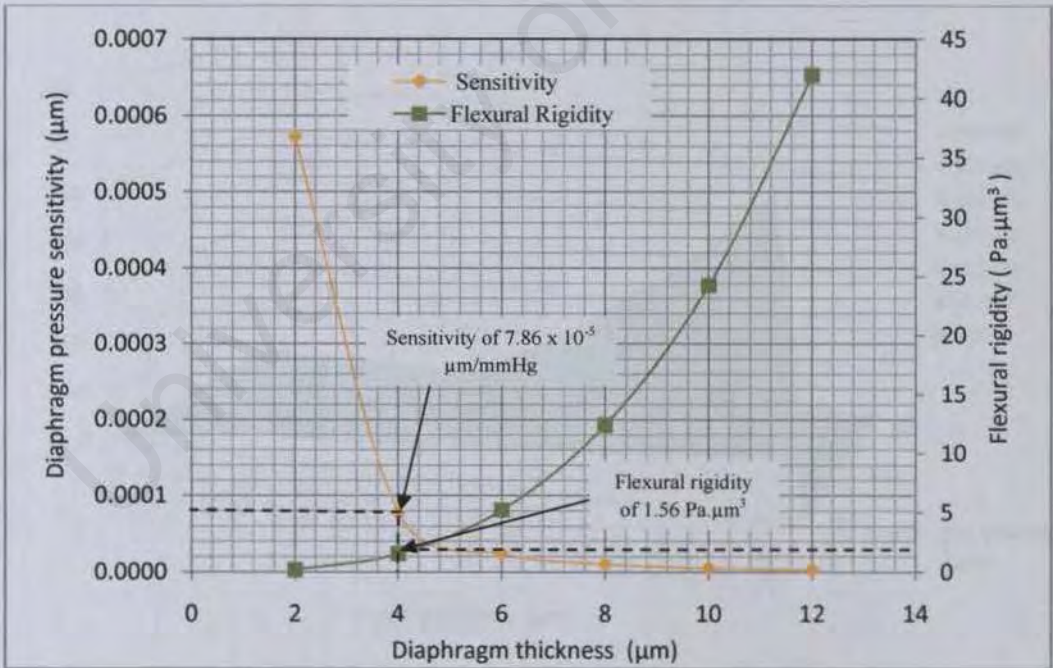
The sensitivity of silicon nitride diaphragm is lower than the polyimide diaphragm is due to the increment in stiffness of the diaphragm (Figure 4.7). This increased in the diaphragm stiffness which is closely related to its Young's Modulus has decreased the deflection and thus reduced its sensitivity. Therefore, the silicon nitride diaphragm has a lower deflection and is less sensitive than polyimide diaphragm.

The relationship of diaphragm pressure sensitivity and flexural rigidity with diaphragm thickness for polyimide and silicon nitride diaphragms are further discussed in Figures 4.8 (a) and (b). Based on the presented simulation result, the flexural rigidity is found to be increased when the diaphragm is thick. Based on Figure 4.8(a), the polyimide diaphragm which possesses a Young's modulus of 7.5 GPa is more sensitive than silicon nitride diaphragm (Young's modulus of 270 GPa).

Therefore, it is concluded that diaphragm with low flexural rigidity is highly desirable. It is proven that thin diaphragm and low Young's Modulus decreases the flexural rigidity. As a result the micro-diaphragm becomes more sensitive as supported by equation (4.1).



(a)



(b)

Figure 4.8: Sensitivity and flexural rigidity in relation with diaphragm thickness for (a) polyimide (b) silicon nitride

In addition, it is shown in the Figures 4.8 (a) and (b), when the diaphragm thickness is 4 μm , the sensitivity of the polyimide and silicon nitride is $3.01 \times 10^3 \mu\text{m}/\text{mmHg}$ and $7.86 \times 10^5 \mu\text{m}/\text{mmHg}$ respectively. With this particular dimension, the silicon nitride diaphragm attained the flexural rigidity of $1.56 \text{ Pa}\cdot\mu\text{m}^3$ which is 97 % more than flexural rigidity achieved by the polyimide diaphragm ($0.05 \text{ Pa}\cdot\mu\text{m}^3$).

(iii) Diaphragm Stress Distribution

In this sub-section, the diaphragm stress distribution results are discussed in terms of tangential and radial stresses. The tangential and radial stresses distributions are illustrated in Figures 4.9 and 4.10, respectively.

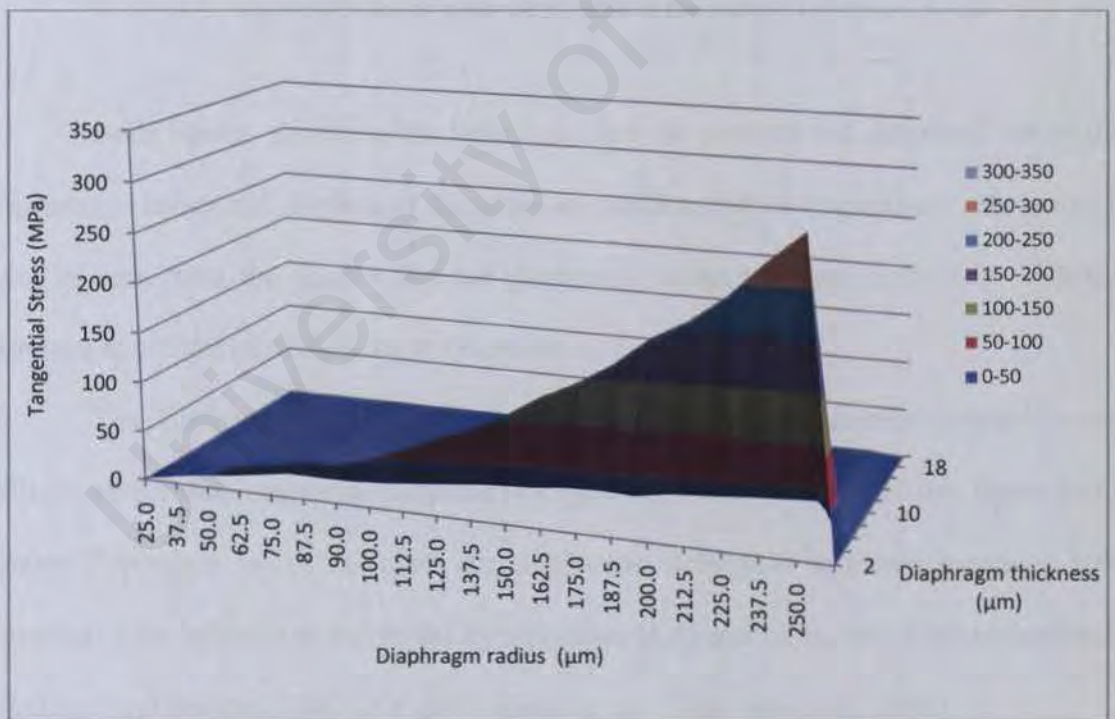


Figure 4.9: Tangential stress distribution of the diaphragm

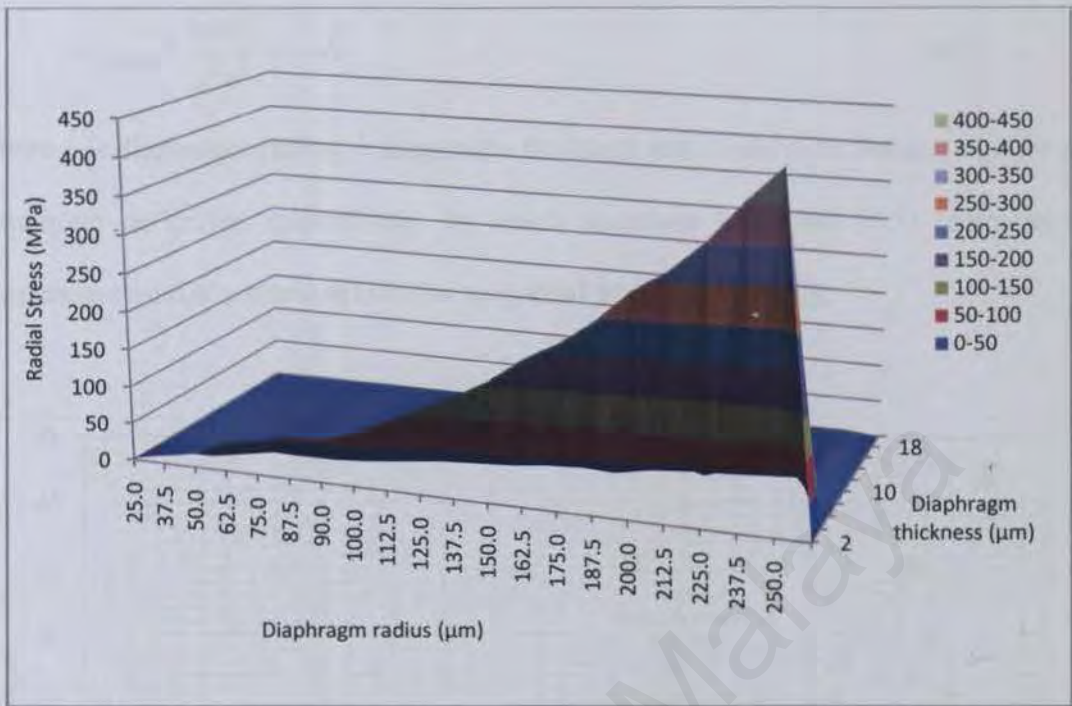


Figure 4.10: Radial stress distribution of the micro-diaphragm

Both figures show similar behaviour as both stresses are decreased when the diaphragm radius and diaphragm thickness are small and thick respectively. However, it can be seen from the figures that the diaphragm radius has more effects on both the stresses as compared to diaphragm thickness.

The comparison of stress and diaphragm deflection between polyimide and silicon nitride diaphragms is illustrated in Figure 4.11. It is shown from this figure that a larger diaphragm radius increases the diaphragm deflection and thus increases both stresses. This behavior is supported by equations (4.4) and (4.5), and other researchers' findings in (Giovanni, 1982, Xu, 2005, Eaton *et al.*, 1999, Sun *et al.*, 2008).

$$\sigma_{r,\max} = \frac{48Dy_c}{a^2h^2} \quad (4.4)$$

$$\sigma_{t,\max} = \frac{24Dy_c}{a^2h^2}(1+\mu) \quad (4.5)$$

where a is diaphragm radius, h diaphragm thickness and D and y_c is flexural rigidity and maximum deflection respectively. In which equations (4.4) and (4.5) represent the maximum radial stress and maximum tangential stress respectively.

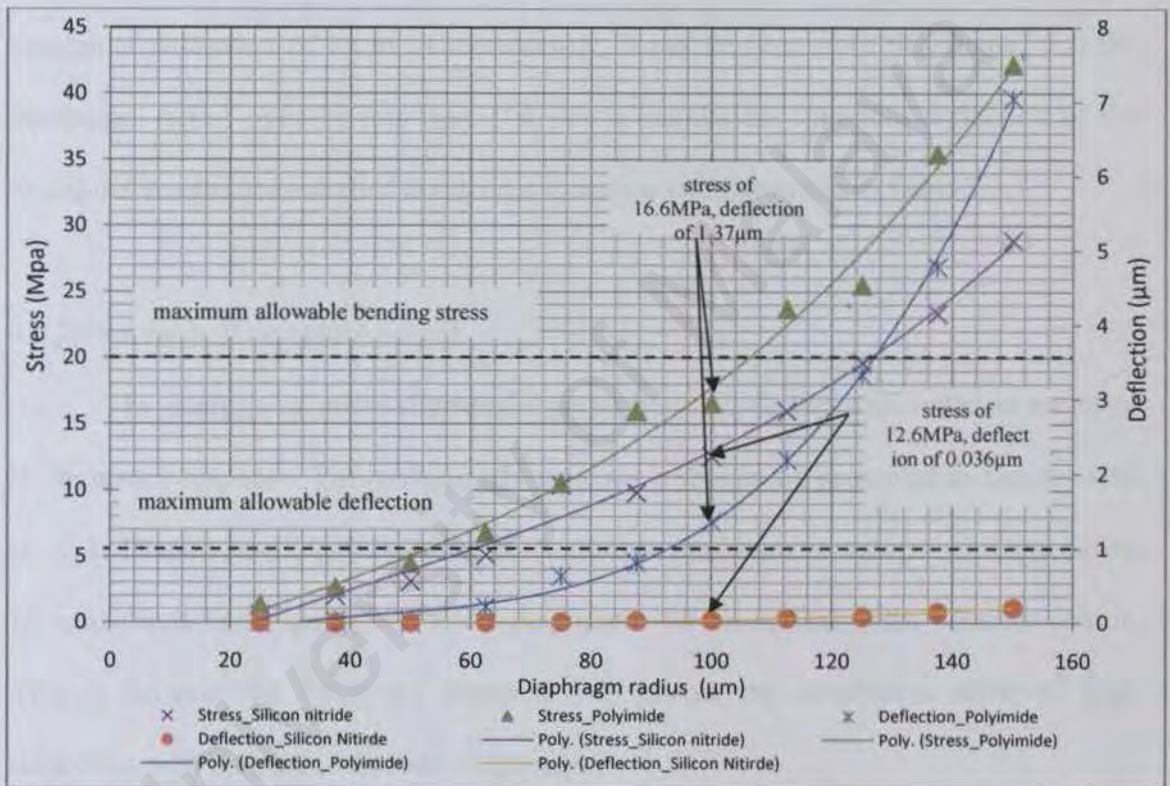


Figure 4.11: Simulation result on diaphragm deflection and stress in relation with diaphragm radius

It is observed from Figure 4.11, that the silicon nitride has lower deflection and stress as compared to the polyimide diaphragm. This is because the high Young's Modulus possessed by silicon nitride has increased its flexural rigidity and thus reduced its deflection. This finding is in agreement with equation (4.1).

This figure also shows that when the radius is $100\mu\text{m}$, the polyimide and silicon experienced bending stresses of 16.6 MPa and 12.6 MPa respectively. However, with this dimension, the polyimide diaphragm deflected by $1.37\ \mu\text{m}$ which exceeded the maximum allowable deflection of $1\ \mu\text{m}$.

Furthermore, the simulation results presented in Figure 4.11 shows that the micro-diaphragm must have the maximum bending stress of 20 MPa in order to attain maximum deflection of $1\ \mu\text{m}$. Consequently, it can be seen from this figure, that the diaphragm radius must be less than $100\ \mu\text{m}$ to acquire the optimum deflection of the micro-diaphragm and satisfied the design specifications presented in Table 3.1.

4.2.2 Frequency Response Analysis

The analysis of micro-diaphragm performance is further elaborated in terms of its frequency response. The analyses of frequency response are presented in Figures 4.12 to 4.17. Diaphragm frequency response is another important parameter which needs to be considered in designing the micro-diaphragm for an optical pulse pressure sensor. This is because the frequency response will ensure the diaphragm achieved high deflection with optimum vibration frequency.

The frequency response of the micro-diaphragm was presented in terms of its resonance frequency. This resonance frequency occurs when oscillation frequency matches a natural frequency possessed by the diaphragm. Thus, an oscillation with large amplitude is induced at this resonance frequency.

Figure 4.12 shows that when the diaphragm's radius and thickness are small and thick respectively, there will be an increment in the resonance frequency of the diaphragm. At a particular diaphragm radius, resonance frequency increases when

micro-diaphragm is thick. This result is supported by findings of Hong *et al.*, 2006 and equation (3.18).

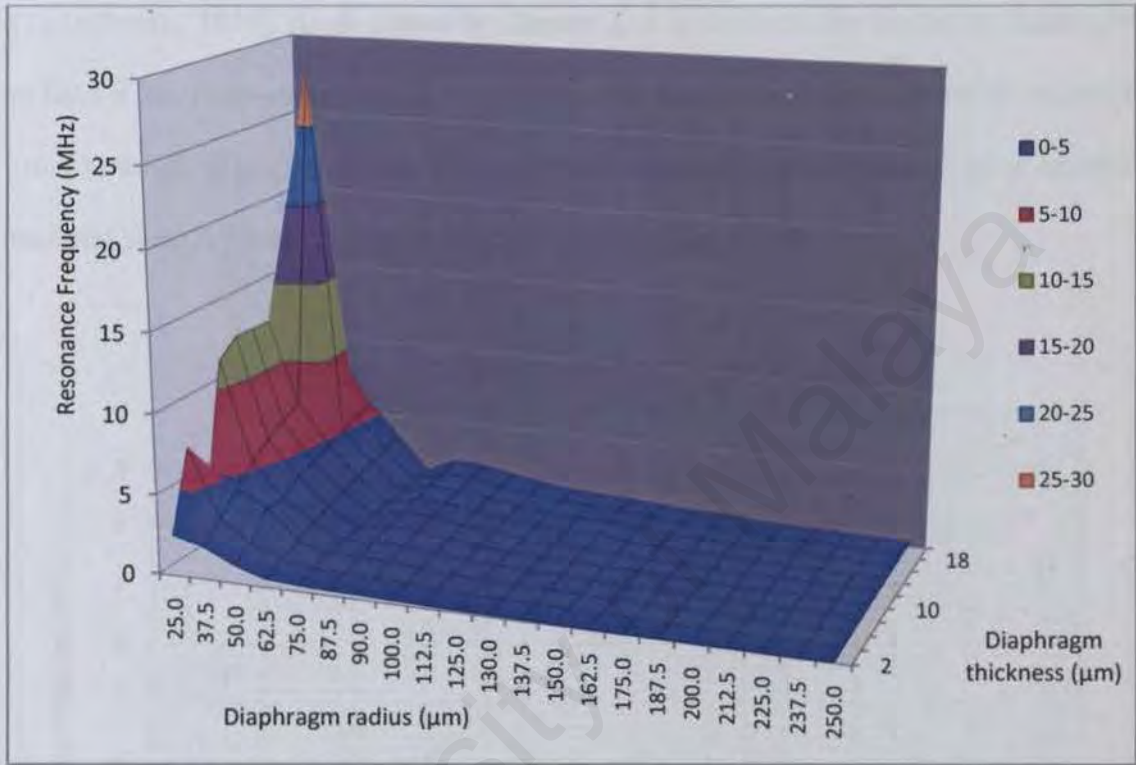


Figure 4.12: Relationship among diaphragm radius, diaphragm thickness and resonance frequency

The analysis of frequency response is discussed by studying the relationship between resonance frequency and diaphragm thickness. It is observed from Figure 4.13 that the resonance frequencies for polyimide and silicon nitride are linearly correlated with diaphragm thickness. Silicon nitride attained higher resonance frequency with the slope of 0.4311 and coefficient correlation, R^2 of 0.9908. Meanwhile, the polyimide diaphragm has a lower slope of 0.1099 which is 75 % difference from the slope of silicon nitride. It is shown in this figure that the higher slope indicated that the diaphragm vibrated in higher frequency (Figure 4.13).

Findings in Figure 4.13 also indicate that the polyimide diaphragm experienced less vibration since it achieved lower resonance frequency than silicon nitride. This is because, the vibration of the micro-diaphragm is influenced by its elasticity and mass (Timoshenko, 1974). As discussed in Chapter 3, it is desirable for the micro-diaphragm to have a low resonance frequency to successfully detect the-pulse pressure in the range from 0 to 50 kHz. Therefore, the polyimide diaphragm is attested to be a suitable material since it vibrates in lower frequency than silicon nitride.

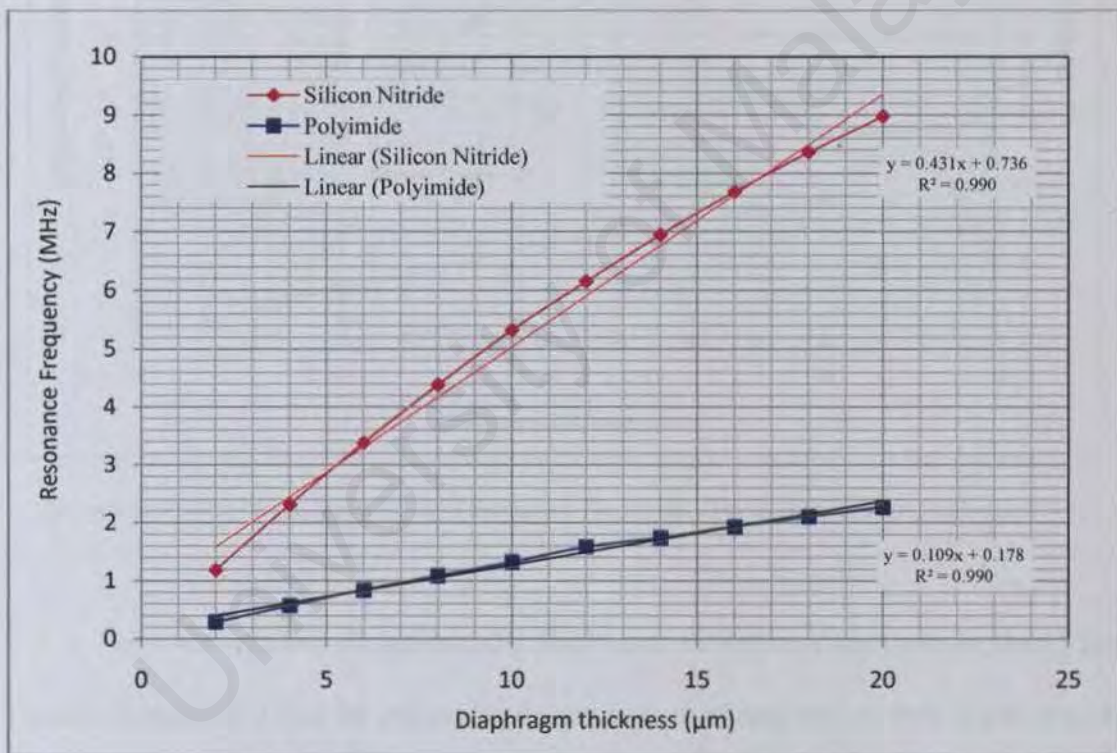


Figure 4.13: Resonance Frequency in relation with diaphragm thickness

The correlation between diaphragm deflection and resonance frequency is illustrated in Figure 4.14. In order to attain maximum deflection of 1µm, the thickness of diaphragm should be selected in the range of 0 to 5 µm. As shown in the figure, when the diaphragm thickness is 5 µm, the resonance frequencies of polyimide and silicon

nitride are 2.8 MHz and 0.6 MHz respectively. These resonance frequencies satisfied the design specification (Table 3.1) since both frequencies are 2.5 times larger than the applied frequency.

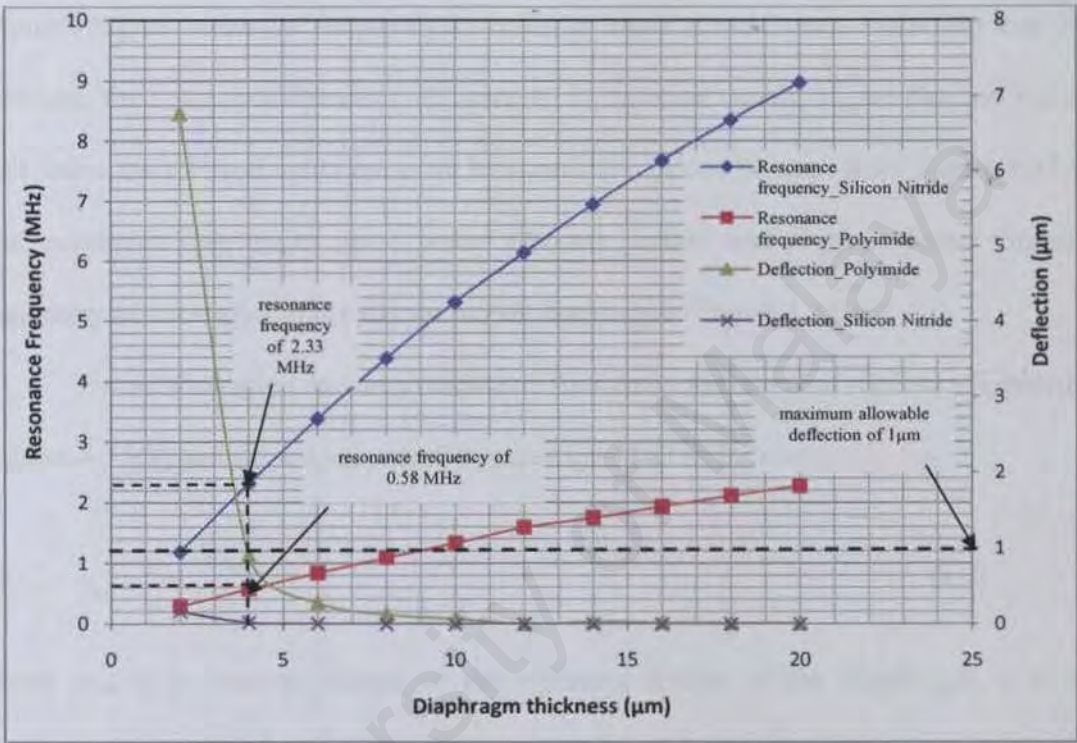


Figure 4.14: Diaphragm deflection and resonance frequency in relation with diaphragm thickness

However with this dimension, the diaphragm deflection exceeds more than 1 µm. Thus, it is concluded that the micro-diaphragm with thickness of less than 5 µm must be chosen to satisfy all specifications presented in Table 3.1. It is shown for diaphragm thickness of 4µm, the polyimide diaphragm vibrates at lower frequency of 0.58 MHz to achieve maximum deflection of 0.9 µm (Figure 4.14). Meanwhile, at the same thickness (4 µm), the silicon nitride requires higher vibration frequency of 2.33 MHz but it only attained very low diaphragm deflection of 0.02 µm.

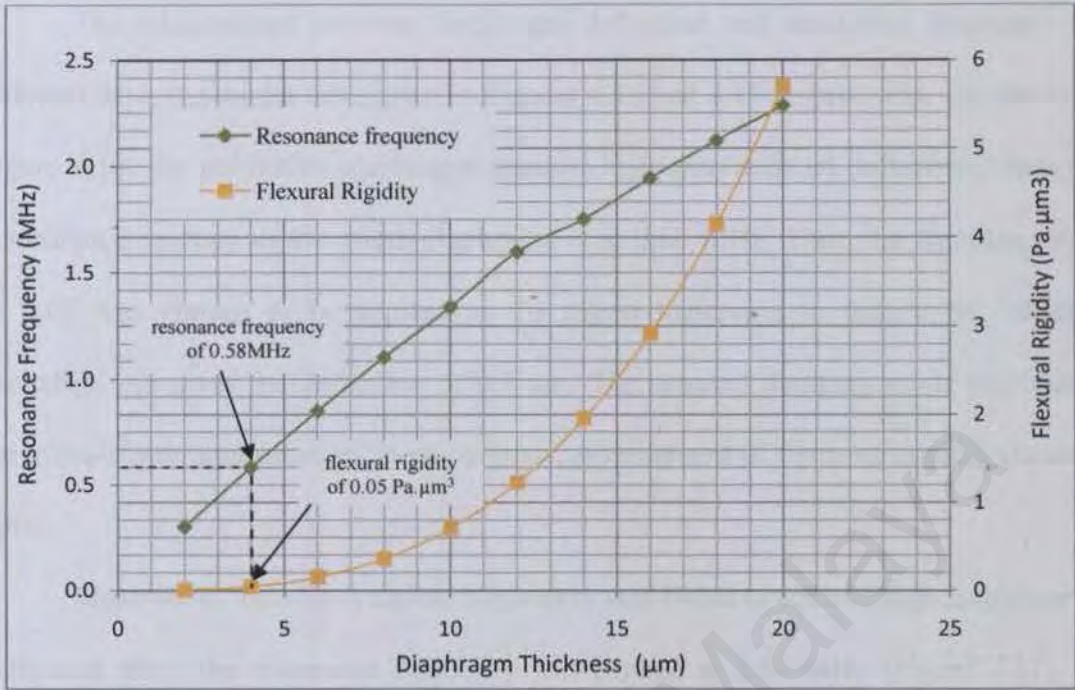
The analysis of frequency response is further discussed by investigating the relationship of flexural rigidity and resonance frequency with diaphragm thickness. Figures 4.15 (a) and (b) illustrate that the resonance frequency increased when the flexural rigidity was increased. It was found in this figure that thicker diaphragm requires higher vibration frequency in order to attain a maximum deflection and thus increases the resonance frequency (Figure 4.15). In other words, higher flexural rigidity will cause the micro-diaphragm to be less sensitive. It can be seen from Figure 4.15 (a) that polyimide diaphragm has a lower flexural rigidity and requires lower vibration frequency as compared to the silicon nitride diaphragm (Figure 4.15(b)).

The relationships between resonance frequency and flexural rigidity presented in Figures 4.15(a) and (b) are supported by equation (4.8) as follows:

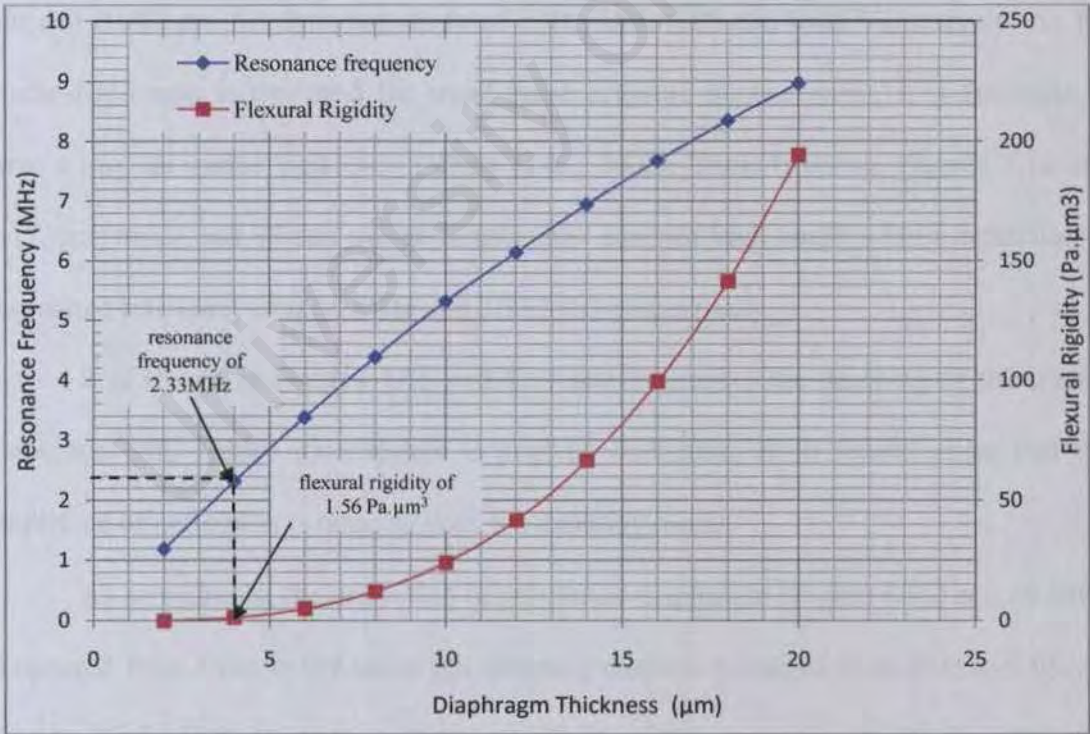
$$f_{mn} = \frac{\alpha_{mn}}{4\pi} \sqrt{\frac{4D}{\rho r^4 h}} \tag{4.8}$$

where α_{mn} is a constant related to the vibrating modes of the diaphragm, h is the thickness of the diaphragm, r is the effective diaphragm radius, ρ is the mass density of the diaphragm material, whereas D is the flexural rigidity of the micro-diaphragm.

Thus, it is observed from the Figures 4.14 and 4.15 that, at the thickness of 4 μ m, the polyimide diaphragm vibrates at frequency of 0.58 MHz and achieved the deflection of 0.9 μ m. These findings are in agreement with design specifications presented in Table 3.1.



(a)



(b)

Figure 4.15: Resonance Frequency and flexural rigidity in relation with diaphragm thickness for (a) Polyimide and (b) Silicon Nitride

The relationships between diaphragm deflection and resonance frequency for different damping modes are shown in Figures 4.16 and 4.17 respectively. As shown in Figure 4.16, the polyimide diaphragm attained high amplitude of deflection when the resonance frequency of the micro-diaphragm is at 0.66 MHz. Thus, the damping mode of 0.05 was chosen to be applied to the micro-diaphragm to reduce its vibration excitation and gives the deflection of 0.9 μm . The selected damping mode has caused the micro-diaphragm operated in an optimum environment of dynamic loading (Beards, 1996).

Meanwhile, the silicon nitride diaphragm was found to achieve high amplitude of deflection when the resonance frequency was excited at 2.33 MHz (Figure 4.17). At resonance frequency of 2.33 MHz, the deflections are given by 0.06 μm , 0.02 μm , 0.01 μm and 0.007 μm for damping mode of 0.01, 0.03, 0.05 and 0.08 respectively. As the micro-diaphragm is designed for small pulse pressure measurement, it is desirable to have a low resonance frequency (Wang *et al.*, 2006). Thus, from the Figures 4.16 and 4.17, polyimide and silicon nitride diaphragms attained high amplitude of deflection at resonance frequency of 0.66 MHz and 2.33 MHz respectively.

It is shown in Figures 4.16 and 4.17 that increasing the damping of the micro-diaphragm will reduce its response to a given excitation. Both figures show that the amplitude of deflection is reduced with the damping mode.

As an example, the deflection of polyimide diaphragm (Figure 4.16) at 0.66 MHz is reduced from 5 μm to 0.9 μm when damping mode is increased from 0.03 to 0.05. As the damping mode is increased, there will be a reduction in vibration, noise, and dynamic stress (Beards, 1996).

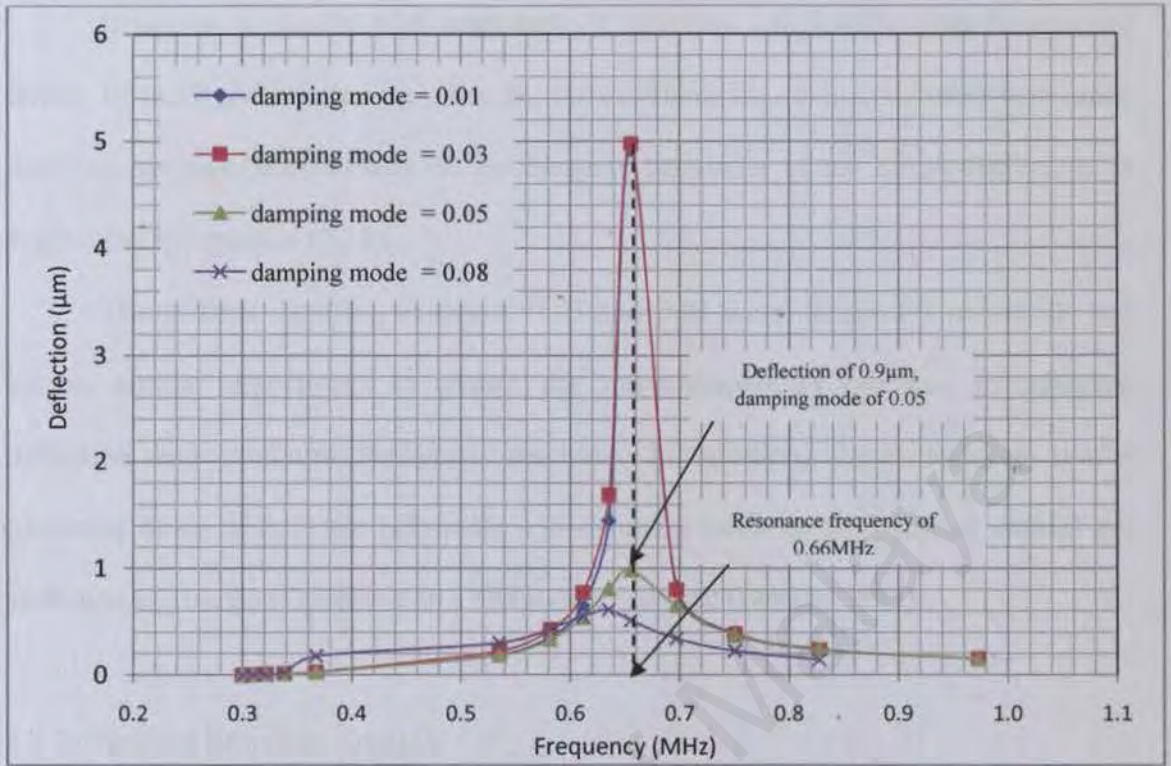


Figure 4.16: Diaphragm deflection versus frequency for polyimide diaphragm

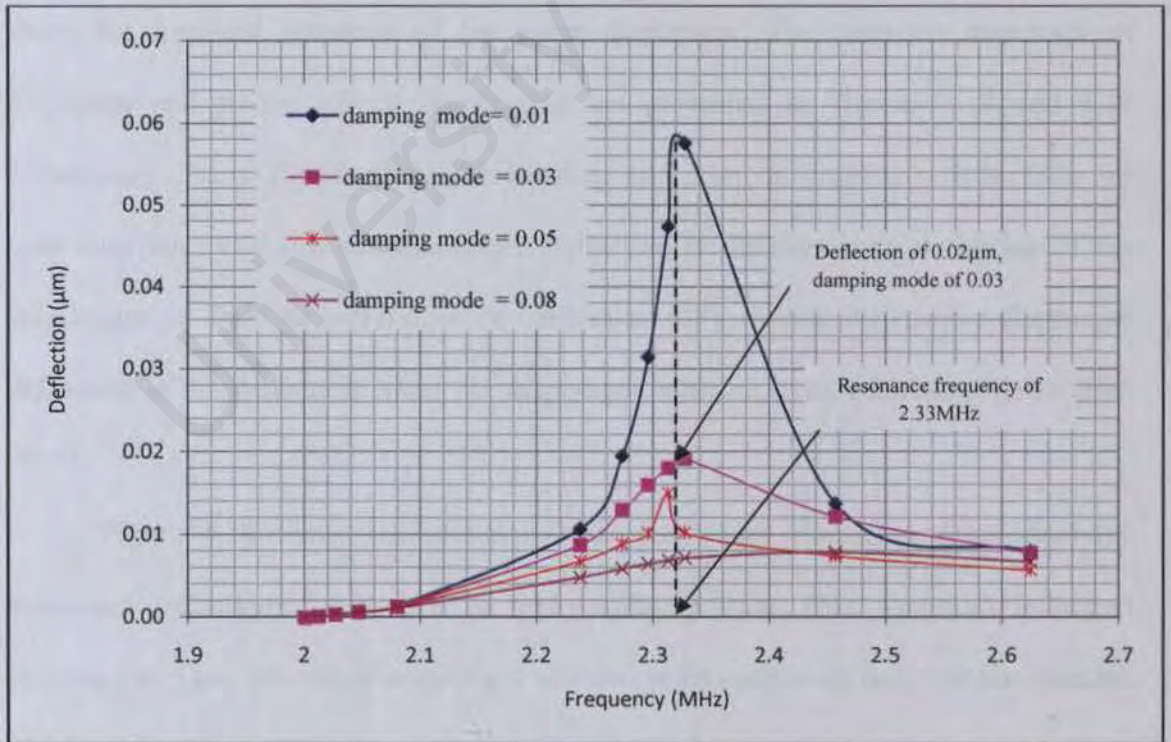


Figure 4.17: Diaphragm deflection versus frequency for silicon nitride diaphragm

However, excessive high amplitude of vibration will lead to both fatigue and failure of the micro-diaphragm (Beards, 1996). Therefore, it is concluded that mode damping has significant effects on the dynamic behaviour of the micro-diaphragm as supported by equation (3.18).

The suitable damping modes of 0.05 and 0.03 were chosen for polyimide and silicon nitride respectively to ensure the micro-diaphragm operated in adequate deflection and optimum frequency response. In addition, these damping modes (damping mode of 0.05 for polyimide and damping mode of 0.03 silicon nitride) are sufficient to give good response to a vibration excitation (Beards, 1996).

4.2.3 Transient Response Analysis

Since the micro-diaphragm is loaded with a time varying load, it is important to study the transient response of the micro-diaphragm. The transient responses of polyimide and silicon nitride diaphragms are presented in Figures 4.18 and 4.19 respectively. These figures show the absolute and relative diaphragm deflections for both materials. The absolute diaphragm deflection is the maximum deflection of the diaphragm, *i.e.* from its initial position (deflection = 0) whereas the relative diaphragm deflection is the deflection when the diaphragm vibrates at its oscillating point (Bao 2005).

Figure 4.18 shows that the polyimide diaphragm vibrates and achieves the maximum deflection of 0.9 μm at its first oscillating point. This maximum deflection happened at 5 μs . The micro-diaphragm vibrated at its oscillating point within duration of 1.8 μs .

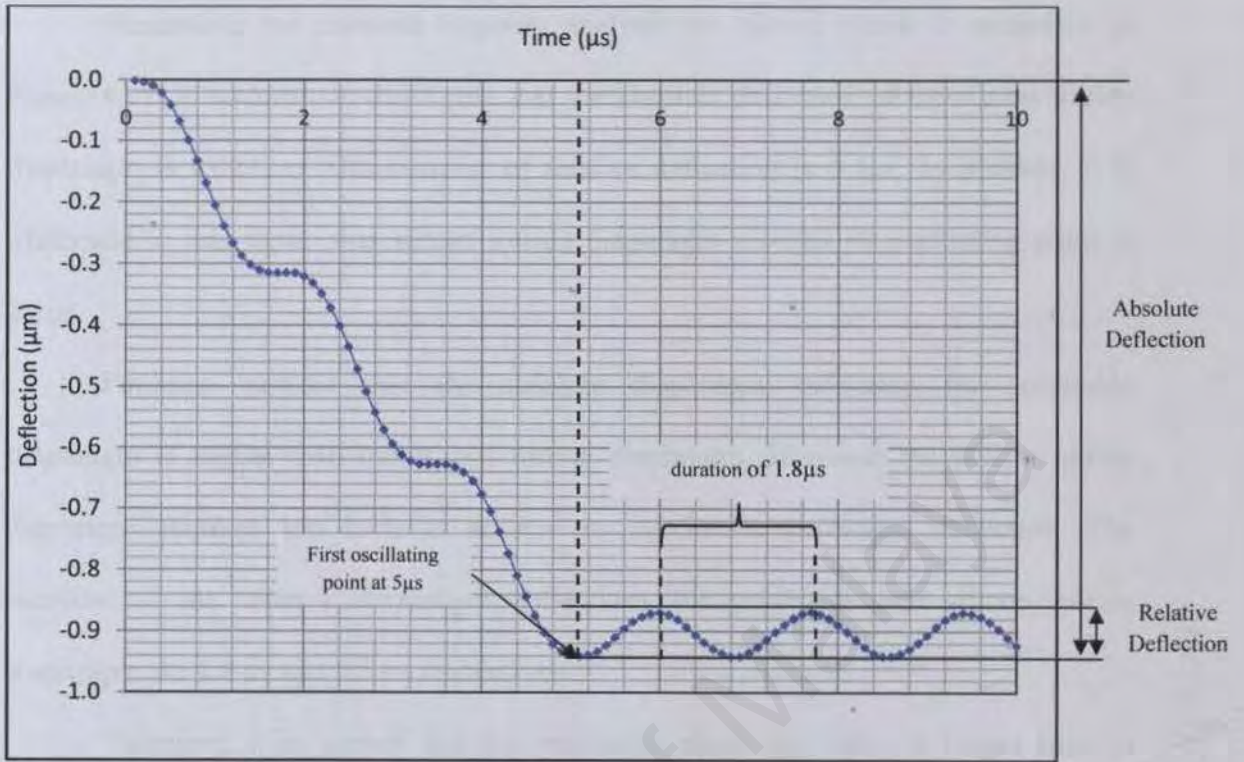


Figure 4.18: Deflection versus time for polyimide diaphragm

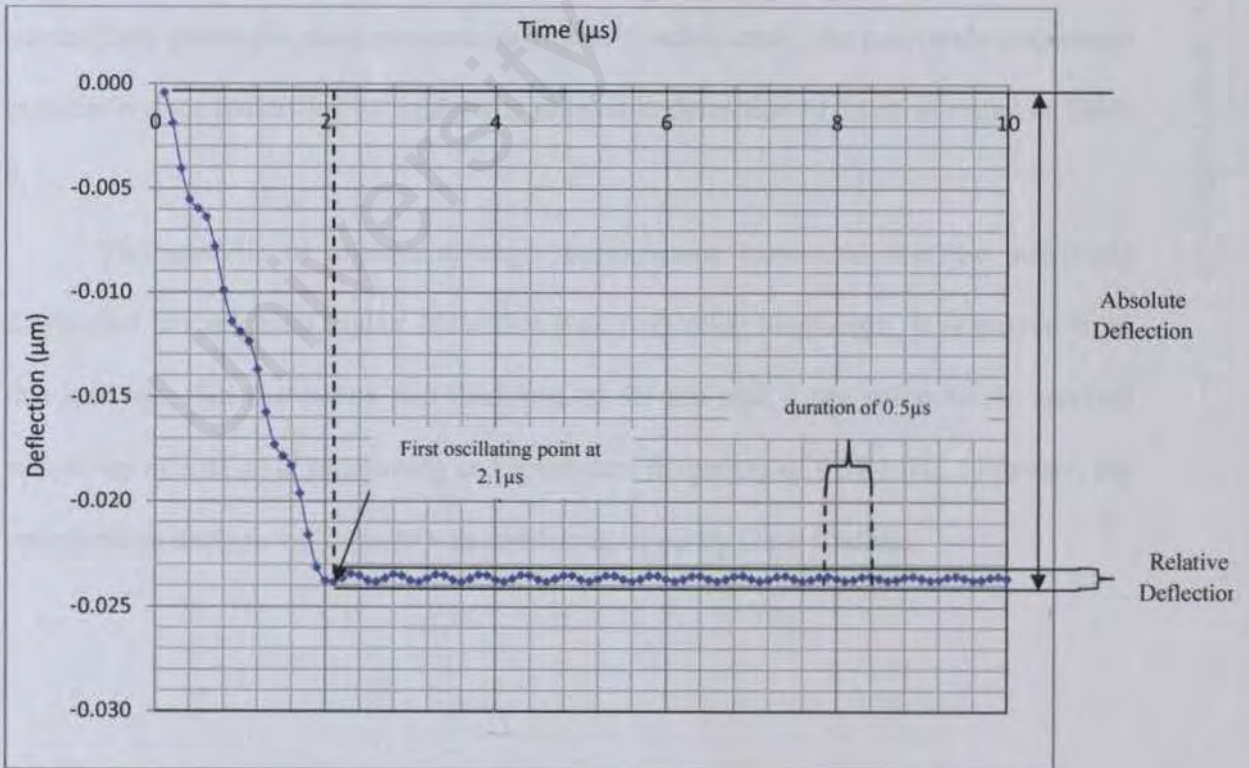


Figure 4.19: Deflection vs time for silicon nitride diaphragm

Meanwhile the transient response analysis for silicon nitride is presented in Figure 4.19. It is shown in this figure that the absolute deflection of the silicon nitride diaphragm is $0.024\mu\text{m}$ with duration of relative deflection is $0.5\mu\text{s}$. In addition, it is illustrated in this figure that silicon nitride diaphragm reached its oscillating point at $2.1\mu\text{s}$.

Findings indicate that the absolute diaphragm deflection for polyimide diaphragm is higher than the silicon nitride diaphragm. However the silicon nitride diaphragm requires less time to achieve its maximum diaphragm deflection. The duration of the relative diaphragm deflections for polyimide and silicon nitride diaphragm are $1.8\mu\text{s}$ and $0.5\mu\text{s}$ respectively.

Therefore, it is proven that the polyimide diaphragm takes a longer time to vibrate in order to achieve its maximum diaphragm deflection of $0.9\mu\text{m}$. As a result, to successfully detect the pulse pressure on human's radial artery, the polyimide diaphragm is suitable since it satisfies the maximum allowable deflection of $1\mu\text{m}$ as stated in Table 3.1.

The analysis of micro-diaphragm performance concluded that the polyimide diaphragm has achieved higher deflection than polyimide diaphragm. It is proven from this analysis, that the radius and thickness of $90\mu\text{m}$ and $4\mu\text{m}$ respectively attained sensitivity of $3.01 \times 10^3\mu\text{m}/\text{mmHg}$ and resonance frequency of 0.58MHz . However, the optimization analysis of Taguchi was conducted to verify these findings.

4.3 Optimization using Taguchi Method

The optimization result of Taguchi is divided into two parts namely analyses of S/N ratio and Pareto ANOVA.

4.3.1 Analysis of Signal-to-noise (S/N) ratio

The simulated and the calculated S/N ratio results for micro-diaphragm's deflection, sensitivity and resonance frequency performance are presented in Table 4.1. The mean S/N ratios for each level of control factors and control factor interactions for the larger the better characteristics are shown in Table 4.2 and Figure 4.20. From Table 4.2, it was observed that the control factor A2 (*i.e.* diaphragm radius of 90 μm) gives the highest value of mean S/N ratio which are -145.23 dB, and 194.77 dB for deflection and sensitivity respectively.

Table 4.1: Simulated and calculated S/N ratio results for diaphragm deflection, diaphragm pressure sensitivity and resonance frequency

Simulation trials	Factors	Simulated results			Calculated S/N Ratio		
		Deflection (μm)	Sensitivity ($\mu\text{m}/\text{mmHg}$)	Resonance Frequency (MHz)	The larger-the-better characteristic		The smaller-the-better characteristic
					Deflection (dB)	Sensitivity (dB)	
1	A1B1C1	0.00409	1.36E-5	1.82507	-167.77	-217.31	-125.23
2	A2B1C1	0.90311	3.01E-3	0.58440	-120.89	-170.43	-115.33
3	A1B2C1	0.01414	1.25E-6	3.26307	-156.99	-226.53	-130.27
4	A2B2C1	0.12614	4.21E-4	1.10278	-137.98	-187.53	-120.85
5	A1B1C2	0.00241	8.05E-6	6.41726	-172.34	-221.88	-136.15
6	A2B1C2	0.02359	7.86E-5	2.32698	-152.55	-202.09	-127.34
7	A1B2C2	0.00038	1.25E-6	13.01840	-188.52	-238.06	-142.29
8	A2B2C2	0.00335	1.12E-5	4.39525	-169.50	-219.04	-132.86

The diaphragm's thickness (*i.e.* control factor B) and material (*i.e.* control factor C) are insignificant on the mean S/N ratio response for the larger the better characteristic of these two micro-diaphragm performance. In addition, the interaction between diaphragm thickness and diaphragm material (*i.e.* interaction BXC) are significant since it achieves the highest value of mean S/N ratio.

Table 4.2: Response Table of Mean S/N ratio for the larger the better characteristic of diaphragm deflection, and diaphragm pressure sensitivity

The larger the better characteristic								
Micro-diaphragm performance/ Control Factor	Diaphragm radius (A)		Diaphragm Thickness (B)		Diaphragm Material (C)		Interaction diaphragm thickness and diaphragm material, (B X C)	
	A1	A2	B1	B2	C1	C2	B1 X C1	B2 X C2
Deflection	-171.40	-145.23	-153.39	-163.25	-145.91	-170.73	-144.33	-179.01
Sensitivity	-220.95	-194.77	-202.93	-212.79	-195.45	-220.27	-193.87	-228.55

*Values of S/N ratios are in decibel, (dB)

Table 4.3: Response Table of Mean S/N ratio for smaller the better characteristic of resonance frequency

The smaller the better characteristic								
Micro-diaphragm performance/ Control Factor	Diaphragm radius (A)		Diaphragm Thickness (B)		Diaphragm Material (C)		Interaction between diaphragm radius & diaphragm thickness, (A X B)	
	A1	A2	B1	B2	C1	C2	A1X B1	A2X B2
Resonance Frequency	-123.48	-124.10	-126.01	-131.57	-122.92	-134.66	-130.69	-126.86

*Values of S/N ratios are in decibel, (dB)

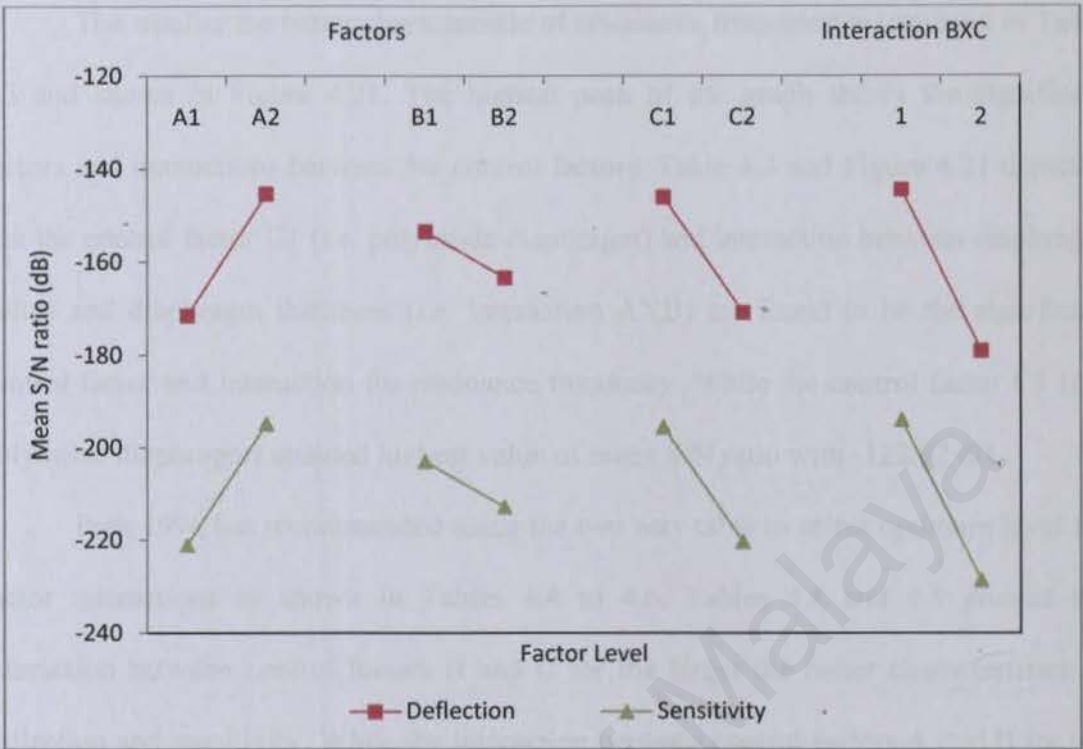


Figure 4.20: The mean signal-to-noise ratio graph for diaphragm deflection and diaphragm pressure sensitivity

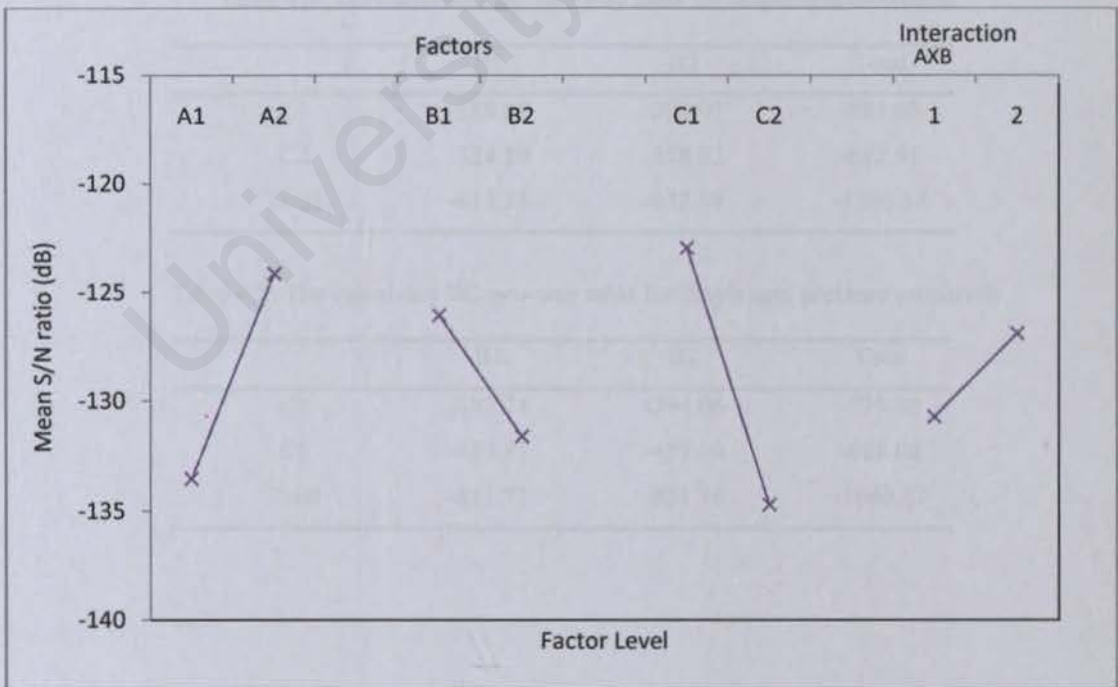


Figure 4.21: The mean signal-to-noise ratio graph for resonance frequency

The smaller the better characteristic of resonance frequency is tabulated in Table 4.3 and shown in Figure 4.21. The highest peak of the graph shows the significant factors and interactions between the control factors. Table 4.3 and Figure 4.21 depicted that the control factor C1 (*i.e.* polyimide diaphragm) and interaction between diaphragm radius and diaphragm thickness (*i.e.* interaction AXB) are found to be the significant control factor and interaction for resonance frequency. While the control factor C1 (*i.e.* polyimide diaphragm) attained highest value of mean S/N ratio with -122.92 dB,

Park 1996 has recommended using the two way table to select optimum level for factor interactions as shown in Tables 4.4 to 4.6. Tables 4.4 and 4.5 present the interaction between control factors B and C for the larger the better characteristics of deflection and sensitivity. While the interaction between control factors A and B for the smaller the better characteristic of resonance frequency is presented in Table 4.6.

Table 4.4: The calculated BC two-way table for diaphragm deflection

	B1	B2	Total
C1	-288.65	-294.97	-583.63
C2	-324.89	-358.02	-682.91
Total	-613.54	-652.99	-1266.53

Table 4.5: The calculated BC two-way table for diaphragm pressure sensitivity

	B1	B2	Total
C1	-387.74	-394.06	-779.80
C2	-423.97	-457.10	-881.08
Total	-811.71	-851.16	-1660.87

Table 4.6: The calculated AB two-way table for resonance frequency

	A1	A2	Total
B1	-261.37	-242.67	-504.04
B2	-272.56	-253.71	-526.27
Total	-533.93	-496.38	-1030.31

The optimum level for the interaction is indicated by the highest value in that particular two-way table. Thus, from these two-way tables, it was found that B1 and C1 are the optimum control factors for the larger the better characteristics. Table 10 shows the optimum control factors for the smaller the better characteristics are A2 and B1 (-242.67 dB).

Thus, analysis of S/N ratio summarized that the diaphragm radius of $90\mu\text{m}$ (*i.e.* Control Factor A2), diaphragm thickness of $4\mu\text{m}$ (*i.e.* Control Factor B1) and polyimide diaphragm (*i.e.* Control Factor C1) are the optimum combination to achieve the high deflection and sensitivity as well as low resonance frequency.

4.3.2 Analysis of Pareto ANOVA

The Pareto ANOVA analyses of diaphragm's deflection, pressure sensitivity and resonance frequency are summarized in Tables 4.7, 4.8 and 4.9 respectively. The optimum level of each control factor was indicated by the highest value of contribution ratio.

The Pareto diagrams in Figures 4.24 (a) and 4.24 (b) show that the diaphragm radius (*i.e.* Control Factor A) is most likely to give more influence in affecting the diaphragm's deflection and pressure sensitivity. However, for the smaller the better

characteristic, the diaphragm material (*i.e.* Control Factor C) obtained the highest contribution ratio as shown in Figure 4.24 (c).

Table 4.7: Pareto ANOVA analyses for diaphragm deflection

Factor	A	B	C	Total
Sum at factor level				
1	-666.60	-613.54	-583.63	
2	-580.92	-633.98	-663.89	
Sum of squares of differences	7341.72	417.75	6442.86	14262.33
Contribution ratio (%)	51.69	2.94	45.37	100
Optimum Level	A2	B1	C1	

Table 4.8: Pareto ANOVA analyses for diaphragm pressure sensitivity

Factor	A	B	C	Total
Sum at factor level				
1	-915.31	-811.71	-813.32	
2	-779.09	-882.69	-881.078	
Sum of squares of differences	18557.48	5038.06	4591.14	28186.68
Contribution ratio (%)	65.84	17.87	16.29	100
Optimum Level	A2	B1	C1	

Table 4.9: Pareto ANOVA analyses for resonance frequency

Factor	A	B	C	Total
Sum at factor level				
1	-533.94	-504.04	-491.68	
2	-496.38	-526.27	-538.63	
Sum of squares of differences	1410.51	494.19	2204.44	4109.14
Contribution ratio (%)	34.33	12.03	53.65	100
Optimum Level	A2	B1	C1	

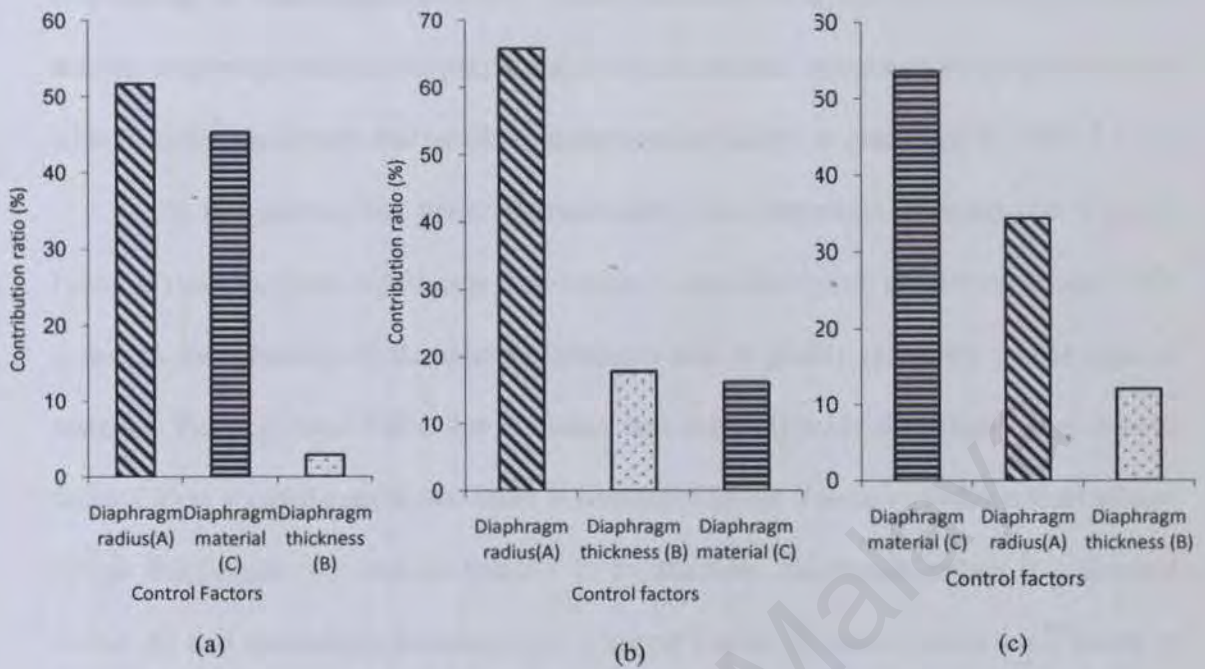


Figure 4.22: Pareto diagram for (a) diaphragm deflection (b) diaphragm pressure sensitivity and (c) resonance frequency

The Pareto ANOVA analysis presented in Figure 4.22 (a) showed that the effect of diaphragm radius contributes 51.69 % on diaphragm deflection followed by diaphragm material and diaphragm thickness at 45.37 % and 2.94 % respectively. It is illustrated in this figure that the diaphragm's radius and material achieved high contribution ratio on the diaphragm deflection. This means that the variations in diaphragm's radius and material will affect the deflection of the diaphragm. The diaphragm thickness (*i.e.* control factor B) is insignificant in affecting the larger the better characteristic of diaphragm deflection.

Figure 4.22 (b) indicates that the diaphragm's thickness (*i.e.* control factor B) and material (*i.e.* control factor C) are insignificant since their contribution ratios are lower as compared to diaphragm radius (*i.e.* control factor A). The diaphragm radius is more significant since it attained a contribution ratio of 65.84 % and has more influence

in affecting the diaphragm sensitivity. Therefore, it can be concluded from this analysis that the diaphragm radius will play a major role in order to achieve the best performance with adequate sensitivity and satisfied design specifications as presented in Table 3.1.

For the smaller the better characteristic, the diaphragm material (*i.e.* Control Factor C) was the most significant factor since it attained highest contribution ratio. This is due to the vibration of the micro-diaphragm that is greatly influence by the type of material. Finding from Table 4.9 indicates that the polyimide diaphragm (*i.e.* control factor C1) is a significant factor since it possessed lower Young's modulus than silicon nitride diaphragm (*i.e.* control factor C2) In addition, diaphragm radius (*i.e.* Control Factor A) and diaphragm thickness (*i.e.* Control Factor B) have contribution ratios of 34.32 % and 12.03 % respectively. Table 4.1 and Figure 4.24 (c) showed that the resonance frequency was equal to 0.5844 MHz which is 2.5 larger than the applied frequency. Thus, the control factors of A2, B1 and C1 are the optimum combination for the micro-diaphragm and it satisfied the design specifications presented in Table 3.1.

Thus, it is found that the optimum control factors with combination of control factors A2, B1, and C1 from the S/N ratio Pareto ANOVA analyses were similar with the second simulation trials, whereby the diaphragm's pressure sensitivity and deflection was equal to 0.00301 $\mu\text{m}/\text{mmHg}$ and 0.90311 μm respectively. With this optimum combination, the micro-diaphragm achieved the best performance with low vibration frequency and adequate sensitivity to detect the pulse pressure on human's radial artery.

4.4 Summary

The micro-diaphragm performance and optimization analyses using the Taguchi method have been presented in this chapter. Based on the simulation results, it is

concluded that the diaphragm deflection and diaphragm pressure sensitivity increased when the diaphragm radius and diaphragm thickness are large and thick respectively. In addition, flexural rigidity of the diaphragm also increases when the diaphragm is thick. Thus, it reduces the diaphragm deflection as well as diaphragm pressure sensitivity.

Moreover, diaphragm stress distribution was also studied to predict the likelihood of diaphragm failure. The findings indicated that tangential and radial stresses increased with the increment of the diaphragm deflection. Furthermore, the micro-diaphragm has a linear relationship with diaphragm deflection and applied pressure.

It is proven that the polyimide diaphragm has a better performance as compared to the silicon nitride diaphragm. This is due to the high Young's modulus possessed by the silicon nitride diaphragm that reduces its sensitivity. These findings are supported by findings from other researcher's (Xu, 2005, Deng, 2004, Madssen *et al.*, 2006, Osika *et al.*, 2007).

Unlike static response, diaphragm resonance frequency increased when diaphragm thickness and diaphragm radius is thick and small respectively. The finding also showed that diaphragm with higher Young's modulus, which is Silicon Nitride has a higher resonance frequency than polyimide diaphragm.

The findings indicated that when the thickness and radius is $4\ \mu\text{m}$ and $90\ \mu\text{m}$ respectively, the sensitivity of polyimide and silicon nitride diaphragms are of $3.01 \times 10^{-3}\ \mu\text{m}/\text{mmHg}$ and $7.86 \times 10^{-5}\ \mu\text{m}/\text{mmHg}$ respectively. At this particular dimension, the silicon nitride diaphragm attained the flexural rigidity of $1.56\ \text{Pa}\cdot\mu\text{m}^3$ whilst silicon nitride achieved the flexural rigidity of $0.05\ \text{Pa}\cdot\mu\text{m}^3$. In addition, the polyimide diaphragm obtained higher deflection of $0.9\ \mu\text{m}$ as compared to silicon nitride which only achieved $0.02\ \mu\text{m}$.

The Taguchi method was applied to find an optimum combination of design parameter for the micro-diaphragm. For all performance characteristics, diaphragm radius of $90\mu\text{m}$ (*i.e.* Control Factor A2) and diaphragm thickness of $4\mu\text{m}$ (*i.e.* Control Factor B1) and polyimide diaphragm (*i.e.* Control Factor C1) were the optimum control factors for micro-diaphragm performance.

The Pareto ANOVA analysis concluded that the diaphragm radius (*i.e.* control factor A) achieved the highest contribution ratio in affecting the performance of diaphragm's deflection and pressure sensitivity. Meanwhile, the diaphragm material (*i.e.* control factor C) plays a major role in determining the resonance frequency performance. This analysis has proven that the Taguchi method is suitable to optimize the micro-diaphragm performance. In this project, it is indicated that the optimization method of Taguchi is in agreement with other researchers' findings (Lai & Lin, 2007, Vijian and Arunachalam, 2007, Shalaby *et al.*, 2009).

A comparison of the designed micro-diaphragm with other findings is presented in Table 4.12. It is shown in this table that Toshima *et al.*, 2003 has successfully designed a smaller micro-diaphragm using silicon-based material. However, the sensitivity of this micro-diaphragm is less than the micro-diaphragm which was designed in this study.

Based on the data presented in this table, it is attested that the designed micro-diaphragm is sensitive as compared to the others' findings. In more specific, the polyimide diaphragm was successfully designed with the radius of $90\mu\text{m}$ and the thickness of $4\mu\text{m}$.

Table 4.10: A comparison of the designed micro-diaphragm for the optical pulse pressure sensor with the findings of other researchers'

Aspects	Hill <i>et al.</i> , 2007	Toshima <i>et al.</i> , 2003	Dagang <i>et al.</i> , 2006	Cibulaet <i>et al.</i> , 2002	This Study
Pressure range (mmHg)	0-125	0-400	0-150	0-300	0-300
Diaphragm-based material	Polymer	Silicon	Silicon	Polymer	Polymer
Diaphragm size/radius (μm)	50	50	150x150	62.5	90
Diaphragm thickness (μm)	2	0.7	1.5	4	4
Sensitivity ($\mu\text{m}/\text{mmHg}$)	0.0038	0.0015	0.2300	4.5×10^{-6}	0.0030

Generally, large and thin the micro-diaphragm leads to higher deflection and sensitivity. In addition, a diaphragm which vibrates with low resonance frequency is desired in designing the diaphragm. Thus, the Taguchi approach found the optimum combination of control factors which could gives the best performance for the micro-diaphragm.

In conclusion, this study has proven that miniature size micro-diaphragm is successfully designed to be used for the pressure range of 0 to 300 mmHg. Furthermore, the micro-diaphragm used polyimide, which is a polymer-based material to achieve a high sensitivity.

CHAPTER 5

CONCLUSION AND FUTURE WORK

5.1 Conclusion

The micro-diaphragm for the optical pulse pressure sensor has been successfully designed and its performance has also been simulated. It has been proven that the optimum design parameters could be chosen to obtain the best micro-diaphragm performance by employing the statistical analysis of Taguchi.

The main contribution of this research is the modelling of the micro-diaphragm with higher sensitivity to detect and measure small pulse pressure measurement. This research has developed the miniature size diaphragm which uses the polyimide. In particular, polyimide has excellent mechanical and good optical properties for optical pulse pressure sensor.

The designed micro-diaphragm is capable of detecting the pulse pressure with a range from 0 to 300 mmHg. The analyses of the micro-diaphragm performance concluded that thin micro-diaphragm and large diaphragm radius increased both the diaphragm deflection and diaphragm pressure sensitivity. Nevertheless, using this micro-diaphragm dimension, the resonance frequency has been reduced.

In addition, three design parameters have been found to affect the performance of micro-diaphragm. These design parameters namely diaphragm radius, diaphragm thickness and diaphragm materials must be optimized to ensure the best performance of micro-diaphragm. Furthermore, the optimization analysis of Taguchi which consists of the analyses of S/N ratio and Pareto ANOVA concluded that the diaphragm radius of

90 μm , diaphragm thickness of 4 μm and polyimide diaphragm formed the optimum combination of design parameters for the micro-diaphragm.

Thus, this study has demonstrated the modelling and simulation study of the micro-diaphragm for the optical pulse pressure sensor using the MEMS technology. Application of the Taguchi method was found to be a useful-technique to determine the optimum combination of the design parameters. The method could also be used in designing the micro-diaphragm with the best performance, less simulation runs and fewer design steps.

5.2 Future Work

This project can be further improved by considering these recommendations.

5.2.1 Improvement for micro-diaphragm structural design

The micro-diaphragm can be improved by introducing a boss and corrugated micro-diaphragm structure. This combination will give a high sensitivity and a high efficiency as compared to the flat micro-diaphragm (Sun *et al.*, 2008). In addition, the corrugated diaphragm gives larger dynamic range and thus offers wide range of linearity (Soin and Majlis, 2002).

As compared to the flat micro-diaphragm, a corrugated diaphragm with a much higher mechanical sensitivity has been achieved whereas a better reproducibility is obtained in several biomedical designs (Zou *et al.*, 1997). This corrugated micro-diaphragm can be introduced in designing the optical pulse sensor since it provides higher sensitivity than flat micro-diaphragm. With a high sensitivity micro-diaphragm, an adequate detection system to measure small micro-diaphragm deformation can be implemented.

References

- Aly, S.P., Jones, M.A., Al-Jarrah, V.P., 2007. Design of a diaphragm based dual optical sensor for pulse pressure measurements. *Optics Express*, 15(18), pp. 11111-11118.
- In addition, a diaphragm based dual optical sensor can be designed for pulse pressure measurements. This diaphragm based dual optical sensor can increase the measurement linearity and avoid optical intensity loss (Dagang *et al.*, 2006). This proposed design can successfully measure the pulse pressure. Thus, the diaphragm based dual optical sensor can be applied in designing the optical pulse pressure sensor.
- ### 5.2.2 Test & verification
- This study only focused on the modelling of the micro-diaphragm structure. The analysis of the micro-diaphragm performance was conducted on the simulation basis but the actual fabrication was not conducted. Therefore, the realization of the actual micro-diaphragm is still needed for test and verification.
- Beauchamp, J., 1985. *Topology in Mechanical Design*. In: *1985 European Conference on Design & New York: Elsevier Applied Science*.
- Combes, A., Sauer, M., Boudreau, J., Gagnon, H., Richard, J.L., Thromboreux, J., Gosselin, L., 1991. Pulse Pressure, a Marker of Long-term Cardiovascular Mortality in a French Male Population. *Arteriosclerosis*, 11(4), pp. 1472-1475.
- Chalazat, S., Gagnon, H., Turmel, U., Poirier, H., 1991. A self-excited piezoelectric micromachined transducer for biomedical applications. *Sensors and Actuators*, 22, pp. 351-358.
- Caquer, K., Gagnon, H., 2005. *MEMS in Medicine: Diagnostic and Therapeutic Systems*. In: *Proceedings of C2005A, Circulcia, France, 12-16 September 2005*.
- Chang, C.C., Liu, T.-C.K., Du, M.S., 2007. An Implantable Capacitive Pressure Sensor for Biomedical Applications. *Sensors and Actuators A*, 134, pp. 382-392.
- Clibber, P., Doherty, D., Grogan, E., 2002. *Microfluidic and Optical Pressure Sensor for Medical Applications*. *IEEE Transactions*, 49(14), pp. 2716-2724.
- Coleman, H.W., and Steele, W.G., 1988. *Experimental, theoretical and numerical analysis for engineers*, 2nd Ed. New York: Wiley.

References:

- Alty, S.R., James, N.A., Millasseau, S.C., Chowienczyk, P.J., 2007. Predicting Arterial Stiffness from Digital Volume Pulse Waveform. *IEEE Transaction on Biomedical Engineering*, 54(12), pp. 2268-2275.
- Bao, M. 2005. *Analysis and Design Principles of MEMS Devices*. Elsevier B.V.
- Bartsch, D-U, Mueller, A.J., O'Connor, N., Holmes, T., Freeman, W.R., 1996. 3-D Reconstruction of Blood Vessels in the Ocular Fundus from Confocal Scanning Laser Ophthalmoscope ICG Angiography. In Proceedings of *International Conference on Image Processing*. 16-19 September 1996. Lausanne, Switzerland.
- Basem, E-H, Roy, D.M., 2005. *Service Design for Six Sigma*. New Jersey: A Wiley-Interscience Publications.
- Bashir, R. 2004. BioMEMS: state-of-the-art in detection, opportunities and prospects. *Elsevier Science*, 56 (11), pp.1565-1568.
- Beards, C.F., 1996. *Structural Vibration: Analysis and Damping*, John Wiley & Sons Inc. New York.
- Belsley, K., Huber, D., and Goodman, J., All-Passive Fiber Optic Pressure Sensor, *In Tech*, 33, pp. 39-42.
- Bendell, T., 1988. *Taguchi method; Proceedings of the 1988 European Conference*. London & New York: Elsevier Applied Science.
- Benetos, A., Safar, M., Rudnichi, A., Smulyan, H., Richard, J.L., Ducimetiere, P., Guize, L., 1997. Pulse Pressure; a Predictor of Long-term Cardiovascular Mortality in a French Male Population. *Hypertension*, 30, pp. 1410-1415.
- Chatzandroulis, S., Goustouridis, D., Normand, P., Tsoukalas, D., 1997. A solid-state pressure-sensing microsystem for biomedical applications. *Sensor and Actuators, A* 62, pp. 551-555.
- Cheung, K. C., Renaud, P. 2005. BioMEMS in Medicine: Diagnostic and Therapeutic Systems. In: *IEEE Proceedings of ESSDERC*, Grenoble, France. 12-16 September 2005.
- Chiang, C-C, Lin, C-C K., Ju, M-S., 2007. An Implantable Capacitive Pressure Sensor for Biomedical Applications. *Sensors and Actuators A*, 134, pp. 382-388.
- Cibula, E., Donlagic, D., Stropnik, C., 2002. Miniature Fiber Optic Pressure Sensor for Medical Applications. *Applied Optics*, 44(14), pp. 2736-2744.
- Coleman, H.W., and Steele, W.G., 2000. *Experimentation and uncertainty analysis for engineers*, 2nd Ed, New York, Wiley

- Correia, J.H., Bartek, M., Wolffenbuttel, R.F., 1998. Load-deflection of a Low Stress SiN-Membrane/Si Frame Composite Diaphragm. In: *Technical Proceedings of the 1998 International Conference on Modeling and Simulation of Microsystem*. USA
- Cui, B., Cortot, Y., Veres, T., 2006. Polyimide Nanostructures Fabricated by Nanoimprint Litography and Its Applications, *Microelectronic Engineering*, 83, pp. 906-909.
- Dagang, G., Po, S.N.C., Hock, F.T.E., 2006. Design and optimization of Dual Optical Fiber MEMS Pressure Sensor for Biomedical Applications. *Journal of Physics: Conference Series*, 34, pp. 1073-1078.
- Darne, B., Girerd, X., Safar, M., Cambien, F., guize, L., 1989. Pulsatile versus Steady Component of Blood Pressure: A Cross-sectional Analysis and a Prospective Analysis on Cardiovascular Mortality, *Hypertension*, 13, pp. 392-400.
- Darnoby, I., Kryvyi, R., Lobur, M., Tkatchenko, S., 2008. Possibilities of the use of genetic algorithms in design of MEMS elements. In *MEMSTECH 2008, International Conference on Perspective Technologies and Methods in MEMS design*. 21-24 May 2008
- Deng J, 2004. *Development of Novel Optical Fiber Interferometric Sensors with High Sensitivity for Acoustic Emission Detection*. Dissertation submitted to Virginia Polytechnic Institute
- Dorf, R.C., 2006. *Sensors, Nanoscience, Biomedical Engineering, and Instruments*. 3rd Ed. CRC Press.
- Druzhinin, A., Lavitska, E., Maryamova, I., 1999. Medical Pressure Sensors on The Basis of Silicon Microcrystal and SOI layers. *Sensors and Actuators*, B 58, pp. 415-419.
- Eaton, W.P., Bitsie, F., Smith, J.H., Plummer, D.W. 1999. A New Analytical Solution for Diaphragm Deflection and Its Application to a Surface-Micromachined Pressure Sensor. In: *Technical Proceedings of The International Conference on Modeling and Simulation of Microsystem*. USA.
- Fang, J., Madhavan, S., Cohen, H., Alderman, M.H., 1995. Measures of Blood Pressure and Myocardial Infarction in Treated Hypertensive Patients, *J. Hypertens*, 13, pp. 413-419.
- Fisher, R.A., 1951. *Design of Experiments*, Oliver & Boyd, Edinburgh.
- Frahm, J. 1987. Localized Proton Spectroscopy using Stimulated Echoes. *J. Magn. Reson.* 72. pp 502.

Franklin, S.S., Khan, S.A., Wong, N.D., Larson, M.G., Levy, D., 1999. Is Pulse Pressure Useful in Predicting Risk for Coronary Heart Disease? The Framingham Heart Study, *Circulation*, 100, pp. 354-360.

Ghani, J.A., Choudhury, I.A., Hassan, H.H., 2004. Application of taguchi method in the optimization of the end milling parameters. *Journal of Materials Processing Technology*, 145, pp. 84-92.

Giovanni, M.D. 1982. *Flat and Corrugated Diaphragm Design Handbook* Marcel Dekker, Inc.

Goldberg, R.L., Jurgens, M.J., Mills, D.M., Henriques, C.S., Vaughan, D., Smith, S.W., 1997. Modeling of Piezoelectric Multilayer Ceramics using Finite Element Analysis. *IEEE Transactions on Ultrasonics, Ferroelectrics and Frequency Control*, 44(6), pp. 1204-1214.

Goustouridis, D., Normand, P., tsoukalas, D., 1998. Ultraminiature Silicon Capacitive Pressure-sensing Element Obtained by Silicon Fusion Bonding. *Sens. Actuators A*, A68, pp. 269-274

Gravel, P., Beaudoin, G., De Guise, J. A., 2004. A method for modeling noise in medical images, *IEEE Trans. Med. Imag.*, 23 (10), pp. 1221-1232.

Grayson A.C.R et al., 2004. A BioMEMS Review: MEMS Technology for Physiologically Integrated Devices. *Proceeding of the IEEE*, Vol. 92(1) January 2004.6-21.

Habibi, M., Lueder, E., Kallfass, T., Horst, D., 1995. Surface Micromachined Capacitive Absolute Pressure Sensor Array on a Glass Substrate, *Sensors and Actuators A*, 46, pp. 125-128.

Haldar, A., and Mahadevan, S., 2000. *Probability, reliability and statistical methods in engineering design*, New York, Wiley 2000

Hansis, E., Schafer, D., Dossel, O., Grass, M., 2008. Evaluation of Iterative Sparse Object Reconstruction from Few Projections for 3-D Rotational Coronary Angiography. *IEEE Transactions on Medical Imaging*, 27(11). pp. 1548-1555.

Hart, M., Conant, R., Lau, K., Muller, R., 1999. Troboscopic Phase Shifting Interferometry for Dynamic Characterization of Optical MEMS. *Proc. SPIE*, 3749, pp. 468-469.

Hautvast, G., Lobregt, S., Breeuwer, M., Gerritsen, F., 2006. Automatic contour propagation in cine cardiac magnetic resonance images. *IEEE Transaction on Medical Imaging*. 25 (11), pp. 1472-1482.

- He, G., Cuomo, F.W., 1991. Displacement Response, Detection Limit and Dynamic Range of Fiber Optic level Sensors, *J. Lightwave Technol.*, 9 (11), pp. 1618-1625.
- He, R., & Yang, P., 2006. Giant Piezoresistance Effect in Silicon Nanowires. *Nature Nanotechnology*, 1, pp. 42-46.
- Hill, G.C., Melamud, R., Declercq, F.E., Davenport, A.A., Chan, I.H., Hartwell, P.G., Pruitt, B.L., 2007. SU-8 MEMS Fabry-Perot Pressure Sensor. *Sensors and Actuators A: Physical*, 138(1), pp. 52-62.
- Hong, E., Trolier-McKinstry, S., Smith, R., Krishnaswamy, S.V., Freidhoff, C.B., 2006. Vibration of Micromachined Circular Piezoelectric Diaphragms. *IEEE Transactions on Ultrasonic, Ferroelectrics, and Frequency Control*, 53(4), pp. 697-706.
- Hossain, M.I., Abedin, A.H., 2008. Magnetic resonance angiography – an advanced technique in MRI using flow imaging. In: *LISSA 2007, IEEE/NIH Life Science Systems and Applications Workshop*, 2007. LISA 2007. Nov 8-9, 2007.
- Hsiung, K-L., 2006. Design of microelectromechanical systems for variability via chance-constrained optimization. *Journal of Physics: Conference Series* 34, pp. 162-167.
- Imai et al., 2006. A Novel Contrast Medium Detects Increased Permeability of Rat Injured Carotid Arteries in Magnetic Resonance T2 Mapping Imaging. *Journal of Atherosclerosis and Thrombosis*, 14(2), pp. 65-71.
- Intellisuite Technical Reference Manual, Version 8.2, 2007.
- Kalvesten, E., Smith, L., Tenerz, L., Stemme, G., 1998. The First Surface Micromachined Pressure Sensor for Cardiovascular Pressure Measurements. In *MEMS 98, The Eleventh Annual International Workshop on Micro Electro Mechanical Systems*, Heidelberg, Germany.
- Katsumata, T., Haga, Y., Minami, K., Esashi, M. 2000. Micromachined 125 μ m diameter ultra miniature fiber-optic pressure sensor for catheter. *Trans. Inst. Electrical Eng. Jpn.*, Part E 120E. pp. 58-63.
- Kerr, D.R., Milnes, A.G., 1963. Piezoresistance of Diffused Layers in Cubic Semiconductors. *Journal of Applied Physics*, 34, pp. 727-731.
- Kirby, E.D., 2006. A parameter design study in turning operation using the taguchi method. *The Technology Interface*. pp. 1-14.
- Ko, W.H., Bao, M-H., & Hong, Y-H, 1982. A High Sensitivity Integrated-Circuit Capacitive Pressure Transducer. *IEEE Transaction on Electron Devices*, 29(1), pp. 48-56.

Kopeć G., Podolec, P., Podolec, J., Rubis, P., Zmudka, K., Tracz, W., 2009. Atherosclerosis Progression Affects the Relationship between Endothelial Function and Aortic Stiffness. *Atherosclerosis*, 204, pp. 250-254.

Kuo, W., Prasad, V.R., Tillman, F.A., and Hawang, C-L., 2001. *Optimal Reliability Design*, Cambridge University Press

Kwak, B.M., Lee, S.H., Huh, J.S., 2000. A robust and versatile software system for optimal Design of MEMS structures, In *SPIE Proceedings Series*, Design, test, integration, and packaging of MEMS/MOEMS Conference Paris, France, 9-11 May 2000.

Lai, Y.L., Lin, C-H., 2007. Investigation of Structures of Microwave Microelectromechanical-System Switches by Taguchi Method. *Japanese Journal of Applied Physics*, 46, pp., 6539-6545.

Latifoglu, F., Sahan, S., Kara, S., Gunes, S. 2007. Diagnosis of atherosclerosis from carotid artery Doppler signal as a real world medical application of artificial immune systems. *Expert Systems with Applications*, 33, pp. 786-793.

Lax, H., Feinberg, A.W., Cohen, B.M., 1956. Studies of the arterial pulse wave. *J Chron Dis*, 3, pp. 618-631.

Le, H.P., Shah, K., Singh, J., Zayegh, A. 2006. Design and Implementation of an Optimised Wireless Pressure Sensor for Biomedical Application *Analog Interg Circ. Sig. Process*, 48, pp. 21-31.

Lehman, E.D., Gosling, R.G., and Sonksen, P.H., 1992. Arterial Wall Compliance in Diabetes, *Diabet Med*. 9, pp. 114-119.

Lion precision, 2009. Capacitive Sensor Operation and Optimization. (TechNote) [internet]. Available at: <http://www.lionprecision.com/tech-library/technotes/cap-0020-sensor-theory.html> [Accessed on 11 March 2009].

London, G.M., et al., 1990. Aortic and Large Artery Compliance in End-Stage Renal Failure. *Kidney Int*. 37, pp. 137-142.

Mackenzie, I.S., Wilkinson, I.B., Cockcroft, J.R., 1995. Assessment of arterial stiffness in clinical practice. *Q J Med*, 95, pp. 67-74.

Madou, M.J. 2002. *Fundamentals of Microfabrication The Science of Miniaturization*. 2nd Ed. CRC Press.

Madssen, E., Haere, P., Wiseth, R. 2006, Radial Artery Diameter and Vasodilatory properties After Transradial Coronary Angiography. *Ann Thorac Surg.*, 82, pp.1698-1703.

Marco, S., Samitier, J., Ruiz, O., Morante, J.R., Esteve, J., 1996. High Performance Piezoresistive Pressure Sensors for Biomedical Applications using Very Thin Structured Membranes. *Meas. Sci. Technol.* 7, pp. 1195-1203.

Matter, N.I., Scott, G.C., Grafendorfer, T., Macovski, A., Conolly, S.M., 2006. Rapid Polarizing Field Cycling in Magnetic Resonance Imaging. *IEEE Transactions on Medical Imaging.* 25(1). January 2006. pp. 84-93.

Matsumoto, H., and Saegusa, M., 1978. The Development of a Fiber-optic Catheter Tip Pressure Transducer, *Jap. J. Med. Eng. Technol.*, 2, pp. 239-242.

Maute, K., and Frangopol, D.M., 2003. Reliability-based design of MEMS mechanisms by topology optimization. *Comput. Structures*, 81, pp. 813-824

McCready, S.S., Heger, A.S., Harlow, T.H., Holbert, K.E., 2002. Piezoresistive Micromechanical Transducer Operation in a Pulsed Neutron and Gamma Ray Environment. In *IEEE Radiation Effects Data Workshop*. USA

Meirovitch L., 1997. *Principles and Techniques of Vibrations*. Englewood Cliff, NJ: Prentice Hall.

Melamud, R., Davenport, A.A., Hill G.C., Chan, I.H., Declercq, F., Hartwell, P.G., Pruitt B.L., 2005. Development of an SU-8 fabry-perot blood pressure sensor. In: *MEMS 2005, 18th IEEE International Conference on Micro Electro Mechanical Systems*. Miami USA, 30 Jan – 3 Feb 2005.

Mintz, G.S., Painter, J.A., Pichard, A.D., Kent, K.M., Satler, L.F., Popma, J.J., Chuang, Y.C., Bucher, T.A., Sokolowicz, L.E., Leon, M.B., 1995. Atherosclerosis in Angiographically "Normal" Coronary Artery Reference Segments: An Intravascular Ultrasound Study with Clinical Correlations. *Journal of American College of Cardiology*, 25(7). pp. 1479-1485.

Nalbant, M., Gokkaya, H., Sur, G., 2007. Application of Taguchi Method in the Optimization of Cutting Parameters for Surface Roughness in Turning, *Materials and Designs*, 28, pp., 1379-1385.

Nesson, S., 2007. *Miniature Fiber Optic Pressure Sensors for Intervertebral Disc Pressure Measurements in Rodents*. M.Sc. USA: University of Maryland, College Park.

Nichols, W.W., and O'Rourke, M.F., 1990. *Properties of Arterial Wall*. In: *McDonald's Blood Flow in Arteries: Theoretical, Experimental and Clinical Principles*. 3rd Ed. London: Edward Arnold.

Noh, H-S, Kim, S., Hesketh, P.J., Mao, H., Wong, L. 2003. Miniature Corrugated Diaphragm for Fiber-Optic-Linked Pressure Sensing (FOLPS). IN *IMECE '03*, 2003

ASME International Mechanical Engineering Congress & Exposition, Washinton, D.C., USA, 16-21 November 2003.

Osika, W., Dangardt, Gronros, F.J., Lundstam. U., Myredal, A., Johansson, M., Volkmann, R., Gustavsson, T., Gan, L. M., Friberg, P. 2007. Increasing Peripheral Artery Intima Thickness from Childhood to Seniority. *Journal of The American Heart Association*, 27(3), pp. 671-676.

Park, J.B., Bronzino, J.D., 2003. *Biomaterials Principles and Applications*. USA: CRC Press.

Pelletier, N., Beche, B., Tahani, N., Camberlein, L., Gaviot, E., Goulet, A., Landesman, J.P., Zyss, J., 2005. Integrated Mach-Zehnder Interferometer on Su-8 Polymer for Designing Pressure Sensors. In: *Proceedings of IEEE Sensors*. 30 Oct – 3 Nov 2005.

Polla, D.L. 2001. BioMEMS Applications in Medicine. *2001 International Symposium on Micromechatronics and Human Science SCIENCE*. IEEE. 13-15.

Pouladian, M., Golpayegani, M.R.H., 2003. Noninvasive detection of a atherosclerosis by Arterio-Oscillo-Gram. *Proceedings of the 25th Annual International Conference of the IEEE EMBS*. September 17-21, 2003.

Pramanik, C., Saha, H., Gangopadhyay, U., 2006. Design Optimization of a High Performance Silicon MEMS Piezoresistive Pressure Sensor for Biomedical Applications. *J. Micromech. Microeng.*, 16, pp. 2060-2066.

Puers, R., 1993. Capacitive Sensors: When and How to Use Them, *Sensors and Actuators A*, 37-38, pp. 93-105.

Saliterman, S.S., 2006. *Fundamentals of BioMEMS and Medical Microdevices*. SPIE Press, Bellingham Washington.

Sander, C.S., Knutti, J.W. Meindi, J.D., 1980. A Monolithic Capacitive Pressure Sensor with Pulse-Period Output, *IEEE Transaction on Electron Devices*, 27(5), pp. 927-930.

Sebastiani, G., Richard, F.G., Jones R.A., Haraldseth, G., Muller, T.B., Rinck, P.A., 1996. Analysis of dynamic magnetic resonance images. *IEEE Transactions on Medical Imaging*. 15(3). June 1996. pp. 268-277.

Shalaby, M.M., Wang, Z., Chow, L.L-W., Jensen, B.D., Volakis, J.L., Kurabayashi, K., Saitou, K., 2009. Robust Design of RF-MEMS Cantilever Switches using Contact Physics Modeling. *IEEE Transactions on Industrial Electronics*, 56(4), pp. 1012-1021

Sheplak, M., and Dugundji, J., 1998. Large deflections of clamped circular plates under initial tension and transitions to membrane behavior. *ASME Journal of Applied Mechanics*, 65(1), pp. 107-115.

- Shin, J.W., Chung, S.W., Kim, Y.K., Choi, B.K., 1998. Design and Fabrication of Micromirror Array Support by Vertical Springs, *Sensors & Actuators A*, 66, pp. 144-149.
- Shin, K.H., Moon, C.Y., Lee, T.H., Lim, C.H., Kim, Y.J., 2004. Implantable Flexible Wireless Pressure Sensor Module. *Sensors and Actuators A: Physical*, 123, pp. 30-35.
- Shirazee, N.A., Basak, A., Nakata, T., Takahashi, N., 1997. Analysis of Permanent Magnet Lifting Devices using Finite Elements, *IEEE Transactions on Magnetics*, 33(2), pp. 2211-2214.
- Silva, C.C.G., König, Jr., B., Carbonari, M.J., Yoshimoto, M., Allegrini S., Bressiani, J.C., 2008. Bone Growth Around Silicon Nitride Implants-An Evaluation by Scanning Electron Microscopy. *Materials Characterization*, 59, pp. 1339-1341.
- Singh, M., Li, J.K-J, Sigel Jr., G. H., Amory, D., 1990. Fiber Optic Pulse Sensor for Noninvasive Cardiovascular Applications. In Proceedings of the 1990 *IEEE Sixteenth Annual Northeast Bioengineering Conference*. 26-27 March 1990.
- Smith, C.S., 1954. Piezoresistance in Germanium and Silicon. *Physic Reviews*, 94, pp. 43-49.
- Soin, N., Majlis, B.Y., 2002. An Analytical Study on Diaphragm Behavior for Micro-machined Capacitive Pressure Sensor. *International Conference on Semiconductor Electronics*, Kuala Lumpur, Malaysia.
- Sun, Y., Feng, G., Georgiou, G., Niver, E., Noe, K., Chin, K., 2008. Center Embossed Design Guidelines and Fabry-Perot Diaphragm Fiber Optic Sensor, *Microelectronic Journal*, 39, pp. 711-716.
- Syrcos, G.P., 2003. Die Casting Process Optimization using Taguchi Methods. *Journal of Materials Processing Technology*, 135, pp. 68-74.
- Taguchi, G., 1989. *Introduction to Quality Engineering; Designing Quality into Products and Processes*. Tokyo: Asian Productivity Organization.
- Tasirin, S.M., Kamaruddin, S.K., Ghani, J.A., Lee, K.F., 2007. Optimization of drying parameters of bird's eye chili in a fluidized bed dryer. *Journal of Food Engineering*, 80, pp. 695-700.
- Tayag, T.J., Hoon, K.S., Marchetti, J., Jafri, I.H., 2003. Optical Fiber Interferometer for Measuring the in situ Deflection Characteristics of Microelectromechanical Structures. *Opt. Eng.*, 42(1), pp. 105-111.
- Thompson, L., Jelinek, H., Cornforth, D., 2008. Establishing Normative Data for Peripheral Arterial Disease Using Pulse Wave Analysis. In ISSNIP 2008, *International Conference on Intelligent Sensors, Sensor Networks and Information Processing*. 15-18 December 2008. Sydney Australia.

Timoshenko, S, 1974. *Vibration Problems in Engineering*, 1974, John Wiley & Son N.Y 4th Ed.

Timoshenko, S.P., Kreiger, S.W., 1959. *Theory of Plates and Shells*, 2nd Ed, McGraw Hill International Book Company.

Tohyama, O., Kohashi, M., Sugihara, M., Itoh, H., 1998. A Fiber-Optic Pressure Microsensor for Biomedical Applications. *Sensors and Actuators A*, 66, pp. 150-154.

Toshima, K., Watanabe, T., Kaneko, Y., Maesako, T., Takakashi, K., Diaphragm-Type Optical Fiber Pressure Sensor with a Sleeve Fiber Insertion. In MHS 2003, *International Symposium on Micromechatronics and Human Science*. Nagoya Municipal Industrial Research Institute, 19-22 October 2003.

Totsu, K., Haga, Y., Esashi, M., 2005. Ultra-Miniature Fiber-Optic Pressure Sensor using White Light Interferometry. *Journal of Micromechanics and Microengineering*, 15, pp. 71-75.

Tyan, C-C, Liu, S-H., Chen, J-Y, Chen, J.J, Liang W-M, 2008. A Novel Noninvasive Measurement Technique for Analyzing the Pressure Pulse Waveform of the Radial Artery, *IEEE Transactions on Biomedical Engineering*, 55(1), pp. 288-297.

Vijian, P., Arunachalam, V.P., 2007. Optimization of Squeeze Casting Process Parameters using Taguchi Analysis. *Int. J. Adv. Manuf. Technol.*, 33, pp. 1122-1127.

Wada, T., et al., 1994. Correlation of Ultrasound-Measured Common Carotid Artery Stiffness with Pathological Findings. *ArteriosclerThrombVascBiol*, 14 pp., 479-482.

Wang, X., Li, B., Russo, O.L., Roman, H. T., Chin, K.K., Farmer, K.R., 2006. Diaphragm design guidelines and an optical pressure sensor based on MEMS technique, *Microelectronic Journal*, 37, pp. 50-56.

Webpage: <http://www.stocktoncardiology.com/services.php?page=servNCE>, assessed on 12th May 2009.

Webpage: www.drainaging.commri.htm, assessed on 12th May 2009.
1009.

Website: www.moh.gov.my assessed on 10th May 2009

Wernicke, G., Kruschke, O., Demoli, N., Gruber, H., 1998. Some investigations on Holographic Microscopic Interferometry with Respect to the Estimation of Stress and Strain in Micro-opto-electro-mechanical Systems (MOEMS). *Proc. SPIE*, 3407, pp. 358-364.

Wilkinson, I.B., Hall, I.R., MacCallum, H., Mackenzie, I.S., McEniery, C.M., Van der Arend, B.J., Yae-Eun, S., Mackay, L.S., Webb, D.J., Cockcroft, J.R., 2002. Pulse Wave Analysis Clinical Evaluation of a Noninvasive, Widely Applicable Method for Assessing Endothelial Function. *ArteriosclerThrombVasc Biol.*, 22, pp. 147-152.

Wilson, J., 2005. *Sensor Technology Handbook*. UK. Newnes Elsevier.

Xiao-qi, N., Ming, W., Xu-xing C., Yi-xian, G and Hua R., 2006. An Optical Fiber MEMS Pressure Sensor Using Dual-Wavelength Interrogation. *Measurement Science and Technology*, 17(9), pp 2401- 2404.

Xu, J., 2005. *High Temperature High Bandwidth Fiber Optic Pressure Sensors*. Ph.D. Blacksburg, Virginia: Virginia Polytechnic and State University.

Yamagishi, M., Terashima, M., Awano, K., Kijima, M., Nakatani, S., Daikoku, S., Ito, K., Yasumura, Y., Miyatake, K., 1999. Morphology of Vulnerable Coronary Plaque: Insights from Follow-up of Patients Examined by Intravascular Ultrasound before an Acute Coronary Syndrome. *Journal of American College of Cardiology*, 35(1), pp.106-111.

Yu, H, Zhao, L., 2008. An efficient denoising procedure for magnetic resonance imaging. In: ICBBE 2008, *The 2nd International Conference on Bioinformatics and Biomedical Engineering*. Shanghai, China. 16-18 May, 2008.

Zhang, J.Z., Chen, J.C., Kirby, E.D., 2005. Surface Roughness Optimization in an End-Milling Operation using the Taguchi Design Method. *Journal of Materials Processing Technology*, 184, pp. 233-239.

Zhu, Y. and Wang, A. 2005. Miniature Fiber-Optic Pressure Sensor. *IEEE Photonics Technology Letters*, 17(2). pp. 447-449.

Zieman, S.J., Melenovsky, V., Kass, D.A., 2005. Mechanisms, Pathophysiology, and Therapy of Arterial Stiffness. *Arterioscler.Thromb.Vasc. Biol.*, 25, pp. 932-943.

APPENDIX A

LIST OF PUBLICATIONS

JOURNALS

1. Hasikin, K., Soin N. & Ibrahim, F. 2010. Hasikin, K., Soin, N. & Ibrahim, F., 2010. Application of Taguchi Method in optimizing micro-diaphragm performance. *Microelectronic Reliability*. Under review/Sent for publication on 16th March 2010. (ISI-Cited Publication)
2. Hasikin, K., Soin N. & Ibrahim, F. 2009. Modeling of an Optical Diaphragm for Human Pulse Pressure Detection. *Journal of World Scientific Engineering association Society (WSEAS) Transaction on electronic*, 5(11), pp. 447-456.

PROCEEDINGS

1. Hasikin, K., Soin N. & Ibrahim, F. 2010. Micro-diaphragm Performance Analysis for Polyimide Diaphragm. *2010 IEEE International Conference on Semiconductor Electronics (ICSE 2010)*, on 28-30 June 2010. (IEEE Xplore Cited Publication)
2. Hasikin, K., Soin N. & Ibrahim, F. 2009. Modeling of a Polyimide Diaphragm for an Optical Pulse Pressure Sensor. *International Conference for Technical Postgraduates (TECHPOS)* on 14-15 Dec 2009 (IEEE Xplore Cited Publication).
3. Hasikin, K., Soin N. & Ibrahim, F. 2009. Modeling an Optical Diaphragm for Human Pulse Pressure Detection. *Proceedings of the 8th WSEAS International Conference on Microelectronics, Nanoelectronics, Optoelectronics (MINO 2009)* on May 30 – June 1, 2009, (ISI-Cited Publication)
4. Hasikin, K., Ibrahim, F., & Soin, N. 2008. Determination of Design Parameters of a Biosensor for Human Artery Pulse Wave Detection, *International Proceedings of the International Federation for Medical and Biological Engineering (IFMBE)*, Springer 2008, June 25-28. ISBN: 978-3-540-69138-9 (Print), 978-3540-69139-6 (online). Springer Berlin Heidelberg. (ISI-Cited Publication)
5. Hasikin, K., Ibrahim, F., & Soin, N. 2008. Modeling of a Micro-Diaphragm biosensor for human artery pulse wave detection, *International Conference of the IEEE International Conference on Semiconductor Electronics (ICSE2008)*, Malaysia, on 25-27 Nov 2008. (IEEE Xplore Cited Publication) (ISI-Cited Publication)
6. Hasikin, K., Ibrahim, F., & Soin, N. 2008. Analysis of stress distribution of a circular diaphragm of a biosensor for human artery pulse wave detection *International Conference of Functional Material and Devices (ICFMD 2008)*, 15-18 June 2008

7. Hasikin, K., Ibrahim, F., & Soin, N. 2007. Review On Detection of Human Artery Pulse wave by using a biosensor. International Conference on Ergonomics 2007(ICE 07), Kuala Lumpur , Malaysia - 3-5 December 2007

SIMULATION RESULTS

Transient data for polyimide diaphragm

Time (sec)	Displacement (mm)
1.0E-07	4.29E-04
2.0E-07	2.32E-03
3.0E-07	4.39E-03
4.0E-07	2.09E-02
5.0E-07	4.04E-02
6.0E-07	6.19E-02
7.0E-07	8.72E-02
8.0E-07	1.17E-01
9.0E-07	1.51E-01
1.0E-06	1.89E-01
1.1E-06	2.31E-01
1.2E-06	2.77E-01
1.3E-06	3.27E-01
1.4E-06	3.81E-01
1.5E-06	4.38E-01
1.6E-06	4.98E-01
1.7E-06	5.61E-01
1.8E-06	6.27E-01
1.9E-06	6.96E-01
2.0E-06	7.68E-01
2.1E-06	8.43E-01
2.2E-06	9.21E-01
2.3E-06	1.002E-01
2.4E-06	1.086E-01
2.5E-06	1.173E-01
2.6E-06	1.263E-01
2.7E-06	1.356E-01
2.8E-06	1.452E-01
2.9E-06	1.551E-01
3.0E-06	1.653E-01
3.1E-06	1.758E-01
3.2E-06	1.866E-01
3.3E-06	1.977E-01
3.4E-06	2.091E-01
3.5E-06	2.208E-01
3.6E-06	2.328E-01
3.7E-06	2.451E-01
3.8E-06	2.577E-01
3.9E-06	2.706E-01
4.0E-06	2.838E-01
4.1E-06	2.973E-01
4.2E-06	3.111E-01
4.3E-06	3.252E-01
4.4E-06	3.396E-01
4.5E-06	3.543E-01
4.6E-06	3.693E-01
4.7E-06	3.846E-01
4.8E-06	4.002E-01
4.9E-06	4.161E-01
5.0E-06	4.323E-01
5.1E-06	4.488E-01
5.2E-06	4.656E-01
5.3E-06	4.827E-01
5.4E-06	5.001E-01
5.5E-06	5.178E-01
5.6E-06	5.358E-01
5.7E-06	5.541E-01
5.8E-06	5.727E-01
5.9E-06	5.916E-01
6.0E-06	6.108E-01
6.1E-06	6.303E-01
6.2E-06	6.501E-01
6.3E-06	6.702E-01
6.4E-06	6.906E-01
6.5E-06	7.113E-01
6.6E-06	7.323E-01
6.7E-06	7.536E-01
6.8E-06	7.752E-01
6.9E-06	7.971E-01
7.0E-06	8.193E-01
7.1E-06	8.418E-01
7.2E-06	8.646E-01
7.3E-06	8.877E-01
7.4E-06	9.111E-01
7.5E-06	9.348E-01
7.6E-06	9.588E-01
7.7E-06	9.831E-01
7.8E-06	1.0077E-01
7.9E-06	1.0326E-01
8.0E-06	1.0578E-01
8.1E-06	1.0832E-01
8.2E-06	1.1089E-01
8.3E-06	1.1349E-01
8.4E-06	1.1611E-01
8.5E-06	1.1876E-01
8.6E-06	1.2143E-01
8.7E-06	1.2413E-01
8.8E-06	1.2685E-01
8.9E-06	1.2959E-01
9.0E-06	1.3235E-01
9.1E-06	1.3513E-01
9.2E-06	1.3793E-01
9.3E-06	1.4075E-01
9.4E-06	1.4359E-01
9.5E-06	1.4645E-01
9.6E-06	1.4933E-01
9.7E-06	1.5223E-01
9.8E-06	1.5515E-01
9.9E-06	1.5809E-01
1.0E-05	1.6105E-01

APPENDIX B

SIMULATION RESULTS

Transient data for polyimide diaphragm

Time (sec)	Deflection (μm)
1.00E-07	-4.19E-04
2.00E-07	-2.52E-03
3.00E-07	-8.38E-03
4.00E-07	-2.06E-02
5.00E-07	-4.04E-02
6.00E-07	-6.68E-02
7.00E-07	-9.79E-02
8.00E-07	-0.132221
9.00E-07	-0.168412
1.00E-06	-0.204499
1.10E-06	-0.237847
1.20E-06	-0.265595
1.30E-06	-0.286318
1.40E-06	-0.300517
1.50E-06	-0.309267
1.60E-06	-0.313379
1.70E-06	-0.313949
1.80E-06	-0.31308
1.90E-06	-0.313736
2.00E-06	-0.318857
2.10E-06	-0.330057
2.20E-06	-0.347391
2.30E-06	-0.370607
2.40E-06	-0.399599
2.50E-06	-0.433555
2.60E-06	-0.470384
2.70E-06	-0.507052
2.80E-06	-0.540655
2.90E-06	-0.569479
3.00E-06	-0.592867
3.10E-06	-0.610255
3.20E-06	-0.621105
3.30E-06	-0.625872
3.40E-06	-0.626518
3.50E-06	-0.625915
3.60E-06	-0.626761

3.70E-06	-0.630855
3.80E-06	-0.639399
3.90E-06	-0.653718
4.00E-06	-0.674944
4.10E-06	-0.702977
4.20E-06	-0.736152
4.30E-06	-0.771953
4.40E-06	-0.808013
4.50E-06	-0.842517
4.60E-06	-0.873776
4.70E-06	-0.899827
4.80E-06	-0.919033
4.90E-06	-0.931115
5.00E-06	-0.93732
5.10E-06	-0.939233
5.20E-06	-0.937513
5.30E-06	-0.931793
5.40E-06	-0.921636
5.50E-06	-0.908206
5.60E-06	-0.894549
5.70E-06	-0.883231
5.80E-06	-0.874936
5.90E-06	-0.869752
6.00E-06	-0.868199
6.10E-06	-0.871265
6.20E-06	-0.879525
6.30E-06	-0.891629
6.40E-06	-0.904774
6.50E-06	-0.916857
6.60E-06	-0.927199
6.70E-06	-0.935335
6.80E-06	-0.94003
6.90E-06	-0.939763
7.00E-06	-0.933956
7.10E-06	-0.923894
7.20E-06	-0.911972
7.30E-06	-0.899804
7.40E-06	-0.88798
7.50E-06	-0.877414
7.60E-06	-0.869907
7.70E-06	-0.867327
7.80E-06	-0.87031
7.90E-06	-0.877734
8.00E-06	-0.887784
8.10E-06	-0.899383
8.20E-06	-0.911989

8.30E-06	-0.924337
8.40E-06	-0.934188
8.50E-06	-0.939487
8.60E-06	-0.939552
8.70E-06	-0.935181
8.80E-06	-0.927537
8.90E-06	-0.917152
9.00E-06	-0.904502
9.10E-06	-0.891135
9.20E-06	-0.879522
9.30E-06	-0.871774
9.40E-06	-0.868637
9.50E-06	-0.869719
9.60E-06	-0.874564
9.70E-06	-0.883154
9.80E-06	-0.895088
9.90E-06	-0.90867
1.00E-05	-0.921371

Transient data for silicon nitride diaphragm

Time (sec)	Deflection (μm)
1.00E-07	-3.95E-04
2.00E-07	-1.87E-03
3.00E-07	-4.02E-03
4.00E-07	-5.49E-03
5.00E-07	-5.92E-03
6.00E-07	-6.35E-03
7.00E-07	-7.76E-03
8.00E-07	-9.86E-03
9.00E-07	-1.14E-02
1.00E-06	-1.19E-02
1.10E-06	-1.23E-02
1.20E-06	-1.37E-02
1.30E-06	-1.57E-02
1.40E-06	-1.72E-02
1.50E-06	-1.78E-02
1.60E-06	-1.82E-02
1.70E-06	-1.96E-02
1.80E-06	-2.16E-02
1.90E-06	-2.31E-02
2.00E-06	-2.37E-02
2.10E-06	-2.38E-02
2.20E-06	-2.36E-02

2.30E-06	-2.34E-02
2.40E-06	-2.35E-02
2.50E-06	-2.37E-02
2.60E-06	-2.38E-02
2.70E-06	-2.36E-02
2.80E-06	-2.34E-02
2.90E-06	-2.35E-02
3.00E-06	-2.37E-02
3.10E-06	-2.38E-02
3.20E-06	-2.36E-02
3.30E-06	-2.34E-02
3.40E-06	-2.35E-02
3.50E-06	-2.37E-02
3.60E-06	-2.38E-02
3.70E-06	-2.36E-02
3.80E-06	-2.34E-02
3.90E-06	-2.35E-02
4.00E-06	-2.37E-02
4.10E-06	-2.38E-02
4.20E-06	-2.36E-02
4.30E-06	-2.35E-02
4.40E-06	-2.35E-02
4.50E-06	-2.37E-02
4.60E-06	-2.38E-02
4.70E-06	-2.36E-02
4.80E-06	-2.35E-02
4.90E-06	-2.35E-02
5.00E-06	-2.37E-02
5.10E-06	-2.38E-02
5.20E-06	-2.36E-02
5.30E-06	-2.35E-02
5.40E-06	-2.35E-02
5.50E-06	-2.37E-02
5.60E-06	-2.38E-02
5.70E-06	-2.36E-02
5.80E-06	-2.35E-02
5.90E-06	-2.35E-02
6.00E-06	-2.36E-02
6.10E-06	-2.37E-02
6.20E-06	-2.37E-02
6.30E-06	-2.35E-02
6.40E-06	-2.35E-02
6.50E-06	-2.36E-02
6.60E-06	-2.37E-02
6.70E-06	-2.37E-02

6.80E-06	-2.35E-02
6.90E-06	-2.35E-02
7.00E-06	-2.36E-02
7.10E-06	-2.37E-02
7.20E-06	-2.37E-02
7.30E-06	-2.35E-02
7.40E-06	-2.35E-02
7.50E-06	-2.36E-02
7.60E-06	-2.37E-02
7.70E-06	-2.37E-02
7.80E-06	-2.35E-02
7.90E-06	-2.35E-02
8.00E-06	-2.36E-02
8.10E-06	-2.37E-02
8.20E-06	-2.37E-02
8.30E-06	-2.35E-02
8.40E-06	-2.35E-02
8.50E-06	-2.36E-02
8.60E-06	-2.37E-02
8.70E-06	-2.37E-02
8.80E-06	-2.35E-02
8.90E-06	-2.35E-02
9.00E-06	-2.36E-02
9.10E-06	-2.37E-02
9.20E-06	-2.37E-02
9.30E-06	-2.35E-02
9.40E-06	-2.35E-02
9.50E-06	-2.36E-02
9.60E-06	-2.37E-02
9.70E-06	-2.37E-02
9.80E-06	-2.36E-02
9.90E-06	-2.35E-02
1.00E-05	-2.36E-02

APPENDIX C

CALCULATION FORMULA IN TAGUCHI METHOD

Calculated S/N ratio

Experiment Run	Factor			Designation	Calculated S/N Ratio		
	A	B	C		Deflection	Sensitivity	Resonance Frequency
1	1	1	1	A1B1C1	D1	E1	F1
2	2	1	1	A2B1C1	D2	E2	F2
3	1	2	1	A1B2C1	D3	E3	F3
4	2	2	1	A2B2C1	D4	E4	F4
5	1	1	2	A1B1C2	D5	E5	F5
6	2	1	2	A2B1C2	D6	E6	F6
7	1	2	2	A1B2C2	D7	E7	F7
8	2	2	2	A2B2C2	D8	E8	F8

Mean S/N ratio for diaphragm deflection, diaphragm pressure sensitivity and resonance frequency

Parameter\Factor	Diaphragm radius (A)		Diaphragm Thickness (B)		Diaphragm Material (C)	
	A1	A2	B1	B2	C1	C2
Diaphragm Deflection	Average (D1,D3,D5,D7)	Average (D2,D4,D6,D8)	Average (D1,D2,D5,D6)	Average (D3,D4,D7,D8)	Average (D1,D2,D3,D4)	Average (D5,D6,D7,D8)
Diaphragm Pressure Sensitivity	Average (E1,E3,E5,E7)	Average (E2,E4,E6,E8)	Average (E1,E2,E5E)	Average (E3,E4,E7,E8)	Average (E1,E2,E3,E4)	Average (E5,E6,E7,E8)
Resonance Frequency	Average (F1,F3,F5,F7)	Average (E2,E4,E6,E8)	Average (F1,F2,F5,F6)	Average (F3,F4,F7,F8)	Average (F1,F2,F3,F4)	Average (F5,F6,F7,F8)

Mean S/N ratio for control factor interactions

Parameter\Factor	Interaction between diaphragm radius & diaphragm thickness, (A X B)		Interaction between diaphragm radius & diaphragm material, (A X C)		Interaction diaphragm thickness and diaphragm material, (B X C)	
	A1 X B1	A2 X B2	A1 X C1	A2 X C2	B1 X C1	B2 X C2
Diaphragm Deflection	Average (D1, D5)	Average (D4, D8)	Average (D1, D3)	Average (D6, D8)	Average (D1, D2)	Average (D7, D8)
Diaphragm Pressure Sensitivity	Average (E1, E5)	Average (E4, E8)	Average (E1, E3)	Average (E6, E8)	Average (E1, E2)	Average (E7, E8)
Resonance Frequency	Average (F1, F5)	Average (F4, F8)	Average (F1, F3)	Average (F6, F8)	Average (F1, F2)	Average (F7, F8)

The calculated BC two-way table for diaphragm deflection

	B1	B2	Total
C1	$\Sigma (D1,D2) = G$	$\Sigma (D3,D4) = I$	$G + I$
C2	$\Sigma (D5,D6) = H$	$\Sigma (D7,D8) = J$	$H + J$
Total	$G + H$	$I + J$	$\Sigma (G+I), (H+J)$

The calculated BC two-way table for diaphragm pressure sensitivity

	B1	B2	Total
C1	$\Sigma (E1,E2) = K$	$\Sigma (E3,E4) = M$	$K + M$
C2	$\Sigma (E5,E6) = L$	$\Sigma (E7,E8) = N$	$L + N$
Total	$K + L$	$M + N$	$\Sigma (K + M), (L + N)$

The calculated BC two-way table for resonance frequency

	B1	B2	Total
C1	$\Sigma (F1,F2) = O$	$\Sigma (F3,F4) = Q$	$O + Q$
C2	$\Sigma (F5,F6) = P$	$\Sigma (F7,F8) = R$	$P + R$
Total	$O + P$	$Q + R$	$\Sigma (O + Q), (P + R)$